Development of a Lightweight Fixed-Wing Drone for Early Situational Awareness in Critical Applications

Master's thesis in Product Development

Alex Andersson

DEPARTMENT OF INDUSTRIAL AND MATERIALS SCIENCE

CHALMERS UNIVERSITY OF TECHNOLOGY
Gothenburg, Sweden 2025
www.chalmers.se

Master's thesis 2025

Development of a Lightweight Fixed-Wing Drone for Early Situational Awareness in Critical Applications

Alex Andersson

CHALMERS
UNIVERSITY OF TECHNOLOGY

Department of Industrial and Materials Science
Division of Product Development
Chalmers University of Technology
Gothenburg, Sweden 2025

Development of a Lightweight Fixed-Wing Drone for Early Situational Awareness in Critical Applications

Alex Andersson

© Alex Andersson, 2025.

Company supervisor: Fredrik Falkman, Remote.aero
Supervisor: Gauti Asbjörnsson, Department of Industrial and Materials Science
Examiner: Gauti Asbjörnsson, Department of Industrial and Materials Science

Master's Thesis 2025
Department of Industrial and Materials Science
Division of Product Development
Chalmers University of Technology
SE-412 96 Gothenburg
Telephone +46 31 772 1000

Cover: Final prototype during flight testing.

Typeset in LaTeX
Printed by Chalmers Reproservice
Gothenburg, Sweden 2025

Abstract

This thesis explores the development of a lightweight, sub-250 g fixed-wing drone intended for early situational awareness in emergency response scenarios. Conducted in collaboration with Remote.aero and the Swedish Sea Rescue Society, the work focuses on concept development, aerodynamic optimization, prototyping and validation through flight testing. An extensive benchmarking study identified key design parameters and trade-offs for tailless UAVs. Utilizing XFLR5 aerodynamic simulations, the study optimized critical design variables, notably aspect ratio, taper ratio and wing span, to maximize the L/D ratio within the intended flight envelope. Two prototypes were constructed using 3D printing, confirming theoretical predictions and demonstrating competitive performance during flight tests. The final prototype achieved a stall speed below 8 m/s, a maximum estimated endurance of approximately 43 minutes at loiter speed of 10 m/s, and a maximum estimated range of 55 km at a cruise speed of 25 m/s. The maximum L/D ratio was 16, at a loiter speed of 11 m/s. Its low intrinsic ground risk classification (iGRC 1) under current regulations simplifies deployment in both urban and rural settings, allowing it to compete with heavier systems while offering critical regulatory advantages. However, flight testing revealed that the reduced mass of the drone makes it sensitive to wind gusts, limiting reliable flight at wind speeds exceeding approximately 10 m/s unless additional airspeed margins are maintained. Ultimately, the design met all other requirements and could carry out a typical mission profile with ease, fulfilling the purpose of the project.

Keywords: Fixed-wing Drone, Sub-250g, Blended Wing Body, Tailless, Early Situational Awareness, Aerodynamic Optimization, XFLR5, Flight Testing.

Acknowledgements

This master's thesis was written solely by Alex Andersson in fulfillment of the requirements for the Master of Science degree in Product Development at Chalmers University of Technology, Gothenburg, Sweden.

The work was carried out in collaboration with Remote.aero. I would like to express my sincere gratitude to Fredrik Falkman for his supervision, his confidence in my abilities, and for making the project both exciting and rewarding.

I would also like to thank Associate Professor Gauti Asbjörnsson at Chalmers University of Technology for serving as both my supervisor and examiner. His guidance and support throughout the thesis work have been greatly appreciated.

Alex Andersson, Gothenburg, June 2025

Contents

1
Introduction

Drones are increasingly used to provide early situational awareness in emergency scenarios. This thesis explores the development of a lightweight fixed-wing drone under 250 grams, designed to support first responders with rapid aerial imagery. The following chapter outlines the background, purpose, and scope of the work.

1.1 Background

Early Situational Awareness for Sea Rescue
The Swedish Sea Rescue Society (SSRS) has been developing a fixed-wing drone for more than five years to improve rescue operations, in a project called "Eyes on Scene (EOS)". Their goal is to provide rescue teams with real-time aerial imagery within minutes of an emergency call by establishing a network of centrally controlled UAVs (unmanned aerial vehicles) along the Swedish west coast.

The ambition is to quickly help the crew mentally prepare and better understand the conditions of the rescue before heading out to sea. However, due to current legislation, this drone system is not yet in active operation. For the EOS system to work, drones must be able to fly beyond the visual line of sight (BVLOS), which is still very limited for all types of drones in Sweden. The SSRS 900 gram fixed-wing drone, which can be seen in Figure 1.1, has shown great promise for operations over water, where risks to people and property are minimal. Therefore, legislative changes appear promising for sea rescue [1].

Figure 1.1: The SSRS "Eyes on Scene" project 900 gram drone [1].

Early Situational Awareness for First Responders
The idea of using drones for early situational awareness has been studied for domains on land as well. Recent research by Västra Götalandsregionen has demonstrated the potential of autonomous drones in emergency response. In a four-month trial, self-flying drones equipped with cameras were dispatched to incidents such as fires, traffic accidents (see Figure 1.2), and cardiac arrests. The drones arrived first in 90% of cases, and by streaming live video from the accident site to the dispatch center, the drones provided real-time situational awareness before emergency personnel had reached the scene. This enhanced resource allocation, decision-making support, and mental preparedness for emergency responders [2].

Figure 1.2: Drone photo of traffic accident in roundabout [2].

The study also highlighted regulatory challenges, as airspace restrictions prevented drone deployment in over half of the test cases. This underscores the need for updated legislation to enable broader adoption of autonomous UAVs for emergency response. Compared to water-based operations, deploying drones over land introduces additional complexities and obstacles.

In these contexts, lightweight drones weighing less than 250 grams offer distinct advantages. Sub-250 g drones are governed by less restrictive laws due to their lower risk profile, allowing them to fly close to people or in urban areas, provided they comply with basic safety rules [3]. These exemptions make them highly suitable for rapid deployment in scenarios that require early situational awareness on land.

1.2 Purpose

The purpose of this thesis is to design and develop a sub-250 g fixed-wing drone that can provide early situational awareness for first responders. Drawing inspiration from SSRS's 900 g fixed-wing platform, this project focuses on meeting the stringent 250 g weight limit while striving to compete with its performance.

While the SSRS 900 g drone is well-suited for sea rescue operations over water, this project focuses on the specific requirements for land-based missions, where the lower risk profile of sub-250 g drones is more relevant.

Demonstrating that a sub-250 g drone can deliver operational results comparable to those of heavier platforms provides strong evidence that continued development of lightweight systems is both feasible and valuable. At the same time, by emphasizing the minimal risk these drones pose to people, property, and air traffic, this work aims to build confidence among regulators and support the case for exceptions or more flexible rules for drones used in critical applications.

1.3 Aim

Primary Aim

- Develop a sub-250 g fixed-wing UAV for early situational awareness in critical applications.
- Conduct an aerodynamic optimization study.

Secondary Aim

- Define key design variables and constraints for aerodynamic optimization.
- Evaluate design trade-offs and regulatory advantages for lightweight UAV systems in various domains.

1.4 Scope & Limitations

Scope

This project focuses on the design and development of a sub-250 g fixed-wing UAV for early situational awareness in critical applications on land. Literature studies and reverse engineering will be conducted to inform early design choices, followed by aerodynamic optimization that will focus on maximizing performance while adhering to strict weight constraints. Prototyping and aerodynamic validation through flight testing is also included. Regulatory considerations and application feasibility in emergency response and urban safety domains will be explored.

Limitations

The thesis will be conducted by a single researcher within a limited time frame and budget. Optimization is limited to aerodynamic performance. Hardware components and software for autonomous control will be sourced off-the-shelf. The optimization process will focus on a selected range of design variables due to computational and time limitations.

1.5 Deliverables

Primary Deliverables

- A fully operational sub-250 g UAV prototype, successfully validated through flight testing.
- A comprehensive report detailing the development process, optimization results and flight performance analysis.

Secondary Deliverables

- A requirement specification for the UAV based on research and stakeholder input.
- Insights into design challenges and solutions for lightweight UAV construction and optimization.

1.6 Societal, Ethical & Ecological Aspects

Societal

The drone this project intends to develop has significant potential societal benefits, such as improved safety and efficiency through rapid deployment in emergencies, possibly having a life saving impact by providing early on site imagery and thus reducing response times. Combined with the regulatory advantage of a sub-250 g drone, it may pave the way for a widespread integration of drones in several domains where early situational awareness is key. However, societal concerns also arise, especially regarding the negative public perceptions linked to the association of drones with warfare. This is highly relevant due to the current Russian invasion of Ukraine, where drones have become a fundamental part of the war. The design and appearance of drones, such as their color, shape and sound, could play a role in mitigating these perceptions. Additionally, privacy concerns and the potential of misuse, such as unauthorized surveillance, present ethical challenges that must be carefully addressed.

Ethical

Drones offer ethical advantages, such as reducing risks to human life by operating in hazardous environments, which minimizes the need to expose responders to danger. Additionally, their autonomous functionality can lower operational risks by eliminating human error during flights. Autonomy in UAVs does however introduce ethical dilemmas, as operating without a human pilot at the controls complicates questions of liability and accountability when harm occurs. This highlights the importance of clear decision-making frameworks within the software that manages flight routes and maneuvering. It also opens a discussion about allowing for human override in dangerous situations.

Ecological

Lightweight drones offer significant ecological benefits, including a reduced carbon footprint, as they consume far less energy compared to traditional aircraft or helicopters used for situational awareness. Additionally, they can play a crucial role in environmental monitoring, helping detect and mitigate disasters such as oil spills.

1.7 Stakeholders & Collaborating Partners

Stakeholders

Researcher: Alex Andersson, 076-864 19 15, aleuo@chalmers.se
Examiner: Gauti Asbjörnsson, 031-772 13 16, gauti@chalmers.se

Supervisor: Gauti Asbjörnsson, 031-772 13 16, gauti@chalmers.se
Company supervisor: Fredrik Falkman, 070-528 00 58, fredrik@remote.aero

Collaborating Partners
Remote.aero: A software company that supplies the mission control platform for the SSRS drone network, enabling safe and efficient large-scale drone operations.

Swedish Sea Rescue Society: A non-profit organization dedicated to saving lives at sea, operating along Sweden's coasts and large lakes. With 90% of its operations funded by donations, SSRS relies on volunteers and innovative technologies to provide efficient sea rescue services.

2
Methods

The methodology for this project is presented as a PERT diagram (Project Evaluation and Review Technique). The PERT diagram is a visual project management tool designed for mapping out and tracking tasks and timelines, ideal for projects where the chronological order is crucial, and each phase heavily depends on the deliverables from the previous stage. As shown in Figure 2.1, the project involved a pre-study in the form of literature studies, followed by initial concept development, an aerodynamic optimization study, prototyping and flight testing. The critical path for the project was estimated to be 91 days.

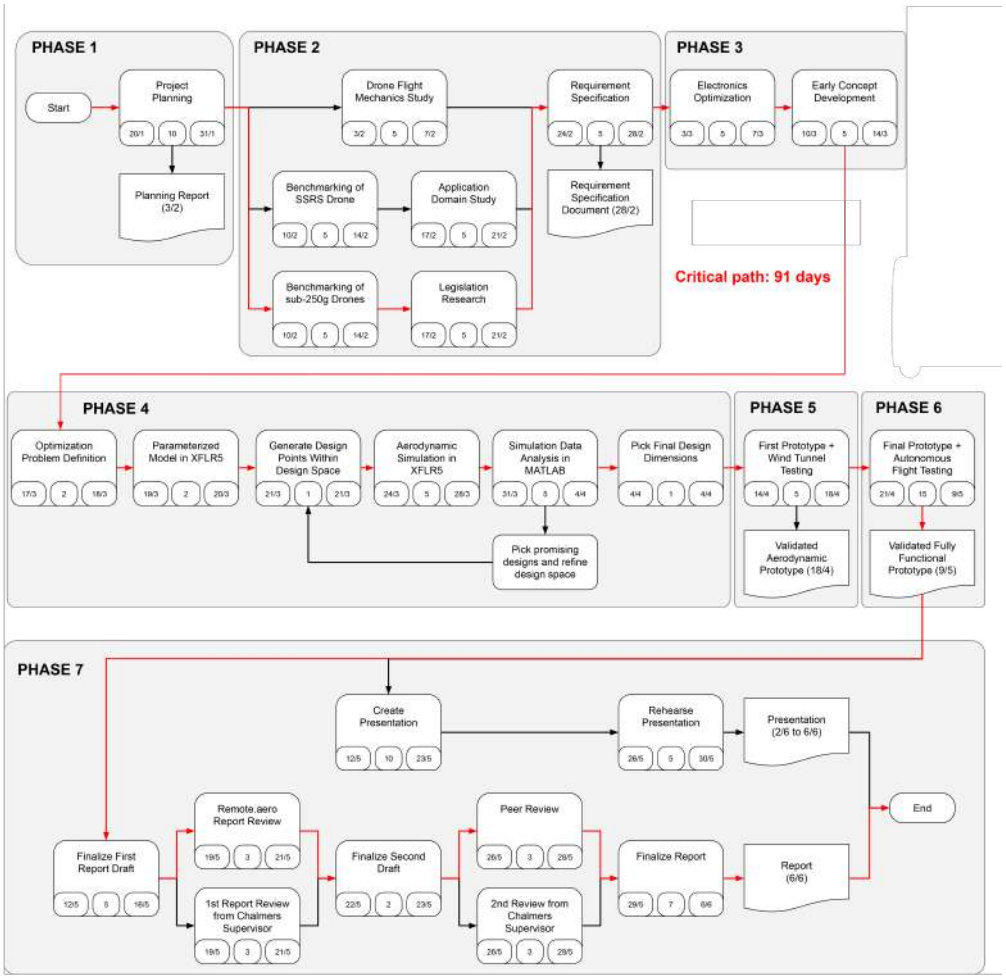

Figure 2.1: PERT diagram, illustrating an overview of the project workflow and major milestones. Available in the Appendix A.1.

2.1 Literature Studies

Flight Mechanics Study
This part of the literature study was conducted to improve the understanding of the flight mechanics of fixed-wing drones. The focus was placed on the principles of flight, flight control, aerodynamics, static and dynamic stability, and flying qualities. The objective was to identify the most critical parameters and to understand how they influence the dimensioning of the drone's body and wing geometry.

Benchmarking of the SSRS Drone
To inform the design process, the design and functionality of the SSRS 900 g drone were analyzed. This involved reviewing previous development efforts, analyzing the bill of materials (BOM), and conducting an aerodynamic analysis using CFD simulation tools in order to establish a basic understanding of the drone's aerodynamic performance. Additionally, research was conducted to investigate scaling challenges associated with reducing the drone's size and weight, thereby identifying potential carry-over design elements.

Benchmarking of sub-250 g Drones
Benchmarking lightweight fixed-wing drones with similar features, such as autonomous flying and built-in cameras, provided useful insights for development. It helped estimate performance values like endurance, range, and cruise speed, and showed the trade-offs between them. Looking at the materials and manufacturing methods also guided design choices. Finally, studying other drones on the market highlighted proven solutions to common problems, such as flight stability, and pointed out areas where new improvements could be made.

Legislation Research
Understanding current drone legislation was essential to ensure compliance with regulations governing sub-250 g drones. It also provided insight into how to maximize regulatory advantages and thus strengthen the case for influencing future policy changes.

Defining the Typical Mission
To define a representative mission scenario for the drone, relevant literature and statistical data on emergency response times in Sweden were reviewed. The focus was on understanding how a lightweight fixed-wing UAV could provide early situational awareness before the arrival of first responders. Studies on ambulance and fire brigade response times were used to estimate average operational distances and mission durations. Additional insights were drawn from existing research on drone deployment strategies to outline a flight profile including deployment, loitering, and return phases. These findings formed the basis for the mission definition and subsequent requirement specification.

Requirement Specification
The requirement specification was developed based on the findings from the literature analysis, in order to outline key functional and performance criteria for the

drone. Regulatory considerations were also included.

2.2 Initial Concept Development

Electronics Optimization
The initial phase of the concept development was to benchmark the components from the initial BOM to evaluate their performance, weight, and compatibility. Trade-offs between factors such as weight, power consumption, and functionality were investigated to identify the best possible solutions. New components were then selected based on the requirement specification, ensuring they met both functional and performance criteria. This process culminated in the creation of a newly optimized BOM, which included lightweight and efficient components, setting a defined weight limit for the drone body to adhere to the sub-250 g design constraint.

Early Concept Development
Early concept development was grounded in the benchmarking of existing lightweight drones, whilst drawing inspiration from the SSRS platform. This process identified which design features could be adapted and which would need to be engineered from scratch, with the development sequence tailored to the balance between carried-over and newly created elements.

XFLR5 Analysis
Once these preliminary design decisions were finalized, an aerodynamic analysis was performed using the aerodynamic simulation software XFLR5 to assess and refine the performance of the initial concept. XFLR5 is an analysis tool for airfoils, wings, and aircraft that is widely used for aerodynamic studies, particularly for low Reynolds number applications such as UAVs, RC planes, and other small aircraft. A previous MSc thesis on which the SSRS drone is based demonstrated that XFLR5 results correlate well with wind tunnel data, supporting the reliability of the tool for this application [4].

2.3 Aerodynamic Optimization Study

Optimization Problem Definition
The first part of the aerodynamic optimization study was to define the optimization problem, which consisted of defining objectives, constraints, and the design variables and their ranges:

- **The objective(s)** were derived directly from the requirement specification.
- **Design variables** and their ranges were established based on insights from previous literature studies. These key variables were selected for their significant influence on the defined objectives.
- **Constraints** were defined to ensure the design met functional and regulatory requirements.

Parameterized Model in XFLR5

A parameterized model was created in XFLR5 to serve as the basis for optimization and to ensure that the design variables were adjustable within the design space.

Generation of Design Points
A Python script using Latin Hypercube Sampling was implemented to generate a fixed number of design points (or samples), ensuring good coverage of the design space with fewer samples than Full Factorial Design. These design points were exported as a .xml file for import into XFLR5.

Aerodynamic Simulation
Aerodynamic simulations were conducted using XFLR5. Each design sample generated within the parameter space was individually simulated to assess key aerodynamic parameters. The simulation results were then saved and visualized using plots within XFLR5, allowing comparative analysis throughout the design space. This process enabled the identification of high-performing designs, which guided further refinement in the subsequent optimization stages.

2.4 Prototyping & Testing

Two prototypes were built following the same methodology. The first verified the feasibility of a sub-250 g airframe through construction and flight testing, while the second incorporated aerodynamic optimization and an onboard camera to enable detailed flight analysis.

Both iterations began with an advanced CAD model that integrated all necessary components. Each was fabricated via lightweight filament 3D printing and was fully functional and flight-ready. Comprehensive flight tests evaluated performance against the requirements. This was done by testing stability, control, and power consumption, as well as reviewing the onboard camera footage.

2.5 Gantt Schedule

The project schedule was outlined using a Gantt chart. A detailed version of the Gantt chart, showing the project timeline and task distribution, is available in Appendix A.2.

3
Defining the Mission

Before developing the drone, it is necessary to clearly define the mission scenario it is intended to perform. This chapter outlines the regulatory framework, the typical mission profile for early situational awareness operations, and the resulting requirement specification for the drone.

3.1 Drone Regulations

Drone regulations play a crucial role in shaping the mission profile, as they determine where and how the UAV can operate. For this project, the sub-250 g weight limit enables regulatory advantages, such as simplified approval and lower risk classification, that directly impact flight range, autonomy, and deployment in populated areas. Understanding these constraints is essential for defining a realistic and compliant mission scenario.

3.1.1 Open-, Specific- & Certified Category

Drones are classified into three main categories based on operational risk and regulatory requirements: open, specific and certified. The open category covers low-risk operations that do not require prior authorization, typically involving small drones flying within visual line of sight and away from populated areas. The specific category applies to moderate-risk operations that require a risk assessment and operational approval, such as flights beyond visual line of sight or in controlled airspace. The certified category is for high-risk operations, including large drones used for cargo or passenger transport, and requires strict certification, pilot licensing, and regulatory oversight, similar to manned aviation [3].

3.1.2 BVLOS - Beyond Visual Line of Sight

Beyond Visual Line of Sight (BVLOS) capability is essential for early situational awareness missions, enabling drones to operate beyond the operator's direct visual range. In urban environments, this applies to nearly all scenarios, as obstacles such as buildings and terrain quickly obstruct visibility. However, BVLOS flights are prohibited for drones operating in the open category [3].

Given these restrictions, operating in the specific category must be considered, with two possible approaches:

- **Operate under a Pre-Defined Risk Assessment (PDRA)**
  This standardized risk evaluation framework, specifically PDRA-G03, allows for BVLOS flights at low altitude [3]. However, it is restricted to predefined, pre-programmed routes, making it unsuitable for dynamic emergency response operations.
- **Operate under a Specific Operations Risk Assessment (SORA)**
  This approach involves applying for BVLOS permission using a customized risk assessment based on PDRA-G03, offering greater flexibility and allowing the operation to be tailored to specific mission requirements.

Given the constraints of pre-programmed routes in PDRA-G03, the SORA-based approach is the more viable option for this project.

3.1.3 SORA

The Specific Operations Risk Assessment (SORA) is a methodology used to classify the risk level associated with drone flights within the specific category of operations. The risk evaluation follows a 10-step process, which begins with a description of the operation and an assessment of both air risk and ground risk. By combining the residual risks, an intrinsic risk value for the entire operation is determined. This value is known as SAIL (Specific Assurance and Integrity Level) and defines the level of safety measures required for the operation [3].

Air risk is determined by the likelihood of encountering manned aircraft in the operational airspace. Factors affecting air risk include:

- **Density of manned air traffic** in the given airspace.
- **Mitigation measures** used to minimize collision risks.

Ground risk refers to the potential threat to people, property, or infrastructure from a drone impact. This risk is determined by the Intrinsic Ground Risk Class (iGRC), shown in Table 3.1, and the effectiveness of the applied risk mitigation measures. The iGRC is a key metric in the SORA methodology, representing the baseline level of risk posed by a drone operation. It is classified on a scale from 1 to 7, ranging from low to high risk [10]. The iGRC is determined based on the following factors:

- **Population density** in the operational area.
- **Type of operation:** Visual Line of Sight (VLOS) or Beyond Visual Line of Sight (BVLOS).
- **The drone's weight and kinetic energy.**

According to the latest SORA 2.5 guidelines:

> *"A UA weighing less than or equal to 250 g and having a maximum speed less than or equal to 25 m/s is considered to have an iGRC of 1 regardless of population density."*

This classification forms the primary justification for developing a sub-250 g drone. By keeping the weight below 250 grams and the maximum speed at or below 25 m/s, the ground risk is effectively minimized, making the operation significantly less restrictive. As a result, regulatory requirements are greatly reduced, simplifying the approval process for UAV missions in densely populated areas.

Table 3.1: Intrinsic Ground Risk Class (iGRC) determination [10].

Intrinsic UAS Ground Risk Class						
Maximum UA characteristic dimension		1m / approx. 3 ft	3 m / approx. 10 ft	8 m / approx. 25 ft	20 m / approx. 65 ft	40 m / approx. 130 ft
Maximum speed		*25 m/s*	*35 m/s*	*75 m/s*	*120 m/s*	*200 m/s*
Maximum iGRC population density (people/km²)	**Controlled Ground Area**	1	1	2	3	3
	< 5	2	3	4	5	6
	< 50	3	4	5	6	7
	< 500	4	5	6	7	8
	< 5,000	5	6	7	8	9
	< 50,000	6	7	8	9	10
	> 50,000	7	8	**Not part of SORA**		

- A UA weighing less than or equal to 250 g and having a maximum speed less than or equal to 25 m/s is considered to have an iGRC of 1 regardless of population density.
- A UA expected to not penetrate a standard dwelling will get a -1 GRC reduction in Step 3 from the M1(A) sheltering mitigation when not overflying large open assemblies of people, see Annex B for additional details.

3.2 The Typical Mission

3.2.1 Emergency Services Response Times & Distances

As previously mentioned, the drone should be developed for early situational awareness on land, to support first responders with a live-video feed from the site, before their arrival and during their work on the site. In order for the drone to be widely applicable, the typical mission will be based on the average values from country-wide Swedish first responder statistics:

For medical emergency response, the median response time for an ambulance is 15,4 minutes, which consists of a median alarm processing time of 3,9 minutes and a median driving time of 10,1 minutes. Once on-site, paramedics spend a median of 21,4 minutes providing medical care before transport or further intervention. With an average driving speed of 90 km/h, the estimated average distance to the emergency site is approximately 15 km [5], [6].

For fire and rescue emergency response across the country, the average response time for the fire brigade is 11,2 minutes, with significant regional variations. The alarm dispatch time from SOS Alarm averages 2,1 minutes, and the median driving time is about 9 minutes. With an estimated average speed of 65 km/h, the typical distance to the emergency site is 9,8 km [7], [8].

Police response time data is classified, but it is likely comparable to ambulance response times due to similar driving speeds. With emergency vehicles typically traveling at high speeds and following optimized routes, police units are expected to cover similar distances within similar time frames. Table 3.2 presents a summary of the response time and driving distance statistics for Swedish first responders.

Table 3.2: Estimated response times and distances for emergency services.

Parameter	**Ambulance**	**Fire Brigade**	**Police**
Alarm Processing Time (min)	3,9	2,1	*Unavailable*
Driving Time (min)	10,1	9	*Unavailable*
Total Response Time (min)	15,4	11,2	*Unavailable*
Estimated Distance (km)	15	9,8	*Estimated* ∼15
On-Site Time (min)	21,4	*Unavailable*	*Unavailable*

3.2.2 Drone Placement

While median response times provide a general overview of emergency response efficiency, additional factors significantly impact the effectiveness of a drone system. Key considerations include the number of drones deployed and their geographical placement, similar to how the SSRS drones are planned to be positioned along Sweden's west coast to optimize coverage.

In urban areas, where ambulances typically arrive quickly, the drone's role may be limited. However, in rural or remote regions, where emergency medical services response times are considerably longer, a strategically placed drone could have a substantial impact. By arriving significantly earlier than the ambulance, the drone could provide an early aerial assessment, enabling:

- Faster decision-making and resource allocation.
- Situational awareness for dispatchers and emergency responders.
- Mental preparedness for first responder personnel en route to the scene.

Although determining the exact quantity and placement of drones is beyond the scope of this project, valuable insights can be drawn from a study by Claesson et al. (2016) [9]. Their research explores the feasibility of drone systems in reducing response times and delivering AEDs (Automated External Defibrillators) in the case of OHCA (Out-of-Hospital Cardiac Arrest). While this project primarily focuses on early situational awareness, their study serves as a baseline for strategic drone deployment.

In a simulated environment, the study found that strategically placing drones with a 10 km operational radius, which can be seen in Figure 3.1, and an assumed speed of 70 km/h, leading to an 8,5-minute flight time, significantly improved response times:

- **Urban area OHCA**
  The drone arrived before EMS in 32% of cases.
  The mean time saved was 1,5 minutes.
- **Rural area OHCA**
  The drone arrived before EMS in 93% of cases.
  The mean time saved was 19 minutes.

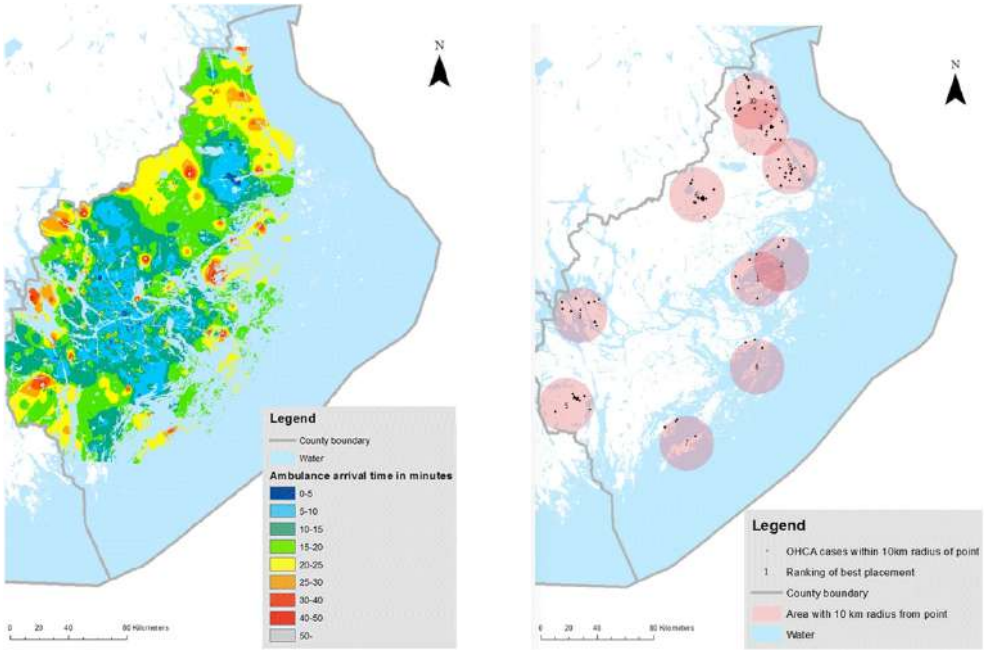

(a) **(b)**

Figure 3.1: Figure (a) shows ambulance arrival time in minutes, Stockholm County 2006–2013. Figure (b) shows the optimal placement of UAVs [9].

3.2.3 Flight Profile

To ensure early situational awareness, the drone must arrive at the site before the first responders. By being dispatched immediately and flying directly to the scene, it avoids traffic delays and ensures a faster, more predictable arrival time. To define the mission profile, the study by Claesson et al. (2016) serves as a baseline, demonstrating that drones with an 8,5-minute flight time and a 10 km operational radius significantly reduced response times, particularly in rural areas. To achieve similar effectiveness, the drone should be designed to match these range and response time parameters. Since ambulances typically cover the longest distances among emergency services, a drone capable of rapid medical response within this range would also be well-suited for other emergency scenarios requiring fast deployment.

The flight profile for a typical mission is defined as follows:

Launch
Traveling at its maximum allowable speed of 25 m/s, the drone covers 10 km in approximately 7 minutes, assuming no headwinds or other environmental factors.

Loiter
Upon arrival, the drone loiters on-site, providing real-time video feed until first responders reach the scene. Given its faster speed compared to the drone used in Claesson et al. (2016), a conservative estimate suggests a loitering time of 18 minutes should be possible. For optimal endurance, the loitering speed is estimated to be 10–15 m/s (40–60% of max speed).

Landing or Return Flight
Once its primary mission is complete, the drone should land at the scene for retrieval by first responders if battery constraints prevent a return flight. While on-site landing remains a viable alternative given the drone's low risk profile, returning to base is preferred as it minimizes disruption to emergency operations. If sufficient battery remains, the drone should fly back to the launch site at cruise speed to optimize range. For efficient forward flight, the cruise speed is estimated to be 18–22 m/s (70–90% of max speed), resulting in a 8-10 minute return flight.

The complete flight profile is illustrated in Figure 3.2.

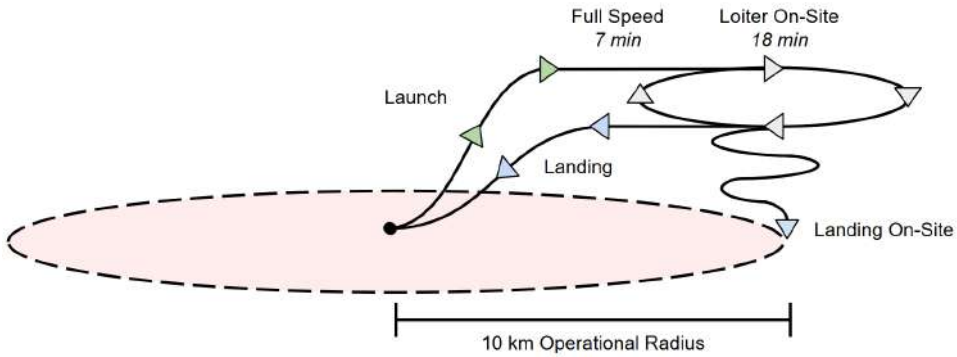

Figure 3.2: Flight profile for a typical mission.

3.3 Requirement Specification

3.3.1 Mission Requirements

The drone developed in this project should be capable of performing the specified mission while meeting the maximum weight and speed requirements necessary for an iGRC rating of 1. Additionally, it should be designed to withstand harsh weather conditions, including all types of rain and wind speeds of up to 15 m/s.

3.3.2 Legal Requirements

The legal and technical requirements for the drone are based on necessary risk mitigation measures, known as Operational Safety Objectives (OSOs). While most OSOs focus on operational procedures and crew coordination areas (outside the scope of this project) some specifically address the drone's hardware, software, and safety features. The OSOs applicable to this drone are determined by its SAIL rating from the Specific Operations Risk Assessment (SORA) process. Since a full SORA evaluation is beyond the scope of this project, a conservative estimate assigns a SAIL level of 2, consistent with the current SSRS 900 g drone.

For SAIL 2, the only required design-related OSO is:

> *OSO #06 – C3 link characteristics (e.g., performance, spectrum use) are appropriate for the operation.*

This requirement ensures communication safety, mandating that the C3 link (Command, Control, and Communication) is robust enough for the intended operation and that the remote pilot can continuously monitor its performance.

To further enhance safety and maintain a robust design approach, this project also considers the technical requirements for a 250 g drone (C0 class) in the open category. These include:

- **Safe Control:** The drone must be stable, maneuverable, and capable of maintaining data link performance under all foreseeable operational conditions, including potential system failures.
- **Safe Design:** The drone must minimize injury risks, avoid sharp edges unless technically necessary, and mitigate potential injuries from propeller blades.

3.3.3 Structural Design Requirements

The drone should have a robust structural design to minimize damage in the event of an unforeseen impact or crash. It should be easy to repair, with modular components that allow for quick part replacement if needed. Additionally, material selection and manufacturing methods should be optimized for scalability, ensuring feasibility for large-scale production. Table 3.3 summarizes the complete requirement specification list.

Table 3.3: Requirement specification.
LR=Legal Requirement, R.=Requirement ("must"), D.=Desire ("should").

Category	Requirement	No.
Flight Performance		
Max Weight	< 250 g	LR.1
Max Speed	25 m/s	LR.2
Cruise Speed	18–22 m/s	D.1
Loiter Speed	10-15 m/s	D.2
Stall Speed	8 m/s	R.1
Weather	Must withstand heavy rain and wind speeds up to 15 m/s.	R.2
Endurance	Must be able to fly at top speed for 8 min and then loiter for 18 min.	R.3
Range	Must be able to operate within a 10 km radius.	R.4
Mission Specific		
Control System	Must have autonomous flight capability with autopilot.	R.5
C3 Link/Safety	Must be stable, maneuverable, and maintain data link performance under all foreseeable operational conditions, including system failures.	LR.3
Camera	Must have stabilized HD live video streaming.	R.6
Telemetry	Must have onboard GPS and airspeed sensor.	R.7
Deployment	Must be dispatchable immediately after an emergency call.	R.8
Landing	Must be able to land on-site if necessary.	R.9
Return	Should be able to return to base at cruise speed.	D.3
Structure & Design		
Durability	Must have a robust design as to not break main airframe on impact at full speed.	R.10
Ease of Repair	Should use modular components that allow for quick and simple part replacement.	D.4
Scalability	Material selection and manufacturing methods must be optimized for large-scale production.	R.11
Appearance	Must be associated with emergency service; bright safety colors.	R.12
Design Safety	The drone must minimize injury risks, avoid sharp edges unless technically necessary, and mitigate potential injuries from propeller blades.	LR.4

4

Introduction to UAV Systems

This chapter provides an overview of key UAV system types, with a focus on fixed-wing platforms. It outlines common configurations, capabilities, and trade-offs relevant to the design of a lightweight drone.

4.1 Overview of UAVs

An Unmanned Aerial Vehicle (UAV), commonly known as a drone, is an aircraft operated remotely or autonomously via an onboard autopilot and navigation system. The terms "drone" and "UAV" are used interchangeably throughout this report. UAVs are generally categorized into two main types: rotary-wing and fixed-wing configurations (see Figure 4.1) [14], [16].

- **Rotary-wing UAVs** (e.g., helicopters, multirotors) are highly maneuverable, capable of vertical takeoff and landing (VTOL), and ideal for hovering tasks. However, they suffer from shorter endurance and higher energy consumption, making them less suited for long-range missions [17].
- **Fixed-wing UAVs** generate lift through aerodynamic surfaces and are significantly more efficient in long-duration and high-speed applications. These UAVs require continuous forward motion for sustained flight and typically rely on runways, catapults, or hand launches for takeoff [15].

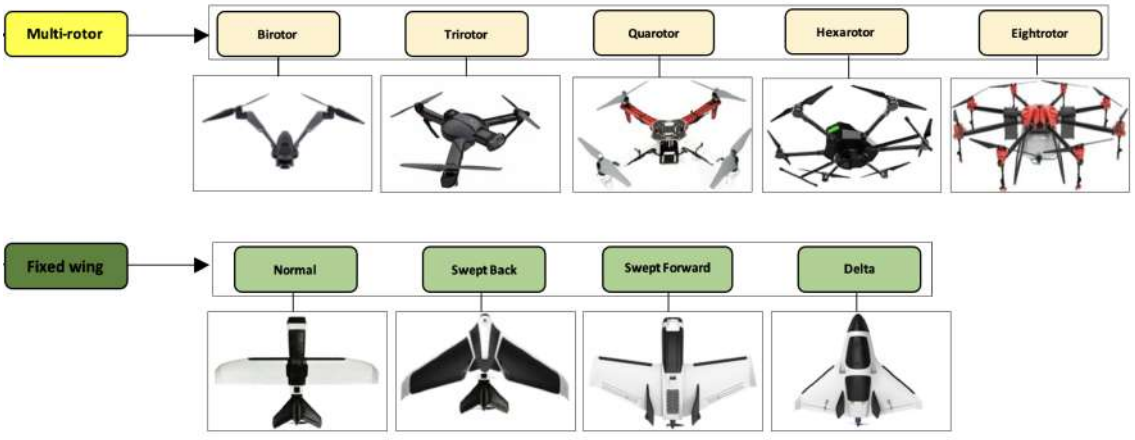

Figure 4.1: Drone categories [17].

4.2 Selection of a Tailless Fixed-Wing UAV

A tailless fixed-wing UAV, similar to the 900 g SSRS drone, has been selected for this project due to its superior aerodynamic efficiency and reduced structural weight.

Fixed-wing UAVs offer significantly longer flight endurance and greater efficiency for large-area surveillance compared to rotary-wing UAVs, which have higher energy consumption and limited range [15]. A tailless configuration eliminates the need for a traditional tail assembly, minimizing mass and drag. These are key factors in achieving a sub-250 g UAV while maintaining sufficient endurance. While the tailless configuration enhances aerodynamic performance and reduces weight, it also introduces certain challenges:

- Reduced yaw and pitch stability, necessitating an autopilot for active stabilization [20].
- Elevon-based control must manage both pitch and roll, requiring precise tuning for optimal flight control [20].

Despite these challenges, the SSRS 900 g UAV has proven that a tailless configuration is well-suited for situational awareness missions, making it the logical choice for a scaled-down sub-250 g version.

4.3 UAV Hardware Components Overview

The functionality of a drone is divided into distinct subsystems, each responsible for a specific aspect of its operation.

4.3.1 Airframe

The airframe is the primary structure of the drone (see Figure 4.2), including the wings and, if present, a fuselage. For lightweight fixed-wing drones, construction follows similar principles to conventional RC aircraft. Wings are typically made of low-density expanded polypropylene (EPP) foam and reinforced spanwise with a carbon spar to improve structural integrity. An outer sheathing is typically applied using modeling foil or fabric, improving aerodynamics. The middle of the airframe is hollowed out to house the required components.

An alternative to traditional foam construction for the airframe is 3D printing. A special filament called "foaming PLA (polylactide)" allow for airframes that are nearly as lightweight as those made from foam. The key advantage of 3D printing is that it eliminates the need for expensive tooling, unlike foam, which typically requires either CNC-cutting from large foam blocks or creating dedicated injection molds. This makes 3D printing especially suitable for prototyping. However, it comes with trade-offs, including reduced durability and a rougher surface finish.

Figure 4.2: Drone airframe [11].

4.3.2 Propulsion & Actuator System

Brushless DC Motor

The motor is the primary propulsion component in a UAV, converting electrical energy into mechanical motion to generate thrust. UAV motors are typically brushless DC motors (see Figure 4.3) due to their higher efficiency, durability, and power-to-weight ratio compared to brushed motors.

Figure 4.3: Brushless DC motor [12].

Key specifications include Kv rating (RPM per Volt), power output (W), maximum voltage (S-rating), and shaft diameter for propeller compatibility.

Servos

Servos control the UAV's aerodynamic control surfaces, enabling maneuverability and stability. They convert electrical signals into mechanical movement and are used to control pitch, roll, and yaw.

Figure 4.4: Digital servo [12].

Key specifications include torque (kg/cm), operating voltage (V), rotation speed (s/60°), and gear material (metal or plastic). Digital servos (see Figure 4.4) offer faster response times due to higher control signal frequency, while analog servos are simpler but slower.

Propeller

The propeller (see Figure 4.5) generates thrust by converting motor power into aerodynamic force, enabling forward motion in a fixed-wing UAV. The efficiency and performance of the propeller depend on its size, shape, and configuration. Key specifications include diameter and pitch (e.g., a 12×5.5 propeller has a 12-inch diameter and a 5.5-inch pitch). Tractor (pull) propellers are front-mounted and operate in clean airflow, while pusher (push) propellers are rear-mounted and may experience turbulence from the wing.

Figure 4.5: Propeller [12].

Electronic Speed Controller

Electronic Speed Controllers (ESC) (see Figure 4.6) regulate power delivery to UAV motors. Each motor requires a dedicated ESC, which must be matched to the motor's voltage and current requirements. ESCs are designed separately for brushed and brushless motors, with brushless variants being more common in UAVs. Key specifications include input voltage (S-rating), continuous and burst current (A), and connector type, all of which determine compatibility with the UAV's power system.

Figure 4.6: Electronic Speed Controller [12].

4.3.3 Power System

Batteries are the power source for UAVs. The most commonly used technologies are Lithium-Polymer (Li-Po) and Lithium-Ion (Li-Ion) (see Figure 4.7). Li-Po batteries are lightweight, offer high energy density, and support high discharge rates, making them ideal for agile UAV maneuvers and short bursts of power. Li-Ion batteries have longer lifespans, better thermal stability, and come in standard formats (e.g., 18650), making them easier to manage. Though slightly heavier, they provide higher energy capacity and are better suited for long-endurance missions. Key parameters are capacity (mAh), voltage (V), and discharge current (A).

Figure 4.7: Li-Po (top) and Li-Ion (bottom) battery types [12].

4.3.4 Autopilot & Flight Computer

The autopilot and flight computer (see Figure 4.8) serve as the UAV's central control system, managing stability, navigation, and autonomous functions. It processes sensor data and executes control commands.

- Key functions include attitude stabilization, waypoint navigation, failsafe handling, and real-time flight adjustments.
- Common systems include off-the-shelf flight controllers like Pixhawk or Pixracer, which offer robust firmware (e.g., ArduPilot, PX4), or custom-built controllers optimized for specific UAV requirements.
- Integrated sensors, such as IMU (Inertial Measurement Unit), GPS, barometer, and airspeed sensors, provide real-time feedback for precise flight control.
- Communication interfaces, including RC input, telemetry, and ground control station (GCS) integration, allow for manual override and mission monitoring.

Figure 4.8: Pixracer flight computer [13].

4.3.5 Camera & Sensors

Cameras and sensors provide real-time situational awareness and flight data, enabling navigation, monitoring, and mission-specific operations for UAVs. Camera systems (see Figure 4.9) are used for live video streaming, reconnaissance, and object detection, with stabilized HD cameras enhancing visibility and clarity. Additional sensors such as airspeed sensors help optimize flight performance and efficiency, while barometers assist in altitude control.

Figure 4.9: Drone camera [12].

Environmental and mission-specific sensors include thermal or infrared cameras for low-light or search-and-rescue missions, as well as LiDAR or depth sensors for terrain mapping and obstacle avoidance.

5

Flight Mechanics for Tailless Aircraft

5.1 Introduction to Flight Mechanics

Flight mechanics studies the motion of an aircraft in flight. It can be divided into five key areas: trajectory analysis, stability and control, aircraft sizing, simulation, and flight testing [21], [22].

- **Trajectory analysis** is the study of an aircraft's path through space under the influence of aerodynamic forces, propulsion, and external conditions [22].
- **Stability and control** determine an aircraft's ability to maintain and adjust its flight path in response to disturbances or pilot inputs [22].
- **Aircraft sizing** is an iterative process that involves determining the dimensions, weight, and propulsion requirements of an airplane based on a predefined mission profile [22].
- **Simulation** involves the numerical integration of differential equations to model flight dynamics [22].
- **Flight testing** is the experimental validation phase of aircraft development, where real-world data is collected to evaluate performance, stability, and control characteristics [22].

This chapter will cover the theoretical aspects of flight mechanics: trajectory analysis, stability and control, focusing on its application on tailless aircraft. Aircraft sizing, simulation and flight testing is covered at a later stage in the report.

5.2 Fundamentals of Flight

5.2.1 Forces Acting on an Aircraft

There are four main forces acting upon an aircraft: weight, lift, drag and thrust. When an aircraft is in straight and level flight, all of these forces acting upon it are perfectly balanced (see Figure 5.1). It can be seen as the forces working in pairs: lift counteracting weight, thrust counteracting drag [23].

Weight is a force that pulls the aircraft down due to gravity acting on the mass of the aircraft. This force is therefore constantly directed towards the center of the earth. The weight of an airplane is distributed across its entire structure. However,

it is often simplified as being concentrated at a single point known as the center of gravity (CG). During flight, the airplane rotates around this point [23].

Lift is the aerodynamic force that enables an aircraft to fly by overcoming its weight. It is generated by the wings as they move through the air and acts perpendicular to the direction of flight. Lift arises from a combination of Bernoulli's Principle and Newton's Third Law of Motion: the pressure difference created by faster airflow over the wing's upper surface (Bernoulli) and the downward deflection of air producing an equal and opposite upward force (Newton). The lift force acts through a single point called the center of pressure (CP), which is determined by the pressure distribution around the aircraft's body [24].

Drag is a resisting force experienced by the aircraft as it moves through the air. This aerodynamic force opposes the aircraft's motion and is influenced by several factors, including: The overall shape and size of the aircraft, the viscosity of the air and the aircraft's speed. Rather than analyzing drag from each component separately, it is typically combined into a single total drag force for simplicity. This force always acts in the opposite direction of flight and is applied through the CP [23].

Thrust is the force that is generated by the aircraft's propulsion system to overcome the drag. It is generally created using jet engines or propellers and pushes the aircraft forward through the air. In the context of small scale fixed-wing UAVs, propeller-produced thrust is the most common. A propeller functions like a rotating wing, generating lift as it moves through the air to produce thrust. Depending on the placement of the propeller, it can either produce a pulling-, or a pushing force [23].

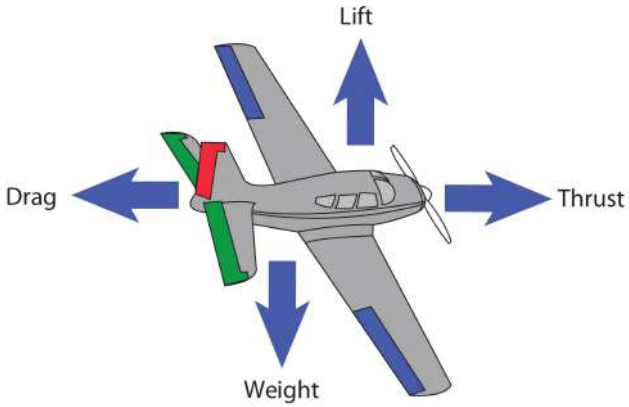

Figure 5.1: Forces acting on an aircraft [27].

5.2.2 Axis of Motion

In three-dimensional flight, an aircraft's orientation must be controlled along all three axes, which intersect at the CG. These axes form a perpendicular coordinate system, and the aircraft's attitude is determined by its rotation around them [25].

Vertical Axis → Yaw

The vertical axis is perpendicular to the wings of the plane, as can bee seen in Figure 5.2. Motion around this axis is called yaw and causes the aircraft's nose to move from side to side [25].

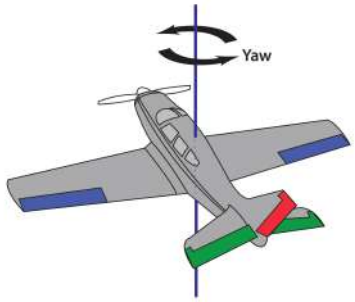

Figure 5.2: Vertical axis (yaw motion) [27].

Lateral Axis → Pitch

The lateral axis is perpendicular to the vertical axis and aligned with the wings of the plane (see Figure 5.3). Motion around this axis is called pitch and causes the aircraft's nose to move up or down [25].

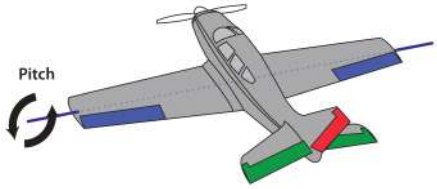

Figure 5.3: Lateral axis (pitch motion) [27].

Longitudinal Axis → Roll

The longitudinal axis is perpendicular to both the vertical and lateral axes, running along the fuselage toward the nose (see Figure 5.4). Motion around this axis is called roll and causes the wingtips to move up and down [25].

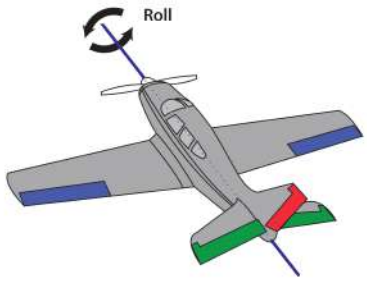

Figure 5.4: Longitudinal axis (roll motion) [27].

5.2.3 Control Surfaces

To control the aircraft's motion around the principal axes, hinged control surfaces are used. During flight, these control surfaces generate aerodynamic forces by deflecting upwards or downwards, acting at their CP. Since they are positioned at a distance from the aircraft's CG, these forces create torques around the principal axes, causing rotation [25].

Control Surfaces: Conventional Aircraft

For conventional aircraft, the control surfaces are defined as ailerons, flaps, elevators and rudder (see Figure 5.5). The ailerons and flaps are located on the trailing edge of the wings, with the ailerons on the outboard section and flaps on the inboard section. The elevators and rudders are located on the tail of the aircraft, positioned on the trailing edge of the horizontal- and vertical- stabilizer, respectively [26].

Ailerons are positioned at the trailing edge of each wing, with one on either side. They operate in opposite directions—when one rises, the other lowers. This creates an imbalance in lift, increasing it on one wing while decreasing it on the other. As a result, the aircraft rolls sideways, enabling it to turn. A well-known issue with ailerons is the phenomenon called adverse yaw, created by the drag generated by the lowered aileron during a turn [27].

Flaps are used to increase lift and drag, improving low-speed performance during takeoff and landing [27].

Elevators provide stability by producing a downward force on the tail and induces pitching motion, making the aircraft climb or descend [27].

Rudder controls yaw, steering the nose of the aircraft left and right. The primary function, however, is to counteract the adverse yaw generated by the ailerons. The rudder corrects this by aligning the nose with the turn, ensuring coordinated flight [27].

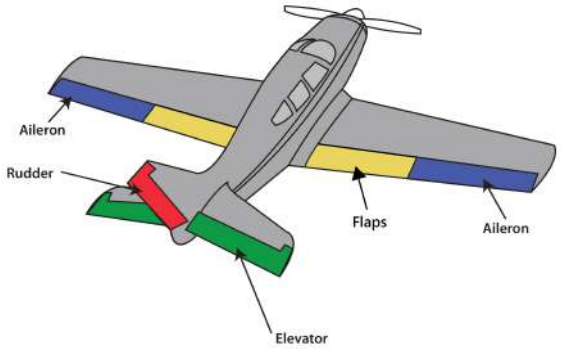

Figure 5.5: Control surfaces on a conventional aircraft. Illustration modified. [27]

Control Surfaces: Tailless Aircraft

For conventional aircraft, lift and control are ensured by separate physical compo-

nents: wings create lift and the vertical and horizontal tail (along with the control surfaces on the tail and wings) regulate the aircraft's movement relative to the air. This is not the case for tailless aircraft. Here, lift and control functions are integrated into a single lifting surface, where control is managed by elevons, and in some cases, flaps (see Figure 5.6) [19], [20].

Elevons are non-conventional control surfaces that extend along the trailing edge of the wings. Unlike traditional aircraft, where separate control surfaces handle pitch and roll, elevons perform both functions simultaneously (the word elevon being a combination of elevator and aileron). Without a Horizontal Tail Plane (HTP), they are essential for maintaining stability and enabling maneuverability in a tailless aircraft, acting as a combined replacement for the horizontal stabilizer, elevator, and ailerons. However, elevons alone cannot compensate for the absence of a vertical tail and rudder, leaving the aircraft without yaw control [19], [20].

Flaps, or split elevons, are sometimes used to create yaw control. By deflecting the flaps on one side of the aircraft, more drag is generated on that wing, inducing yaw motion [20]. In the absence of flaps or other dedicated yaw control surfaces, the aircraft is controlled purely through pitch and roll inputs, relying on coordinated maneuvers to achieve directional changes.

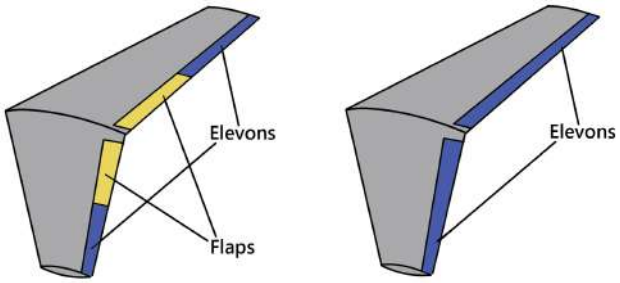

Figure 5.6: Control surfaces on a tailless aircraft. Illustration modified [20].

Dimensioning of Control Surfaces

Control surfaces on conventional aircraft are dimensioned based on size, flight envelope, and the required control authority, typically balancing responsiveness and drag. For tailless designs, elevons handle both pitch and roll control. Full-span elevons are recommended to maximize effectiveness, especially at low Reynolds numbers. A common empirical guideline in light UAV and model aircraft design is to size the total elevon area to approximately one-eighth of the total wing area. Larger control surfaces operated at small deflections are generally preferred for aerodynamic efficiency and reduced drag.

5.3 Stability and control

For safe handling, an aircraft must be stable, controllable, and able to maintain balance across all three axes during flight. Stability and control design is therefore

particularly critical in aircraft development. This is especially true for tailless configurations, where the wing itself must provide both stability and control [30].

Stability refers to the ability of an aircraft to maintain equilibrium. In steady flight, all forces and moments acting on the CG must sum to zero. This is also known as trimmed conditions. Stability is classified into two types: static and dynamic [31].

5.3.1 Static Stability

Static stability is the ability of an aircraft to return to its original position without pilot input after a disturbance, such as a wind gust, affects its angle or speed. Generally, static stability is analyzed for each axis of rotation: longitudinal (pitch)-, lateral (roll)- and directional (yaw) stability. For tailless aircraft, longitudinal stability is the most critical factor since it lacks a tail, which in conventional aircraft provides most of the stability in this axis [31].

Longitudinal (Pitch) Stability

As mentioned before, longitudinal stability is defined as the aircraft's stability in the pitching axis. If an aircraft is longitudinally statically stable, a small change in the angle of attack will create a pitching moment that counteracts the change, returning the aircraft to its equilibrium state [31].

The first condition for longitudinal statical stability is that the pitch stiffness parameter must be negative; $C_{m_\alpha} < 0$. This parameter is the derivative of the pitching moment coefficient (C_m) with respect to the angle of attack (α), as shown in Equation 5.1:

$$C_{m_\alpha} = \frac{\partial C_m}{\partial \alpha} < 0 \tag{5.1}$$

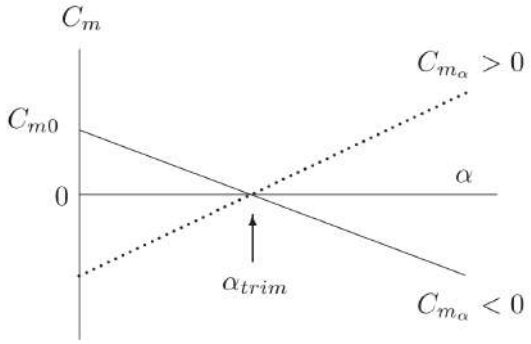

Figure 5.7: Variation of pitching moment with angle of attack [30].

If this condition is satisfied, it implies that as the angle of attack increases, the pitching moment decreases (nose-down moment), returning the aircraft to its trimmed position (a_{trim}). This effect is illustrated in Figure 5.7. In practice, it means that

for a tailless aircraft the CG must be in front of the CP of the aircraft. This can be explained by Equation 5.2, with the expression for C_{m_α} for tailless aircraft:

$$C_{m_\alpha} = (x_{cg} - x_{ac})a_w \tag{5.2}$$

Here, a_w is the lift curve slope of the wing, which almost always positive under normal flight conditions, and $(x_{cg} - x_{ac})$ is the distance between the CG (x_{cg}) and the CP (x_{ac}). Thus, for C_{m_α} to be negative, $(x_{cg} - x_{ac})$ must be < 0 [30].

Satisfying this condition is usually controlled by implementing sweep on the wings [20]. Sweep allows the CP to be moved aft so that the CG is positioned ahead of it (see Figure 5.8). This arrangement ensures static longitudinal stability, which is quantified by the *static margin (SM)*—a measure of how far ahead the CG is located relative to the neutral point (NP). While the CP moves dynamically depending on the angle of attack, NP is the fixed aerodynamic balance point of the entire aircraft. Static margin is calculated using Equation 5.3:

$$SM = \frac{X_{\text{NP}} - X_{\text{CG}}}{MAC} \tag{5.3}$$

where SM is the static margin (typically expressed as a percentage), X_{NP} is the position of the neutral point, X_{CG} is the position of the CG, and MAC is the mean aerodynamic chord. Typical values range from 2% to 10% of MAC, with higher margins providing more stability, and lower margins resulting in increased maneuverability.

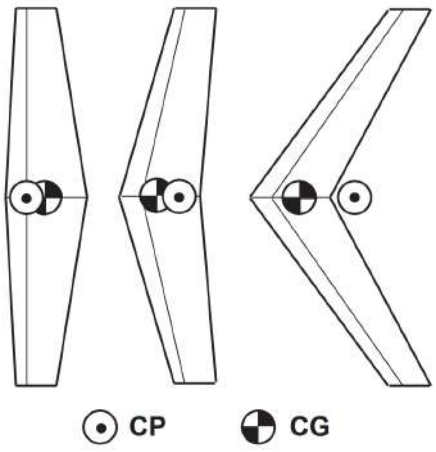

Figure 5.8: Aft movement of CP with an increase in sweep angle [35].

The second condition for longitudinal static stability is that moment at zero angle of attack must be positive (see Equation 5.4):

$$C_{m0} > 0 \tag{5.4}$$

For conventional aircraft C_{m0} is defined by two terms influenced by the main wing and the tail section, respectively, where the term for the main wing is negative and

the term for the tail section is positive. For a tailless aircraft, since there is no tail and thus no positive term, C_{m0} must be made positive by either introducing a reflex airfoil, or by adding wing-twist [33]:

- **A reflex airfoil** is a type of airfoil designed with an upward-curved trailing edge to generate positive pitching moment, resembling the effect of a tail (see Figure 5.9). While reflex airfoils offer a useful solution, they come with drawbacks. They are less efficient than conventional wings and require a higher angle of attack during takeoff [30], [20].

Figure 5.9: Reflexed airfoil [35].

- **Wing-twist** is an alternative to the reflex airfoil configuration and is commonly used in tailless aircraft. It involves sweeping the wing and twisting the tips downward (washout) (see Figure 5.10). When the net lift is zero, the forward section of the wing still generates positive lift while the rear section produces negative lift, resulting in a nose-up (positive) pitching moment. Because there is no tail to provide stability, the aircraft relies on a longer moment arm to maintain balanced flight. Wing sweep effectively increases this arm, helping restore the aircraft to equilibrium after a disturbance. This intentional change in angle along the span is known as geometric twist. A similar effect can also be achieved by using different airfoil sections at the root and tip of the wing, referred to as aerodynamic twist [33].

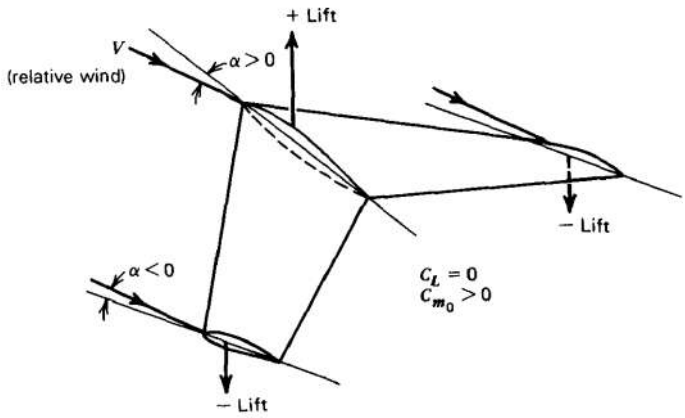

Figure 5.10: Swept-back wing with twisted tips [33].

Lateral (Roll) Stability

Lateral static stability is the aircraft's ability to keep its wings level during flight.

Unlike pitch, the roll axis does not naturally bring the wings back to level if disturbed. Without gravity, an aircraft could stay rolled at any angle without trying to correct itself. This means that, by itself, an aircraft is usually neutrally stable in roll. However, most aircraft are designed to have some natural tendency to return to level flight, mainly because of the dihedral effect. The dihedral effect occurs because of the way gravity interacts with how the aircraft responds to sideways movement, also known as sideslip ($C_{l\beta}$).

A key factor in this effect is the dihedral angle, the upward tilt of the wings compared to the horizontal plane (see Figure 5.11), which helps create a restoring force to level the wings. This makes it a key factor for influencing roll stability [31], [30]. A condition for an aircraft to be laterally stable, is that the positive roll disturbance (ϕ) must generate a negative rolling moment, as shown in Equations 5.5 and 5.6:

$$C_{l_\beta} = \frac{\partial C_l}{\partial \beta} < 0 \tag{5.5}$$

$$C_{l_\phi} = \frac{\partial C_l}{\partial \phi} < 0 \tag{5.6}$$

Here, (C_l) is the rolling moment coefficient, ($C_{l\beta}$) is the sideslip angle and (ϕ) is the roll angle.

Figure 5.11: Dihedral wing [32].

Directional (Yaw) Stability

Directional static stability refers to an aircraft's ability to maintain stability along the vertical axis. A directionally stable aircraft naturally returns to its equilibrium state when subjected to a yawing disturbance (ψ) by generating a restoring yawing moment [31]. To ensure this stability, the derivative of the yaw moment with respect to the sideslip angle (β) must be **positive**, as shown in Equation 5.7:

$$C_{n_\beta} = \frac{\partial C_n}{\partial \beta} > 0 \tag{5.7}$$

For a conventional aircraft, this is done with a longitudinally displaced fin or vertical stabilizer. Here, a sideslip will induce a restorative yawing moment that brings the nose back to the relative air flow. In other words, the aircraft will turn back in to the wind. This poses a challenge for tailless aircraft without a vertical stabilizer. Instead, the effect of a tail is usually made up with vertical fins placed at the wing tips, also known as winglets. This effect can be magnified by adding "toe-in" (a slight inward angle relative to the direction of motion) to the winglets. This causes

the forward-facing winglet to expose a larger portion of its profile to the wind during a yaw, generating significant drag [33], [30]. This creates a restoring yaw moment (see Figure 5.12). Winglets are discussed at length in a later chapter.

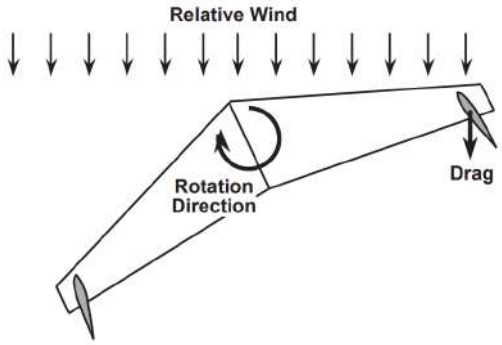

Figure 5.12: Drag on vertical fins creates a restoring yaw moment [34].

Adverse Yaw

Another stability factor connected to both the lateral and directional motion of an aircraft is adverse yaw. Adverse yaw is a common issue where the aircraft yaws opposite to the intended direction of a turn, caused by differential drag between the wings during roll (see Figure 5.13). When elevons (or ailerons) are deflected to initiate a turn, the downward-moving wing produces more lift, which also increases drag, causing the aircraft to yaw in the opposite direction. In conventional aircraft, this effect is countered using vertical stabilizers and rudders [38].

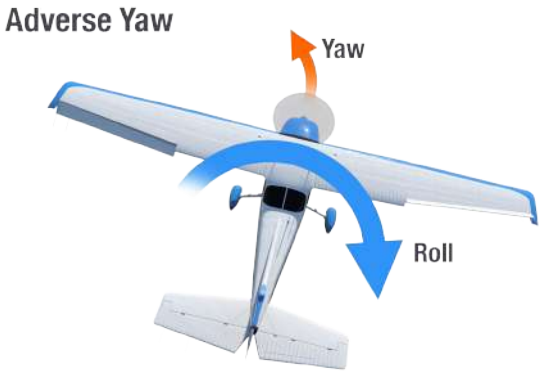

Figure 5.13: The effect of adverse yaw [36].

For tailless aircraft, which lack vertical stabilizers, alternative strategies must be employed to mitigate adverse yaw. One solution is to design the wing with a bell-shaped spanload distribution and integrated wing twist, generating proverse yaw that naturally causes the aircraft to yaw in the same direction as the roll. This technique was notably used in NASA's experimental PRANDTL-D wing (see Figure 5.14) [38]. Other ways to control adverse yaw in tailless aircraft include moving the elevons differently on each side to create more drag on one wing, or using special

flaps at the wingtips, called drag rudders or split elevons, to help turn the aircraft without needing a vertical tail.

Figure 5.14: NASA PRANDTL-D wing [38].

5.3.2 Dynamic Stability

Dynamic stability describes how a vehicle responds over time after being disturbed from its equilibrium state, considering the time-dependent behavior of its motion. This characteristic pattern of motion is called a mode. It implies the presence of resistance to movement, leading to energy dissipation, commonly referred to as positive damping, which makes the aircraft dynamically stable. On the other hand, negative damping implies that the amplitude of the motions will not be dampened, but instead increased over time, making the aircraft dynamically unstable.

Each dynamic stability mode has its own frequency, damping ratio, and time constant, which determine whether the motion is stable or unstable. Notably, static stability does not necessarily ensure dynamic stability [31] [34].

Longitudinal Dynamic Stability Modes

For dynamic stability in the longitudinal axis, there exist two modes: short-period mode and phugoid mode.

Short-period mode is characterized as rapid oscillation in pitch attitude and angle of attack, illustrated in Figure 5.15. It is heavily dampened and settles quickly.

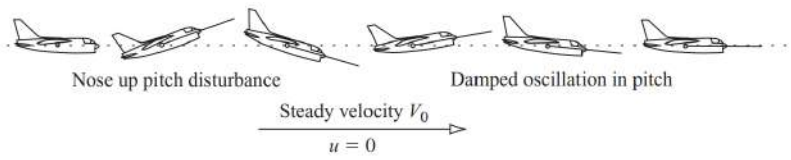

Figure 5.15: A stable short period pitching oscillation [34].

Phugoid mode is a long-period oscillation involving coupled altitude and speed variations. It is weakly damped and slow, resembling a gradual wave-like motion

(see Figure 5.16). This means that the aircraft alternates between gaining and losing altitude while exchanging kinetic and potential energy.

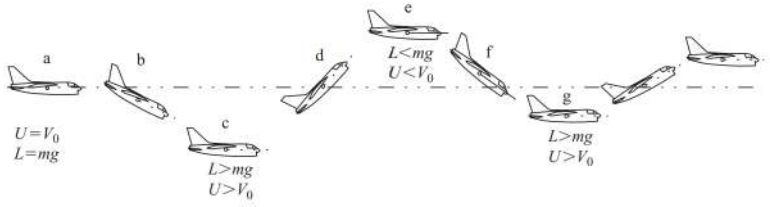

Figure 5.16: The development of a stable phugoid [34].

Longitudinal pitching stability is heavily dependent on the pitch damping derivative C_{mq}, which describes the change in pitch moment due to the pitch rate. This coefficient should be negative (see Equation 5.8), for convergence, generating a nose-down restoring moment that damps and opposes the pitch motion [37] [34].

$$C_{mq} < 0 \tag{5.8}$$

Lateral & Directional Dynamic Stability Modes

For dynamic stability in the lateral and directional axes, there exist two exponential modes; roll mode and spiral mode, and one oscillatory mode; dutch roll mode [31] [37].

Roll mode is a heavily damped rolling motion where the aircraft returns to level flight (see Figure 5.17). It is the quickest of the lateral modes, typically settling in seconds. The frequency of the roll mode is heavily influenced by the roll damping derivative C_{lp} [37].

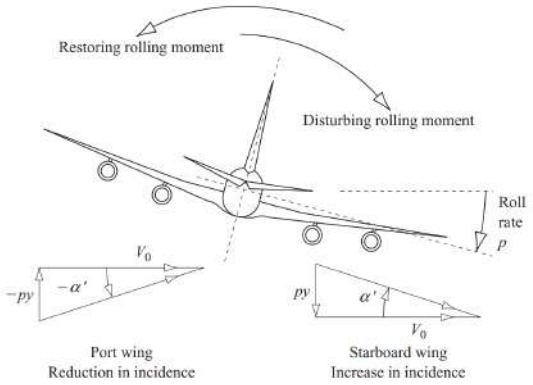

Figure 5.17: Course of motions of the roll mode [34].

Spiral mode is a slow divergence or convergence in bank angle (see Figure 5.18). If this mode is unstable, the aircraft gradually rolls into a spiral dive if left uncorrected. For spiral mode, the dihedral effect is a stabilizing factor. The dihedral effect $C_{l\beta}$

describes the rolling moment caused by the side slip angle. It is one of the most important parameters for lateral and directional stability [37].

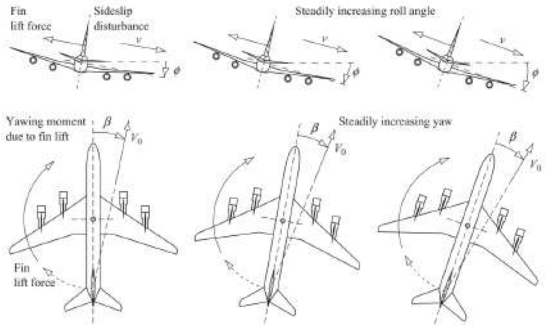

Figure 5.18: Course of motions of the spiral mode [34].

Dutch roll mode is moderately oscillatory motion with intermediate frequency and light damping, characterized by a combination of yawing, rolling, and sideslipping (see Figure 5.19). The dutch roll mode is stabilized by yaw damping, which is influenced by the yaw damping derivative C_{nr}, which describes the change in yaw moment due to the yaw rate. Weathercock stability C_{nb} (often generated by a vertical tail) does also have a stabilizing effect. Hence, dutch roll is a challenge for tailless aircraft [37].

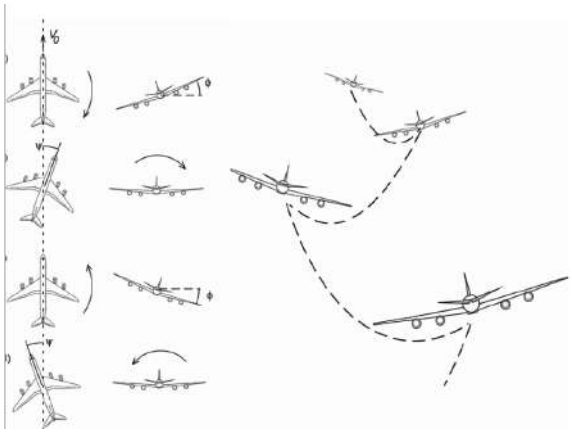

Figure 5.19: Course of motions of the dutch roll mode [31].

As previously mentioned, the roll damping C_{lp}, dihedral effect $C_{l\beta}$, yaw damping derivative C_{nr} and weathercock stability C_{nb} are all important parameters for dynamic lateral and directional stability.

5.3.3 Conclusion of Static & Dynamic stability

To conclude, the static and dynamic stability of a tailless aircraft depend heavily on its aerodynamic design, particularly airfoil reflex, sweep, and CG placement. Carefully balancing these factors is crucial for maintaining controllability and efficiency in flight. Table 5.1 below provides a short summary of the previously discussed parameters, along with their respective stability conditions.

Table 5.1: Stability derivatives and conditions.

Derivative	**Stability Condition**	**Description**
Zero pitch moment C_{m_0}	$C_{m_0} > 0$	Provides inherent nose-up tendency
Pitch stiffness C_{m_α}	$C_{m_\alpha} < 0$	Ensures restoring moment in pitch
Pitch damping C_{m_q}	$C_{m_q} < 0$	Reduces pitch oscillations
Roll damping C_{l_p}	$C_{l_p} < 0$	Stabilizes rolling motion
Roll moment sideslip C_{l_β}	$C_{l_\beta} < 0$	Resists uncommanded roll in sideslip
Yaw stability C_{n_β}	$C_{n_\beta} > 0$	Helps aircraft weathervane into wind
Yaw damping C_{n_r}	$C_{n_r} < 0$	Reduces Dutch Roll oscillations

5.4 Metrics for Aerodynamic Efficiency

5.4.1 L/D Ratio & Glide Polar

Since lift and drag are both aerodynamic forces, their ratio, known as the lift-to-drag (L/D) ratio, serves as a key measure of an aircraft's aerodynamic efficiency. A high L/D ratio indicates that the aircraft either generates significant lift or experiences minimal drag. During cruise, where lift equals weight, a high-lift design enables the aircraft to carry a larger payload. Similarly, because thrust balances drag in steady flight, an aircraft with low drag requires less thrust, reducing fuel consumption or energy demand.

While the L/D ratio represents a single value at a specific flight condition, a broader picture of performance is given by the glide polar. The glide polar is a curve that shows how drag varies with airspeed (or sometimes with lift), allowing identification of the speed at which the maximum L/D ratio occurs. In other words, the L/D ratio is a key point on the glide polar, but the glide polar itself provides a full map of the aircraft's aerodynamic behavior across different speeds [39].

Since thrust is generated by burning fuel or drawing power from an electric energy storage system, lower thrust demands lead to improved energy efficiency. The reduced energy consumption extends endurance, enabling the aircraft to fly longer missions. The L/D ratio is also equivalent to the ratio of the lift coefficient to the drag coefficient [39].

5.4.2 Factors of Aerodynamic Drag

Drag Build-Up

There are two major contributors to the total drag of an aircraft, profile drag and induced drag. Figure 5.20 shows a typical drag breakdown, where it is clear that the skin friction, profile drag and induced drag account for approximately 80% of the total drag. This highlights the importance of trying to decrease these before trying

to minimize other, less significant sources of drag [42].

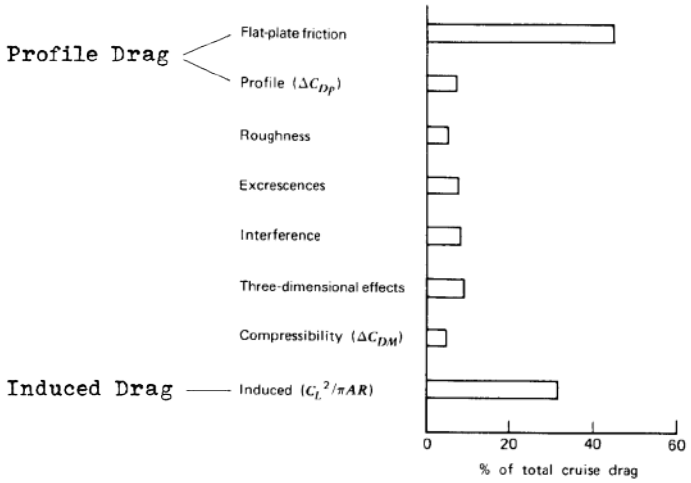

Figure 5.20: Typical drag build-up [42].

Profile Drag

Profile drag refers to the sum of all drag forces acting on airfoil that is not related to the generation of lift. These include skin friction drag, which arises from the friction between an aircraft's surface and the surrounding airflow, and form drag, which results from the aircraft's shape and the way airflow separates around it. Profile drag primarily depends on the airfoil shape, wetted area (the total surface area exposed to airflow), and the angle of attack [42]. Tailless aircraft typically achieve low profile drag, resulting from the absence of a horizontal stabilizer. With a smaller wetted area, these designs experience lower skin friction and form drag, enhancing aerodynamic efficiency [30].

Induced Drag

The other important form of drag is called induced drag, which is the consequence of producing lift in a finite span wing. Generating lift creates a pressure differential between the area above/below the wing. In a finite wing, the air is free to flow from the high pressure region below the wing towards the low pressure region above the wing, ultimately flowing up and around the wing tip, as can be seen in Figure 5.21. This creates a circular air flow around the wing tips [42].

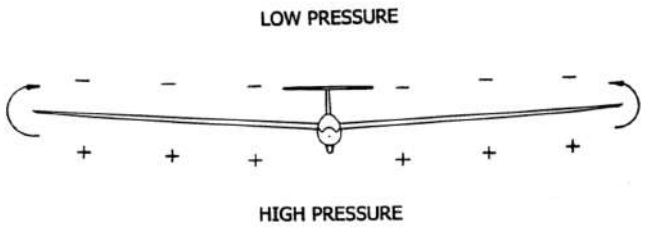

Figure 5.21: Air moving around the wingtip, from the high pressure region on the bottom of the wing to the low pressure region on top of the wing [43].

The pressure differential creates induced opposing spanwise flows on the upper and lower surfaces of the wing. On the underside of the wing the flow is moving outboard, whilst on the overside of the wing the flow is moving inboard. This spanwise flow creates vorticity along the entire span of the wing, which concentrates at the wing tips into two strong wing tip vortices (see Figure 5.22). These produce a downward-moving airflow behind the wing called downwash, which reduces the effective angle of attack, affecting the total lift force and generates induced drag [42].

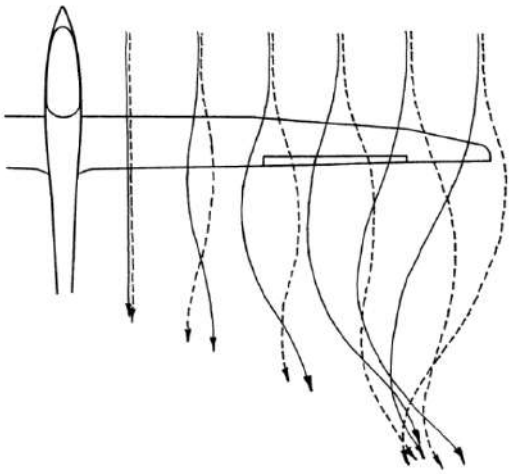

Figure 5.22: Spanwiseflow on a finite wing creating vortices [43].

Induced drag decreases with velocity, making it an important drag factor for slow flying aircraft. It is also directly correlated to the aspect ratio (AR) of the wing. To minimize induced drag, the AR should be maximized. With a higher AR, the lift distribution becomes more efficient across the span of the wing. This generates less intense wing tip vortices since there is less spanwise flow towards the tips [28], [42]. The AR of a wing is the ratio of a wing's length to its chord, calculated by Equation 5.9:

$$AR = \frac{s^2}{A} \tag{5.9}$$

where:

- s = wing span
- A = wing planform area

For reference, a high AR is characterized by long and skinny wings (gliders), and a low AR is characterized by short and stubby wings (fighter jets).

Another effective solution to reduce induced drag is to introduce winglets. Winglets act as a vertical extension of the wing, disrupting the natural vortex formation (see Figure 5.23) [43]. Winglets are not merely a "fence"; they have their own airfoil shape, similar to the main wing. They generate their own aerodynamic load, creating a flow field that interacts with the wing's airflow in a way that reduces overall

spanwise flow. This approach effectively minimizes induced drag by leveraging aerodynamic principles rather than simply blocking airflow [43].

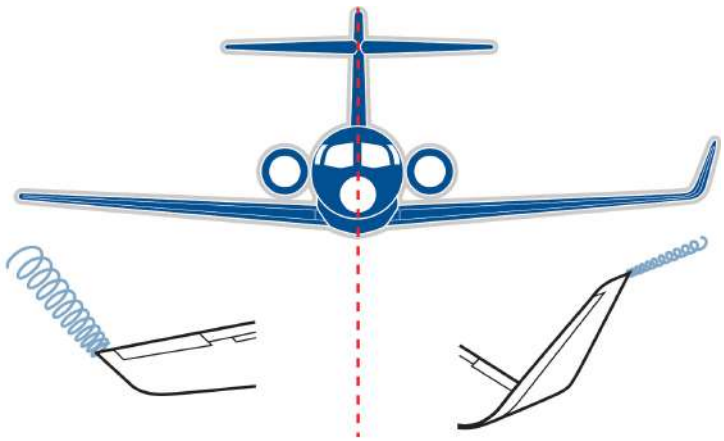

Figure 5.23: Winglets used to disrupt the natural vortex formation [44].

5.4.3 The Flight Envelope

The flight envelope defines the safe operating range of an aircraft in terms of speed and thrust. It is the region in the velocity-altitude plane that encompasses all possible level-flight conditions. Figure 5.24 illustrates the Thrust and Drag vs. Velocity plot, indicating key speed limits [22].

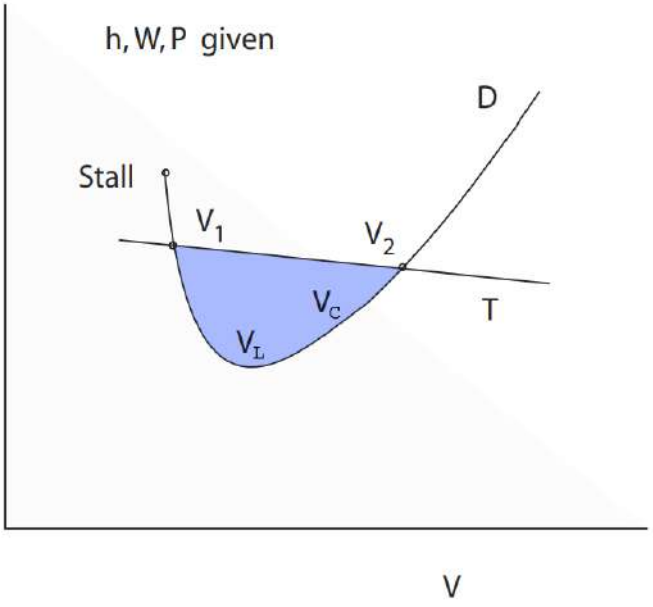

Figure 5.24: Thrust and Drag versus Velocity. Flight envelope marked in blue. Illustration modified [22].

- **Stall Speed** (V_1): The minimum speed required to maintain level flight. Below this speed, the aircraft stalls due to insufficient lift.

- **Minimum Drag Point**: The lowest point on the drag curve, representing the speed at which the aircraft experiences minimal aerodynamic resistance, maximizing efficiency.
  - **Loiter speed** (V_l) is located at this point, as it corresponds to the speed requiring the least amount of thrust to maintain level flight, maximizing endurance.
  - **Cruise speed** (V_c) is often slightly higher than loiter speed, balancing energy consumption and range.
- **Maximum Level Flight Speed** (V_2): The highest speed at which thrust equals drag. Beyond this, the aircraft cannot accelerate further.

Stall Speed Calculation

The **stall speed** (V_s) is the minimum speed at which an aircraft can sustain steady, level flight without losing altitude. It is measured in meters per second (m/s) and depends on several factors, including the aircraft weight, air density, wing area, and the maximum lift coefficient [22]. The stall speed is given by Equation 5.10:

$$V_s = \sqrt{\frac{2W}{\rho S C_L^{\max}}} \tag{5.10}$$

where:

- V_s = Stall speed (m/s)
- W = Aircraft weight (N)
- ρ = Air density (kg/m^3)
- S = Wing reference area (m^2)
- $C_L^{\max}$ = Maximum lift coefficient of the wing (dimensionless)

This equation shows that stall speed increases with greater aircraft weight and decreases with higher air density, larger wing area, or a higher maximum lift coefficient [22].

Flight Endurance

Endurance refers to the total time an aircraft can remain airborne before depleting its available power. It is typically measured in minutes or hours. Maximizing endurance is achieved by flying at the optimal loiter speed, which corresponds to the point where the aircraft requires the least power to sustain level flight. The optimal loiter speed occurs when:

$$\frac{C_L^{3/2}}{C_D} \quad \text{is maximized.}$$

At this speed, the aircraft operates at its most energy-efficient state, allowing for prolonged flight duration [22], [41]. Endurance can be calculated using:

$$Endurance = \frac{E_{\text{battery}}}{P_{\text{tot}}}$$

where:

- E_{battery} = Total energy available from the battery (Wh or J)
- P_{tot} = Total power consumption (W)

The total power consumption of the drone consists of the power required for propulsion and the power consumed by onboard systems [4]. It can be defined as:

$$P_{\text{tot}} = \underbrace{F \cdot V}_{P_{\text{prop}}} \cdot \frac{1}{\eta_{\text{propulsion}}} + P_{\text{os}}$$

where:

- P_{tot} = Total power consumption (W)
- P_{prop} = Power required by the propulsion system (W)
- F = Drag force acting on the drone (N)
- V = Velocity of the drone (m/s)
- $\eta_{\text{propulsion}}$ = Efficiency of the electric propulsion system (dimensionless, $0 < \eta \leq 1$)
- P_{os} = Power draw from the onboard systems (W)

Since the power required for propulsion (P_{prop}) is directly proportional to the drag force (F) and velocity (V), optimizing aerodynamics and propulsion efficiency can significantly extend endurance.

Flight Range

Range is the total horizontal distance an aircraft can travel before exhausting its available power, typically measured in meters or kilometers (m, km). Achieving maximum range involves flying at the cruise speed, which corresponds to the speed for which the aircraft has it's maximum L/D ratio. A higher L/D ratio indicates greater aerodynamic efficiency, meaning the aircraft generates more lift relative to drag, thereby requiring less power per unit distance traveled [39], [40]. The range of an aircraft is given by:

$$\text{Range} = V_{\text{ground}} \times \text{Endurance}$$

where:

- V_{ground} = Ground speed of the aircraft (m/s)
- Endurance = Total flight time before running out of energy (seconds, minutes, or hours)

To achieve maximum range, the aircraft must operate at its cruise speed (V_c). Therefore, the endurance value used in this equation must be calculated specifically for the cruise speed, as it ensures the most efficient energy usage per unit distance traveled.

5.5 Winglets

The primary purpose of winglets has traditionally been to reduce induced drag by counteracting downwash. However, in tailless aircraft, winglets serve mainly as a tool for enhancing directional stability, with the reduction in induced drag being a

beneficial secondary effect. Winglets act similarly to vertical stabilizers, helping the aircraft resist unwanted yaw motions caused by disturbances.

5.5.1 Types of Winglets

For small tailless UAVs, the most common winglet types are blended winglets and split winglets. These designs aim to balance aerodynamic efficiency, stability, and practical considerations like ground clearance and durability.

Blended Winglet

Blended winglets are smoothly curved extensions that transition gently from the wing to the winglet without sharp angles (see Figure 5.25). This gradual curve minimizes interference drag between the wing and winglet junction, improving aerodynamic efficiency.

The design offers several advantages. It reduces interference drag, improves aerodynamic performance across a wide range of angles of attack, and enhances directional stability. However, it also comes with some drawbacks. The structure is slightly more complex to manufacture compared to simpler angled designs and may lead to increased structural loads at the wingtip.

Figure 5.25: A blended winglet on a Boeing 737 [46].

Split Winglet

Split winglets, also known as dual or scimitar winglets, feature both upward- and downward-facing surfaces (see Figure 5.26). This configuration is designed to improve the efficiency of vortex control at the wingtips beyond what is possible with a single surface. The upper section resembles a blended winglet, while the lower section further reduces induced drag by redirecting and weakening the wingtip vortices.

This configuration provides enhanced drag reduction compared to single winglets and offers improved yaw stability and control. On the downside, it features a more

complex geometry and structure, and for small UAVs, there's an increased risk of damage to the lower surface during landings.

Figure 5.26: A split winglet on a Boeing 737 MAX [46].

The choice of winglet design is not only influenced by aerodynamic performance but also by operational considerations. For small UAVs, upward-facing winglets such as blended designs are generally preferred over downward-facing ones. This is mainly to avoid damage during take-offs and landings, where limited ground clearance could otherwise result in impacts to downward-angled winglets [45].

5.5.2 Winglet Design

Geometry

For a blended winglet design, the main design variables can be seen in Figure 5.27. Below is the complete list of variables used in this project:

- **Cant Angle** - Describes how much the winglet is tilted outwards or inwards from the wingtip. A positive cant angle, where the winglet is tilted away from the fuselage, helps redirect the wingtip vortex flow away from the main wing's wake [43].
- **Toe Angle** - The horizontal rotation of the winglet's base relative to the wing's direction [43]. Toe-in causes the forward-facing winglet to expose a larger portion of its profile to the wind during a yaw, generating significant drag, which creates a restoring yaw moment. Toe-out works by the same principle but creates additional lift instead on the rear-facing winglet. Generally, drag is easier to predict than lift, making toe-in the preferred design [35].
- **Twist Angle** - The variation of the angle of attack along the span of the winglet. This can improve the wing's lift distribution by reducing the strength of vortices [43].
- **Sweep Angle** - Refers to the angle at which a winglet is inclined relative to the wing's chord line.
- **Taper Ratio** - The ratio of the root and tip chord lengths.
- **Winglet Span** - The vertical extension of the winglet.
- **Airfoil** - The airfoil profile used for the winglet.

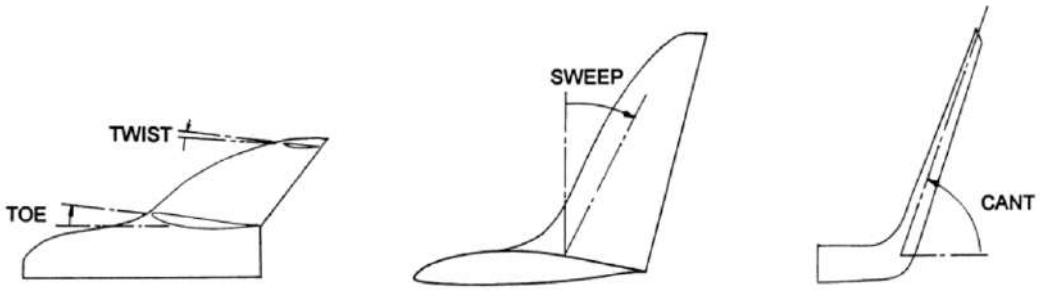

Figure 5.27: Geometry used to define a winglet [43].

Design Guidelines

Approximate recommended values for the blended winglet geometries can be seen in Table 5.2 below.

Table 5.2: Winglet Design Parameters [47], [48].

Cant	Toe	Twist	Sweep	Taper	Span	Airfoil
15°	-2° to 3°	0° to -2°	30° to 50°	0.2 to 0.5	5 to 10% of wing span	NACA 0012, NACA 2412

6

Critical Design Considerations for Low Reynolds Number Flight

Unmanned Aerial Vehicles (UAVs) operating at low speeds and small sizes often fly in regimes characterized by low Reynolds numbers (Re), typically below 500,000. Flight in this domain presents distinct aerodynamic challenges that must be addressed through careful design. This chapter outlines the primary considerations to ensure aerodynamic efficiency, stability, and control in low Reynolds number flight conditions.

6.1 The Reynolds Number

Reynolds number (Re) is a dimensionless quantity used to predict how air flows around an object, such as a wing or airfoil. It helps determine whether the airflow will be laminar or turbulent, which directly impacts lift, drag, and overall aerodynamic efficiency [49]. Smooth airflow over the wing generates significantly more lift than turbulent airflow. The Reynolds number (Re) is calculated as:

$$Re = \frac{\rho V L}{\mu}$$

where:

- ρ = Air density ($\tilde{1}.225$ kg/m^3 at sea level)
- V = Velocity of the aircraft (m/s)
- L = Characteristic length (typically chord length for wings, in meters)
- μ = Dynamic viscosity of air (1.81×10^{-5} kg/m $\cdot$ s)

Reynolds numbers for jet aircraft typically range from 10^7 to 10^8, while model aircraft and many UAVs operate at much lower Reynolds numbers, typically between 10^3 and 10^5 (see Figure 6.1) [32].

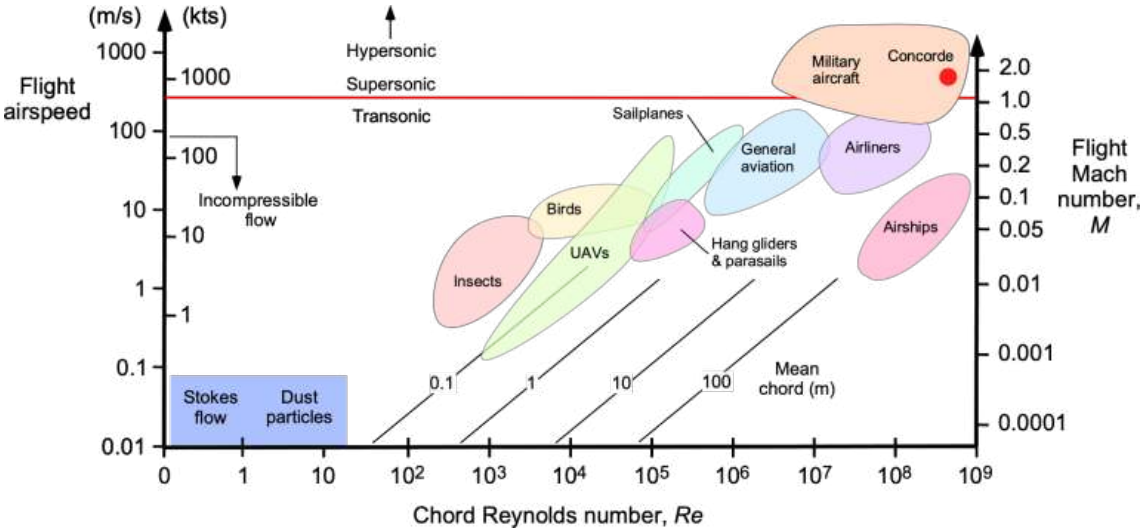

Figure 6.1: Summary of the range of Reynolds encountered by various flight articles [32].

At higher Reynolds numbers (e.g., higher speeds or larger wings), aerodynamic efficiency improves as inertial effects dominate viscosity, reducing profile drag. Conversely, at lower Reynolds numbers, thicker boundary layers increase viscous effects, leading to higher profile drag and a lower L/D ratio [32].

A boundary layer is the thin region of air near a surface where viscous forces significantly influence the flow (see Figure 6.2). At higher Reynolds numbers, boundary layers remain thin and more stable, minimizing drag. However, at lower Reynolds numbers, boundary layers thicken, increasing friction drag and making flow more prone to separation, which reduces aerodynamic efficiency [32].

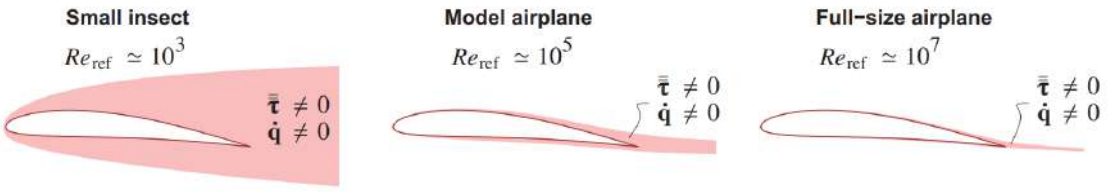

Figure 6.2: Boundary layer thickness at different reynolds numbers [50].

To summarize, the main aerodynamic challenges at low Re are:

- Higher drag due to increased viscosity effects.
- Lower lift coefficient (Cl) → Wings generate less lift per unit area.
- Flow separation occurs earlier → Leads to stall and efficiency losses.

6.1.1 Airfoil Selection For Low Re

Airfoils designed for high Reynolds numbers, such as the NACA 4-digit series, typically perform poorly in low Reynolds number conditions due to thick boundary layers and early flow separation. In the low Re regime, selecting a suitable airfoil

becomes a critical design consideration. Airfoils for small UAVs should generally be:

- Thin, to delay boundary layer separation and reduce profile drag.
- Cambered (see Figure 6.3), to generate sufficient lift at low speeds and low angles of attack.

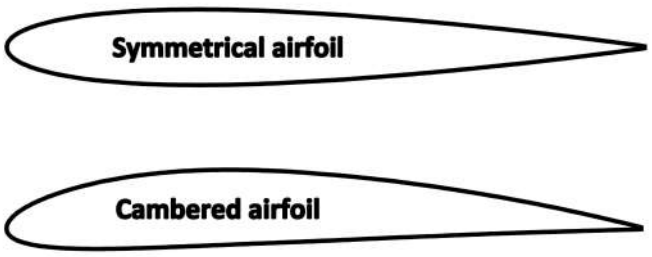

Figure 6.3: Symmetrical and cambered airfoil.

6.1.2 Aspect Ratio

High AR wings, characterized by their long and slender shape, are effective at reducing induced drag, which becomes a dominant source of drag at low speeds. This reduction contributes to a higher L/D ratio, making such wings highly favorable for endurance-focused missions where maximizing flight time and energy efficiency is critical.

However, high AR wings can introduce structural challenges, such as increased wing bending and reduced roll rates.

6.1.3 Additional Drag Reduction Strategies

To reduce drag while operating in low Re, these additional strategies can be applied:

- Minimize frontal area: Streamlined shapes and integrated fuselage designs reduce form drag.
- Surface smoothness: Rough or porous surfaces increase skin friction. Post-processing is needed for 3D printed/foam wings to improve surface finish.
- Gap sealing: Reducing control surface hinge gaps prevents additional drag.

7
Benchmarking

7.1 Selection of Reference UAVs

To guide the early design phase, a benchmarking study was conducted on lightweight fixed-wing drones with the potential to meet the sub-250 g requirement. The focus was primarily on airframe characteristics, since the required functionality would be defined separately through selected electronics. Particular attention was given to aerodynamic layout, stability solutions, structural weight, and material choices. In cases where example setups (motor, ESC, propeller configurations, etc.) were available, these were noted to provide context on achievable flight performance.

Early estimates from the optimized BOM suggested an available weight budget of 50 to 100 grams for the airframe. Therefore, airframe weight was used as the primary parameter when identifying suitable references. A total of eight tailless fixed-wing drones with airframe weights in this range were selected. These were all considered capable of fulfilling the performance requirements when paired with lightweight hardware. For comparison, the original SSRS 900 g drone and a scaled-down 250 g version were also included.

7.2 Benchmarking Criteria

Key parameters extracted from the flight mechanics chapter were used to structure the benchmarking:

- Planform type
- Yaw stability solution
- Pitch stability solution
- Span (mm)
- Length (mm)
- Wing area (dm^2)
- Wing tip chord (mm)
- Wing root chord (mm)
- Sweep angle (degrees)
- Dihedral/anhedral angle (degrees)
- Wing twist (washout) angle (degrees)
- Taper ratio
- AR

- Airframe weight (g) and material

In addition, supplementary performance metrics such as estimated stall speeds, cruising speeds, endurance, and example propulsion setups were added when available. Table 7.1 below shows the benchmarking table.

Table 7.1: Extract of benchmarking table summarizing key airframe parameters. The full table is available in Appendix A.4.

Specs. \ Name		SSRS 900g Drone	FLIK Wing	Nano Goblin	ZOHD Dart
					
General notes		For comparison. What design parameters can be carried over?	Good stability. Flies better at low speeds than the Goblin. Plenty space for electronics. Low airframe weight.	Good flight char. Easy to fit electronics. A bit too heavy.	Good flight char. Easy to fit electronics. Too heavy.
Airframe					
Planform type		Delta wing	Delta wing w. fuselage	Plank wing w. fuselage	Plank wing w. fuselage
Yaw Stability		Winglets	Winglets	Vertical fins	Vertical fins
Pitch Stability			Elevons for reflex. Elevons angled up as ordinary position. Underside of elevons is close an to top of wing	PW-series airfoil "virtually 0 pitching moment". Elevons for reflex	-
Span	mm	850	500	580	570
Length	mm	520	300	390	379
Wing area	dm^2	21,4	8	7,6	7,6
Outer chord	mm	180	125	105	110
Inner chord	mm	300	220	158	190
Sweep	deg	36	32	0	0
Dihedral/anhedral	deg	2.5 deg anhedral			
Twist	deg	-2.5 deg			
Taper ratio		0,60	0,57	0,66	0,58
Aspect ratio		3,38	3,13	4,43	4,28
Airframe weight	g	300	48	70	89
Material		EPP Foam	EPP Foam	EPP	EPP w. CF spar

7.3 Key Findings and Design Implications

The benchmarking highlighted several consistent trends among lightweight fixed-wing UAVs:

- **Wing area and AR:** Successful designs generally had wing areas between 8–9.5 dm^2. AR ranged from 2.7 to 5.4, with higher AR correlating with improved endurance at the cost of reduced maneuverability.
- **Wing planform and layout:** Most drones featured a pure flying wing- or delta wing- configuration, with slight body blending. This improves the L/D ratio and reduces structural weight, but makes it more difficult to place hardware. Other designs incorporated fuselages to improve electronics integration.
- **Stability solutions:** Yaw stability was typically achieved using small winglets or vertical fins placed near the fuselage. Pitch stability was handled either through airfoil selection (reflexed airfoils) or by slight geometric washout in the wing design.
- **Sweep and dihedral angle:** Sweep angles around 30 to 35 degrees were common, improving longitudinal stability and shifting the center of pressure aft. A few drones incorporated slight anhedral angles (2 to 2.5 degrees) to increase roll maneuverability.

- **Material choices:** Lightweight EPP foam or foamed Z-foam was the dominant construction material.

Overall, the benchmarking reinforced the importance of maximizing wing area relative to mass, using simple aerodynamic layouts with effective stability solutions. These insights directly influenced the early concept development and design decisions made in the following chapters.

8

Early Concept Development

This chapter marks the transition from research to initial design. It begins with Bill of Materials (BOM) optimization to define the airframe weight budget, followed by a configuration study that leads to the selection of a blended wing body layout. Key aerodynamic parameters such as wing area, airfoil, and stability are then defined, and the resulting concept is evaluated through XFLR5 and OpenVSP analysis.

8.1 BOM Optimization

To determine the specific weight allocation for the airframe, the current BOM for the SSRS 900 g drone was optimized for a smaller-scale aircraft, implementing several reductions while maintaining functionality:

- **Airframe:**
  - Downsized main spar (−9 g).
  - Downsized elevon linkage (−4 g) by using shorter linkages and connectors, inspired by benchmarked drones.
- **Carrier board:**
  - Removed battery management system (BMS) (−5 g), requiring batteries to be disconnected for charging.
  - Integrated printed circuit board (PCB) (−4 g).
  - Removed unnecessary BMS connectors.
- **Electronics:**
  - Switched to smaller elevon servos (−17.8 g), based on benchmarked drone setups.
  - Switched to 2S Li-Ion 4000mAh batteries (−192 g).
- **Propulsion system:**
  - Downsized motor (−41.3 g).
  - Switched to a smaller ESC (−8.1 g) to match reduced power requirements.
  - Downsized propeller (−5.95 g).
- **Payload system:**
  - Replaced gimbal actuators with two smaller servos (−5 g).

These optimizations result in an estimated 50 g of available weight for the airframe body, ensuring the design remains within the 250 g limit while meeting performance requirements.

A detailed BOM listing the selected components is available in Appendix A.3.

8.2 UAV Configuration Decision Matrix

Several tailless UAV configurations (see Figure 8.1) were identified during the benchmarking process:

1. **Pure Flying Wing:** The whole airframe consists of a swept back wing.
2. **Blended Wing Body:** Like a flying wing, but with an extended root chord.
3. **Plank Wing with Fuselage:** Straight wing with a fuselage.
4. **Delta Wing with Fuselage:** Similar to a flying wing, but with the addition of a fuselage.

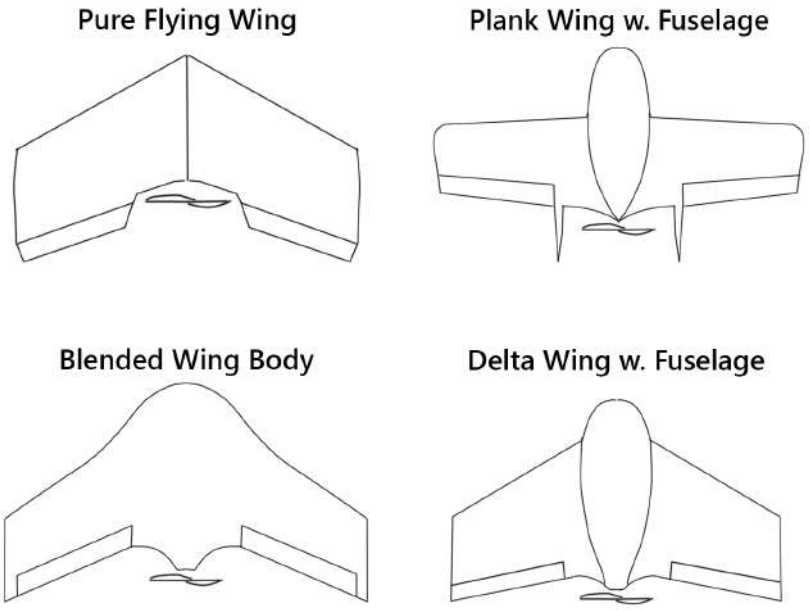

Figure 8.1: UAV layouts.

To compare these configurations and determine the most suitable option for this project, a decision matrix was created. Each selection criterion was weighted based on its importance to project success, ensuring a structured evaluation. The UAV configurations were then assigned scores for each criterion, which were summed to produce a total score for ranking.

The evaluation criteria included:

1. **Weight efficiency:** How well the design minimizes mass while maintaining structural integrity.
2. **Space allocation for components:** The ability to accommodate essential electronics, batteries, and payloads within the airframe.
3. **Aerodynamic efficiency:** How effectively the airframe reduces drag and produces lift.

4. **Stability:** How well the airframe stabilizes in flight.
5. **CG tolerance and adjustability:** The ability to balance and fine-tune the CG within the airframe.
6. **Manufacturing feasibility:** The ease of constructing the airframe using scalable, cost-effective production methods.

By systematically scoring each UAV configuration against these criteria, the most suitable design for the project was selected. These scores are summarized in Table 8.1 below:

Table 8.1: Comparison of UAV configurations based on weighted criteria.

Criteria	**Max score**	**Pure wing**	**Delta wing + fuselage**	**Blended Wing Body**	**Plank wing + fuselage**
Weight Eff.	25	25	18	22	15
Space Allocation	20	12	20	18	20
Aerodynamic Eff.	20	20	15	19	15
Stability	15	10	15	13	12
CG	10	5	10	7	7
Manufacturing	10	8	7	5	9
Total	100	80	85	84	78

The decision matrix revealed that the *Delta Wing with Fuselage* received the highest score, closely followed by the *Blended Wing Body*. The fuselage provides advantages in space allocation and stability, making it easier to fit components and balance the CG. However, it adds drag and weight, reducing aerodynamic efficiency. In contrast, the *Blended Wing Body* maintains high efficiency and a low weight, as the entire wing contributes to creating lift. Additionally, it allows for complete analysis in XFLR5, making aerodynamic modeling more straightforward. Despite these benefits, it is more challenging to manufacture and has limited ability for adjusting CG placement to maintain stability.

Given the focus on aerodynamic efficiency and low weight, the *Blended Wing Body* was selected for further development. It has an efficient lift distribution and is compatible with XFLR5, which makes accurate performance analysis possible. Despite challenges in manufacturing and limited space for components, it offers the most potential for high aerodynamic performance within the weight constraint.

8.3 Calculation of Necessary Surface Area

The total mass of the drone is set to 250 g. To ensure sufficient lift for a stall speed of 8 m/s, the required wing surface area is calculated using the equation for lift:

$$L = \frac{1}{2}\rho V^2 S C_L$$

where:

- L is the lift force,
- $\rho = 1.225\,\mathrm{kg/m^3}$ is the air density,
- $V_{\text{stall}} = 8\,\mathrm{m/s}$ is the stall speed,
- S is the wing surface area,
- C_L is the coefficient of lift, usual values range 1.2 - 1.5.

Since the drone must generate lift equal to its weight $L = mg$, the required wing surface area is derived as:

$$S = \frac{2mg}{\rho V^2 C_L}$$

Substituting values:
- For $C_L = 1.2$:

$$S = \frac{2 \times (0.250 \times 9.81)}{1.225 \times 8^2 \times 1.2} = 5.2\,\mathrm{dm^2}$$

- For $C_L = 1.5$:

$$S = \frac{2 \times (0.250 \times 9.81)}{1.225 \times 8^2 \times 1.5} = 4.2\,\mathrm{dm^2}$$

Thus, the minimum required wing surface area for a stall speed of 8 m/s is approximately 5 dm².

8.3.1 Airfoil Selection

At this scale, minimizing wing drag is primarily influenced by the thickness-to-chord ratio (t/c) and AR. Therefore, the airfoil should have the lowest possible t/c to reduce drag effectively. Preferably, the t/c ratio should be under 10%, meaning the maximum thickness of the airfoil is 10% of the chord.

Four airfoils were identified based on their thin profiles and suitability for low Reynolds number conditions (about 250,000, corresponding to an 180 mm chord at 20 m/s):

- MH60 – 10.08%
- HS522 – 8.67%
- PW51 – 8.9%
- PW75 – 8.9%

These airfoils were analyzed using XFLR5 at a Reynolds number of approximately 250,000. Three plots were generated to evaluate their performance, as can be seen in Figure 8.2:

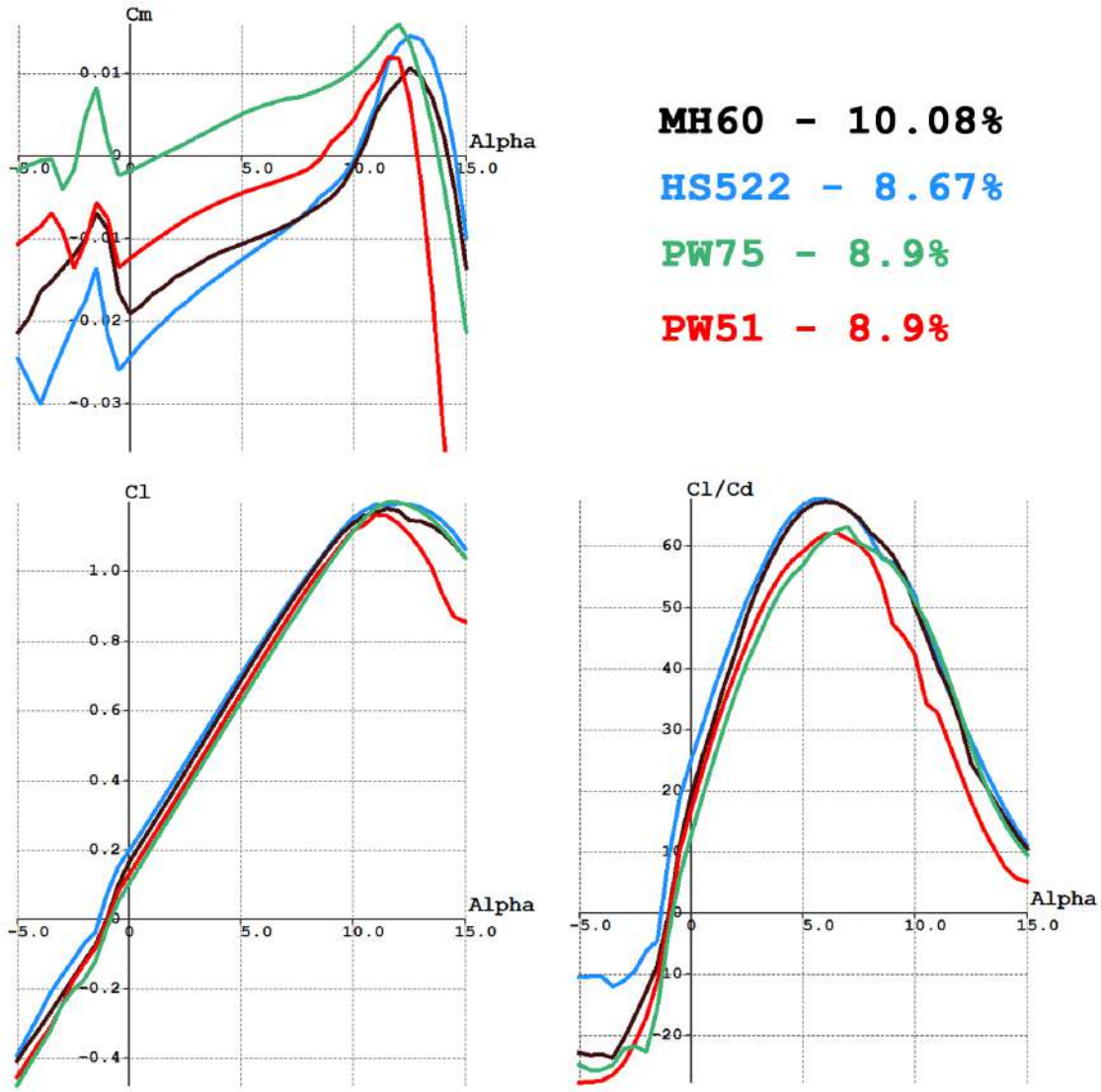

Figure 8.2: Performance parameters vs alpha.

Lift (C_l) vs Alpha:
All four airfoils demonstrate similar lift behavior up to the stall region. HS522 and MH60 reach the highest peak C_l, just above 1.1, followed closely by PW51 and PW75. PW75 stalls slightly earlier and more abruptly.

C_l/C_d vs Alpha:
HS522 exhibits the highest peak efficiency, followed closely by MH60 and PW51. PW75 performs slightly worse in terms of efficiency, with a peak C_l/C_d around 5.8–6.0. All airfoils peak between 5° and 7° AoA.

C_m vs Alpha:
MH60 and HS522 have consistently negative C_m, making them naturally stable. PW51 has a lower negative C_m, offering a middle ground between stability and efficiency. PW75 stands out with a near-zero to slightly positive C_m over the operating range, indicating neutral or slightly unstable behavior, which is highly relevant for

tailless configurations.

PW75 – Selected Airfoil

The PW75 airfoil was selected due to the following key advantages:

- Thin profile: At 8.9% t/c, it provides sufficient internal volume while maintaining low profile drag, making it suitable for sub-250 g aircraft.
- High aerodynamic efficiency: PW75 exhibits a competitive L/D ratio and similar maximum lift coefficient (C_{lmax}) compared to the other candidates.

However, what makes the PW75 especially attractive for this design is its near-zero pitching moment (C_m=0) for varying angles of attack. In a tailless configuration, like a flying wing, this is highly desirable because a near-zero pitching moment means the airfoil doesn't naturally pitch up or down, reducing the need for constant trimming. This minimizes drag from control surface deflections (e.g., elevons) and allows the lift vector to remain more vertical, leading to better lift efficiency. It also simplifies aerodynamic balancing, meaning that the pitching stability can be achieved through geometric wing twist (washout), rather than relying solely on airfoil stability or control inputs.

By accepting a slightly unstable airfoil and managing stability via wing twist, the overall wing becomes more aerodynamically effective.

8.3.2 Initial Design Choices

The benchmarked drones has a wing area of about 8 dm², notably larger than the minimum required value for sufficient lift at 8 m/s for a mass of 250 g. Thus, following the rough design layout of these drones will provide a large enough wing. The benchmarking analysis revealed that many design parameters are consistent across tailless configurations within the sub-250 g scale, where the airframe body weight is approximately 50 g. The following common characteristics were identified:

- Wingspan: 500–550 mm
- Root chord: 200–220 mm
- Tip chord: 125–130 mm
- Wing area: 8–8.5 dm²
- Taper ratio: 0.58–0.63
- AR: 2.9–3.8
- Wing loading: 30 N/m²
- Sweep angle: 30–35°

Notably, the taper ratio and AR closely resemble those of the SSRS drone. However, the SSRS drone differs in having a higher sweep angle and greater wing loading. A higher sweep angle is advantageous for high-speed flight, but at low speeds, it introduces higher drag and lower lift efficiency. Similarly, higher wing loading enhances stability in windy conditions but makes low-speed flight more challenging. Given

the slow-speed flight requirements and small-scale constraints, it is logical to design the drone in alignment with the benchmarked UAVs, optimizing for efficiency and controllability at lower speeds. As a initial design, the dimensions were thus set to:

- Wingspan: 500 mm
- Root chord: 205 mm
- Tip chord: 125 mm
- Sweep angle: 32
- Wing area: 8.2 dm^2
- Taper ratio: 0.6
- AR: 3.0
- Wing loading: 30 N/m^2

With the initial drone design completed, the next step was to accommodate the internal components by increasing the root chord and blending the midsection into the wing.

Root Chord
A critical aspect of sizing the drone is ensuring sufficient internal volume for the components while maintaining structural integrity. The thickest components are the 18650 Li-Ion batteries, which have a diameter of 18 mm and a length of 65 mm. To safely house the batteries, an internal thickness allowing for 5 mm clearance both above and below the batteries was required, resulting in a minimum internal thickness of 28 mm. Given the PW75 airfoil's thickness-to-chord ratio of 8.9%, achieving the necessary internal thickness would require a root chord of approximately 314 mm, calculated as:

$$\text{Root chord} = \frac{28 \text{ mm}}{0.089} \approx 314 \text{ mm}$$

Body/Wing Blend
Drawing inspiration from the benchmarked SSRS 900 g drone, the body/wing blend section was designed to cover approximately 30% of the total wingspan. This configuration ensures ample internal volume for housing components while also promoting smoother airflow over the central part of the wing. To enhance safety and crash resilience, the blended section was further divided into three parts, allowing for a rounded and more impact-tolerant front profile.

8.3.3 Stability

Pitch

As discussed earlier, for tailless aircraft, pitch stability can be achieved through two primary methods: reflexed airfoils or wing twist (washout). The PW75 airfoil has a slight reflex, but geometric wing twist (physically twisting the wingtips) is needed to add additional pitch stability. The Panknin twist formula provides a rough estimation of the required wing twist to achieve pitch stability in tailless

aircraft. It is particularly useful for determining the amount of geometric twist needed to balance the pitching moment and ensure stable flight. The required twist is influenced by factors such as flight speed, Reynolds number, airfoil characteristics and the static margin. For this drone, calculations were performed at two different flight speeds using PW75 airfoil data at the corresponding Reynolds numbers.

Twist needed according to the Panknin twist formula:

- Stable flight at 25 m/s -> Twist required: -2.44°
- Stable flight at 20 m/s -> Twist required: -8.26°

These results indicate that at higher speeds, less twist is required for stability, while at lower speeds, significantly more twist is needed due to changes in aerodynamic forces. In addition to the Panknin twist calculations, analysis was done in XFLR5 to determine the exact wing twist needed for stable flight at various speeds.

Twist needed according to XFLR5:

- -2 degrees: Stable flight at 22.77 m/s (AoA 1.49 deg)
- -3 degrees: Stable flight at 21.68 m/s (AoA 1.75 deg)
- -4 degrees: Stable flight at 19.92 m/s (AoA 2.26 deg)
- -5 degrees: Stable flight at 18.47 m/s (AoA 2.78 deg)

A twist of -3 deg was chosen as it keeps the stable flight close to the cruise speed of 20 m/s, whilst requiring a relatively low angle of attack.

Yaw

Winglets are incorporated to enhance yaw stability, following established design guidelines. The selected parameters are:

- Cant angle: 15°
- Taper ratio: 0.5
- Sweep angle: 45°
- Span: 10% of total wingspan (50 mm)
- Airfoil: Thin symmetric profile (NACA 0007)

Roll

Roll stability is mainly provided by the 32° wing sweep. When the drone experiences a sideslip, the windward wing gets more airflow than the leeward wing, creating more lift on one side. This causes the drone to roll back against the sideslip direction, helping it stay level. In this way, the wing sweep acts like dihedral and improves roll stability.

8.3.4 CG Positioning

A 10% static margin was selected to ensure stability during the initial test flights. A lower static margin may be chosen later to improve maneuverability once the

aircraft's handling characteristics are well understood. To achieve a 10% static margin, the CG was determined using Equation 8.1:

$$X_{CG} = X_{NP} - (SM \times MAC) \tag{8.1}$$

where:

- X_{CG} = CG position in the longitudinal-axis (X-axis)
- X_{NP} = Position of the neutral point (NP), the aerodynamic center of the entire aircraft, in the longitudinal-axis (X-axis)
- SM = Static margin, set to 0.10 (10%)
- MAC = Mean Aerodynamic Chord, the characteristic chord length of the wing

With the NP located 151 mm from the root chord leading edge and a mean aerodynamic chord (MAC) of 182 mm, the CG should be positioned at 133 mm from the root chord leading edge to maintain the desired 10% static margin.

8.3.5 XFLR5 Analysis

To evaluate the aerodynamic performance and stability of the initial concept, the design was modeled in XFLR5. This section presents the setup and results of the analysis, including trimmed flight conditions, L/D ratio, stability derivatives, dynamic modes, and overall feasibility of the configuration.

XFLR5 model

The detailed dimensions used in the XFLR5 aerodynamic model are available in Appendix A.5.7. Figures 8.3, 8.4, 8.5 and 8.6 illustrates the XFLR5 model from various perspectives.

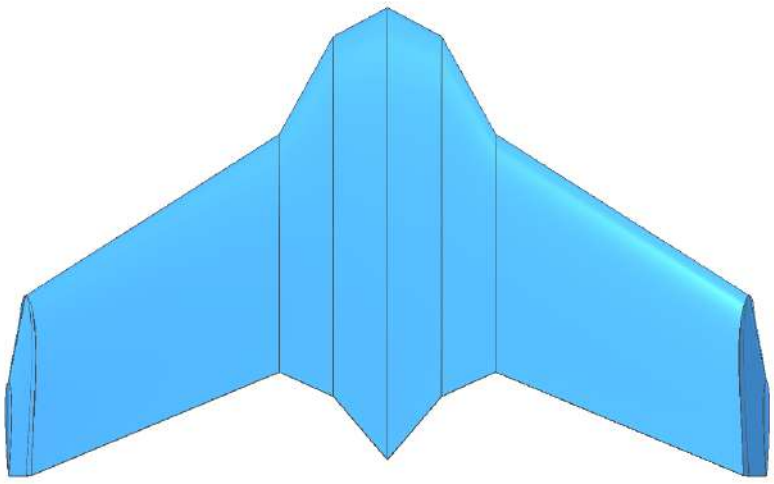

Figure 8.3: Planform in XFLR5.

Figure 8.4: Front view in XFLR5.

Figure 8.5: Side view in XFLR5.

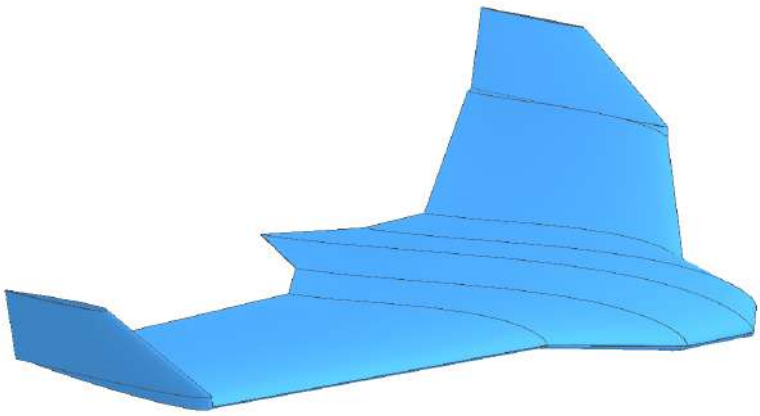

Figure 8.6: Isometric view in XFLR5.

Performance

Stable flight at a zero pitching moment C_m occurs at 21.68 m/s with an angle of attack of 1.75°, indicating the trim condition for steady, level flight (see Figure 8.7).

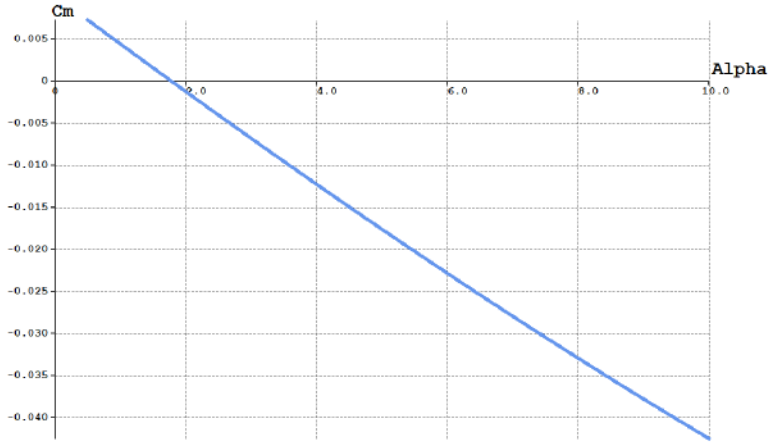

Figure 8.7: C_m vs Alpha.

The maximum C_l/C_d is 14.6 and is achieved at 12.5 m/s, suggesting this as the most aerodynamically efficient cruising speed (see Figure 8.8). AoA that yield optimal C_l/C_d distributions are found in the range of 4° to 5° (see Figure 8.9), reinforcing that the most efficient cruise occurs at moderate angles and lower speeds. The optimal cruising speed is therefore estimated to be around 12.5 m/s (43 km/h).

Stall speed is simulated to be approximately 9 m/s; however, this value should be interpreted with caution. Since XFLR5 is based on potential flow theory and does not model viscous effects or flow separation, it cannot accurately capture the nonlinear behavior of stall. As a result, the predicted stall speed is likely underestimated, and higher-fidelity CFD or experimental data would be needed for a more reliable estimate. Due to time constraints the XFLR5's stall predictions was accepted for design guidance, and flight tests were used for validation.

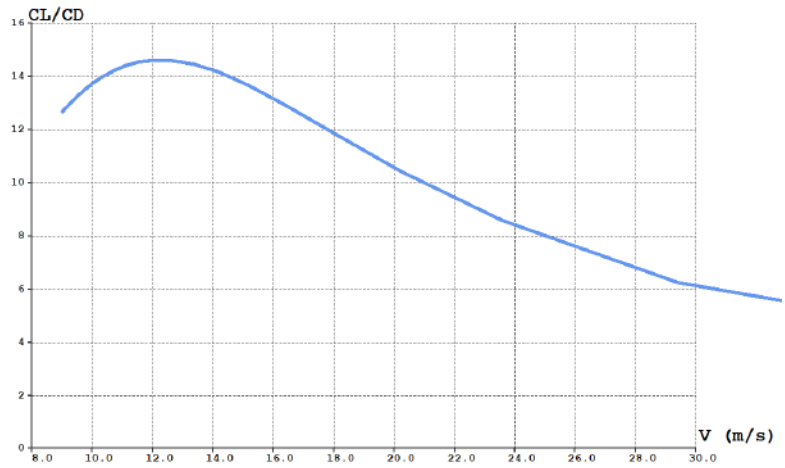

Figure 8.8: Glide polar.

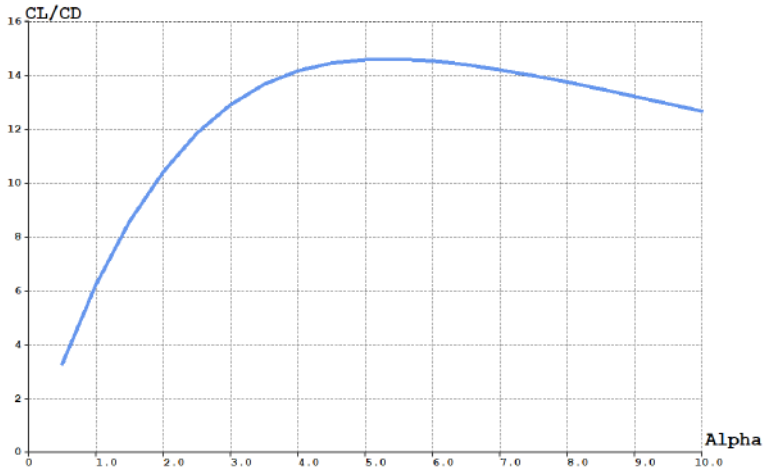

Figure 8.9: C_l/C_d vs Alpha.

Stability Derivatives

As mentioned in the flight mechanics chapter, there are a number of conditions that has to be fulfilled for stable flight. Firstly, these consist of certain stability derivatives that express the aircrafts ability to regain stable flight after a change in trajectory. These derivatives are a direct output from XFLR5 analysis. For this concept, all stability conditions are fulfilled, which can be seen in Table 8.2 below:

Table 8.2: Stability derivatives and conditions for the selected configuration.

Derivative	**Stability Condition**	**Value**
Zero pitch moment C_{m_0}	$C_{m_0} > 0$	Positive
Pitch stiffness C_{m_α}	$C_{m_\alpha} < 0$	-0.31629
Pitch damping C_{m_q}	$C_{m_q} < 0$	-1.10613
Roll damping C_{l_p}	$C_{l_p} < 0$	-0.30126
Roll moment sideslip C_{l_β}	$C_{l_\beta} < 0$	-0.07876
Yaw stability C_{n_β}	$C_{n_\beta} > 0$	0.02627
Yaw damping C_{n_r}	$C_{n_r} < 0$	-0.01895

Dynamic Stability Modes

In addition to the stability derivatives there are also dynamic stability modes, both longitudinal and lateral:

Longitudinal - Short period
According to *MIL-F-8785C* [51], in order to achieve Level 1 flying qualities for a Blended Wing Body (BWB) aircraft, the short period damping ratio, ζ_{sp}, must be greater than or equal to 0.35.

$$\zeta_{sp} = 0.572$$

Result: STABLE (see Figure 8.10)

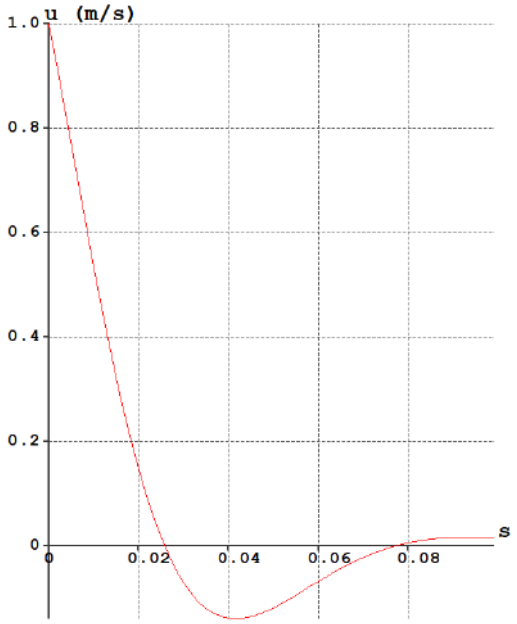

Figure 8.10: Short period mode.

Longitudinal - Phugoid
According to *MIL-F-8785C* [51], in order to achieve Level 1 flying qualities for a Blended Wing Body (BWB) aircraft, the phugoid damping ratio, ζ_{ph}, must be greater than or equal to 0.04.

$$\zeta_{ph} = 0.061$$

Result: STABLE (see Figure 8.11)

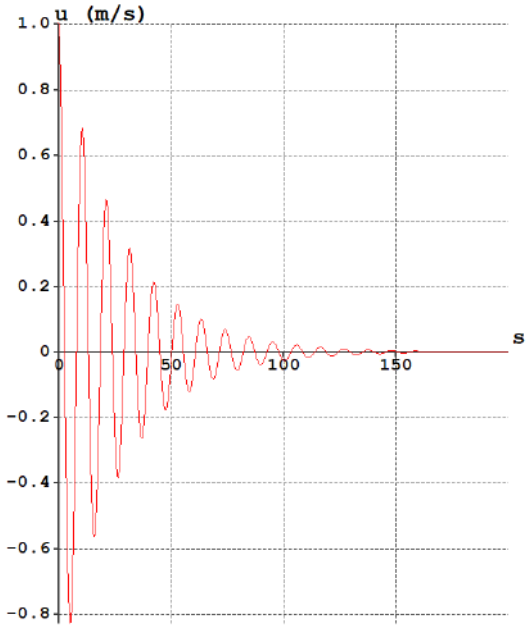

Figure 8.11: Phugoid mode.

Lateral - Roll damping
According to *MIL-F-8785C* [51], to achieve Level 1 flight characteristics, the roll mode time constant must be less than 1.4 seconds. The drone reaches 100% of its final position in less than 0.10 seconds. Result: STABLE (see Figure 8.12)

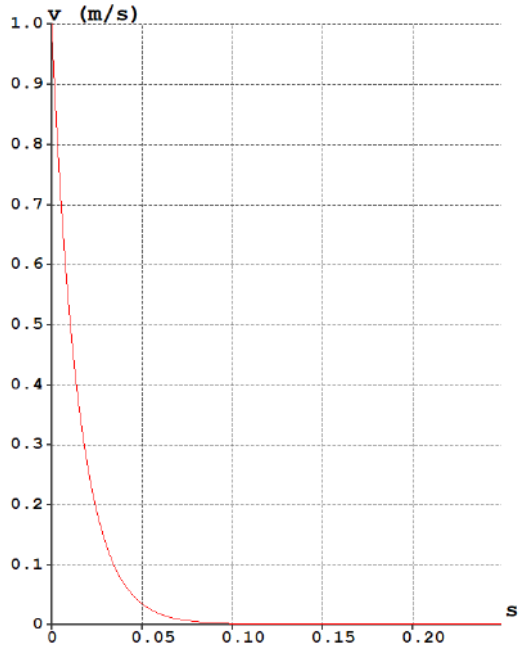

Figure 8.12: Roll damping mode.

Lateral - Dutch roll
According to *MIL-F-8785C* [51], the minimum Dutch roll damping coefficient, ζ_{dr}, should be 0.08.

$$\zeta_{dr} = 0.104$$

Result: STABLE (see Figure 8.13)

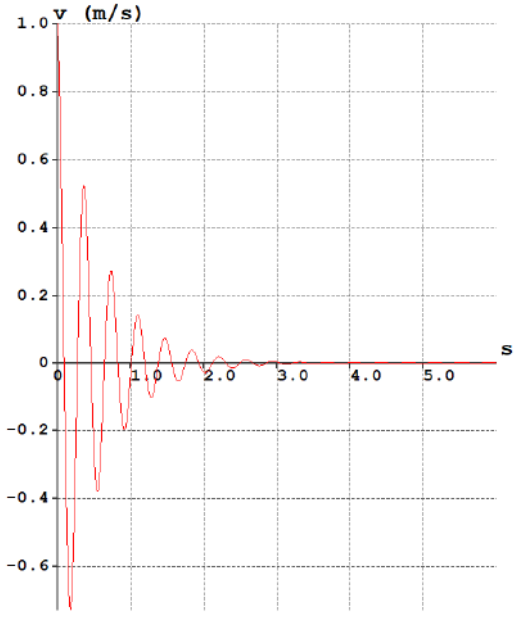

Figure 8.13: Dutch roll mode.

8.3.6 Weight Analysis in OpenVSP

OpenVSP (Open Vehicle Sketch Pad) is an open-source parametric modeling tool developed by NASA. It allows for the creation of accurate 3D geometries based on aerodynamic and structural parameters. In this project, the drone was modeled in OpenVSP to obtain an accurate estimate of its structural weight. A material density

of 40 kg/m³ was assumed, representing the foam intended for the wing construction. The resulting weight of the airframe was approximately 40 grams.

To ensure smooth airflow across the airframe, blending between the wing sections was incorporated into the model (see Figure 8.14). This also serves to prepare the geometry for export as a STEP file to *Fusion 360*, a CAD software developed by Autodesk. Fusion 360 provides tools for design, assembly, and manufacturing, and was used to generate the final 3D print files for the prototype.

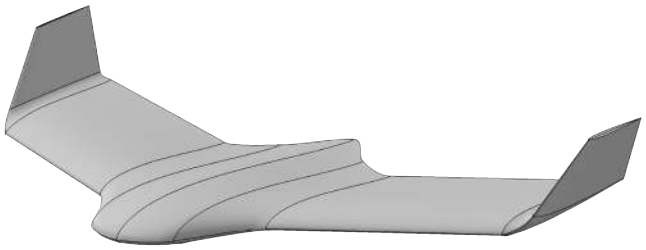

Figure 8.14: OpenVSP model.

9

1st Prototype – Building and Testing

Due to high confidence in the simulation results and the rapid prototyping capabilities enabled by 3D printing, it was decided to make the first prototype fully functional. This also provided an early opportunity to integrate and test the hardware and software systems that would eventually be used in the final prototype.

It is worth noting that this prototype did not use the exact components specified in the BOM, but rather the closest available alternatives from the SSRS parts inventory. The same applies to the airframe: although 3D printing offers a lightweight and accessible manufacturing method, it is not as light as the theoretically optimized, large-scale manufactured foam version. Nonetheless, the prototype is estimated to be sufficiently representative to provide valuable experimental data.

9.1 Airframe

9.1.1 CAD File Preparation

To enable fast and cost-effective prototyping, 3D printing was chosen as the primary manufacturing method. This technology allowed for the rapid production of complex parts with high precision and repeatability, all without the need for extensive tooling or manual labor. The final geometry was exported from OpenVSP and imported into Fusion 360 for detailed preparation. Each airframe component was split strategically to ensure high print quality and eliminate the need for support structures (see Figure 9.1). The components included:

- Middle section front
- Middle section rear
- Canopy front
- Canopy rear
- Wing
- Elevon
- Winglet blend
- Winglet

Elevon Sizing

The elevons were sized based on established flight mechanics guidelines, targeting a total elevon surface area of approximately one-eighth of the total wing area. This proportion is considered a good balance between providing sufficient control authority and minimizing drag. In CAD, the elevons were created by splitting the wing 30 mm forward from the trailing edge, with a consistent chord length from root to tip. This results in an elevon-to-wing area ratio of approximately 12.37%, very close to the intended one-eighth (12.5%) target.

3D Printing Technique

A specialized *vase-mode wing* technique, originally developed by aerospace engineer Tom Stanton [52], was used to print large aerodynamic surfaces. This method enables the printer to continuously print a part's outer perimeter in a spiral motion, avoiding the need to lift the nozzle. Internally, the rib structure is modeled as part of the external surface, tricking the slicer software into printing it as a single continuous shell (see Figure 9.2). This results in a smooth surface finish even when using lightweight PLA, which can otherwise be difficult to print cleanly. Lightweight PLA foams during extrusion, reducing the final part's density by approximately 50%.

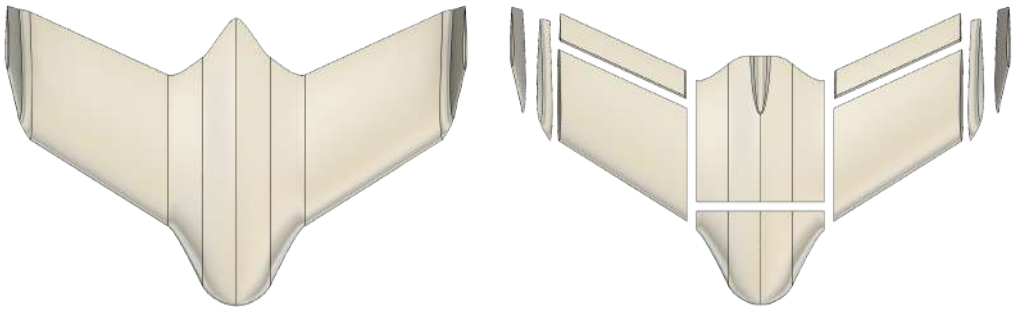

Figure 9.1: Original model (left) & split model (right).

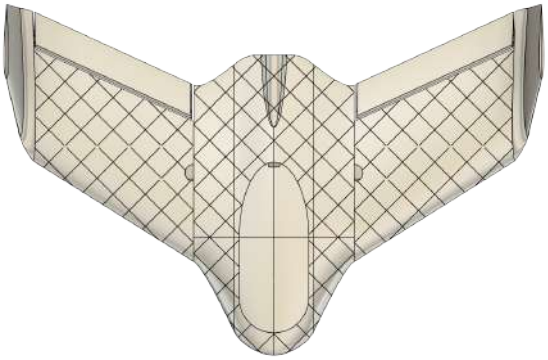

Figure 9.2: 3D print ready model.

This technique also allowed for the integration of structural features such as holes

for carbon fiber reinforcement tubes and servo pockets directly within the wing and middle section. To accommodate electronics, a large cavity was hollowed out of the middle section. Based on earlier estimates, a 5 mm top and bottom wall thickness was sufficient, but to allow for tolerances, the final design used 3 mm.

Only the left side of the aircraft and the middle section were modeled in CAD. The right side was created by mirroring the left-side components in the 3D printing slicer software. The slicer converts CAD models into layer-by-layer G-code instructions for the printer, specifying parameters such as layer height, print speed, infill, and support generation.

9.1.2 3D Printing and Assembly

After all the parts were printed, the airframe went together in a few steps. First, the winglet, winglet blend and main wing were glued into a single assembly. Next, the servos were installed in the wings, and a 3 mm aluminium tube was fed through the elevons to serve as their hinge pin. A carbon tube was then slid through the rear fuselage section, allowing the wings and the elevons to slide on from each side. Once every component was aligned, the entire airframe was bonded using cyanoacrylate, also known as “superglue” (see Figure 9.3). The elevons were then linked to the servos using 1.5 mm piano wire.

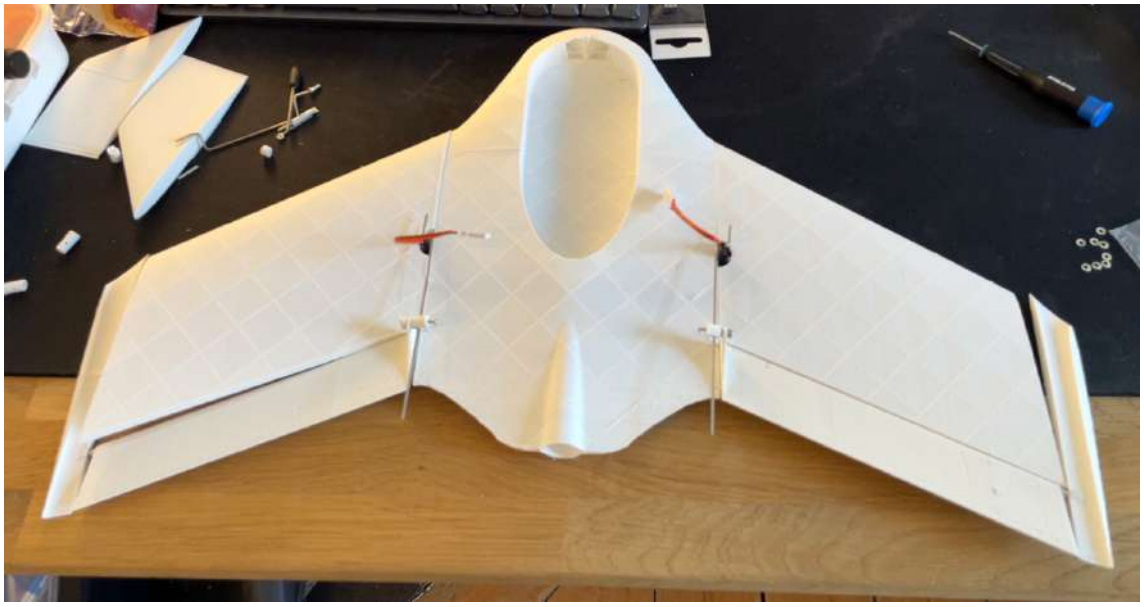

Figure 9.3: Assembly of airframe.

The completed airframe weighed 80 grams. With a measured volume of 975.2 cm^3, the resulting average density was approximately 0.082 g/cm^3. By inserting this mass for the airframe into Fusion 360 and adding simplified models of the remaining hardware, each with realistic mass properties, it was possible to estimate the CG and determine the correct placement of internal components to achieve balance. This layout was then applied during the physical assembly of the prototype (see Figure 9.4 and 9.5).

Figure 9.4: Finished prototype.

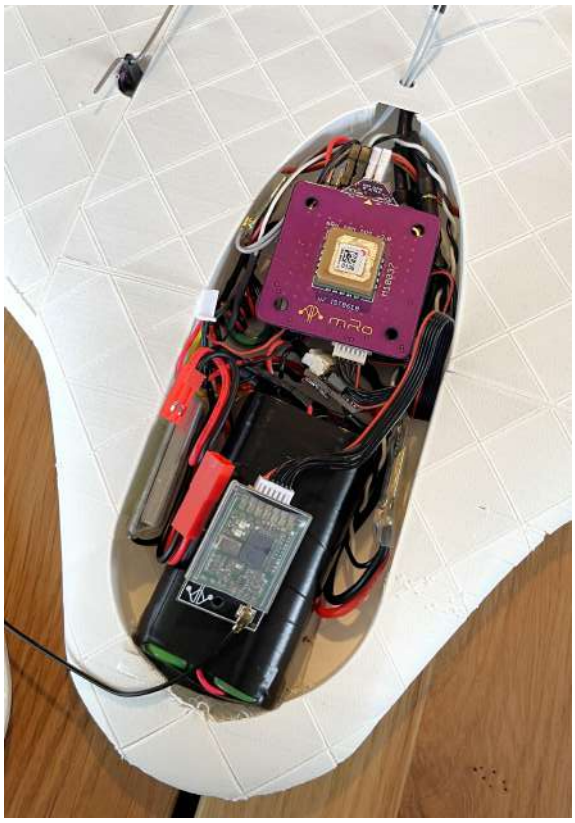

Figure 9.5: Hardware in canopy.

The total weight of the prototype was 302 grams, which was in line with expectations. With the airframe produced in foam, achieving approximately half the density compared to 3D printing, the total mass is estimated to decrease to around 260 grams. Furthermore, when using the optimized BOM with the correct lightweight hardware, the total weight is expected to drop below 250 grams.

It is worth noting that the current testing primarily focuses on the airframe itself. If the prototype demonstrates stable flight characteristics with an additional payload, it can be reasonably assumed that it will perform equally well or better with a lighter configuration. Most importantly, reducing the overall mass will lower the stall speed.

9.2 Electronics & Wiring Scheme

As previously mentioned, the selected components do not all match the optimized BOM, but they closely replicate the final drone's functionality and component weight. The parts selected were:

- **Power Module:** 3DR POWER ZERO
- **Flight Controller:** Pixracer Pro
- **GPS:** SAM GPS + IST8308 Mag
- **RC Receiver:** Futaba R2000SBM
- **SIK Radio receiver:** 3DR SIK TELEMETRY RADIO AIR/GROUND
- **ESC:** SEFM 30A
- **Propeller:** APC 4.1x4.1E
- **Servo:** BMS-101DMG
- **Motor:** EMAX eco 1407
- **Batteries:** 2 x LG INR18650MJ1 3500 mAh
- **BEC (for servo power):** UBEC 5V3A

In order to provide a visual understanding of how each of these components would connect, a wiring diagram was made (see Figure 9.6 and 9.7).

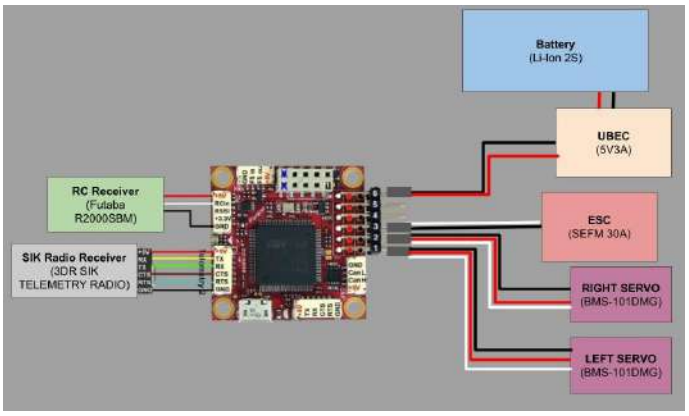

Figure 9.6: Wiring diagram top side.

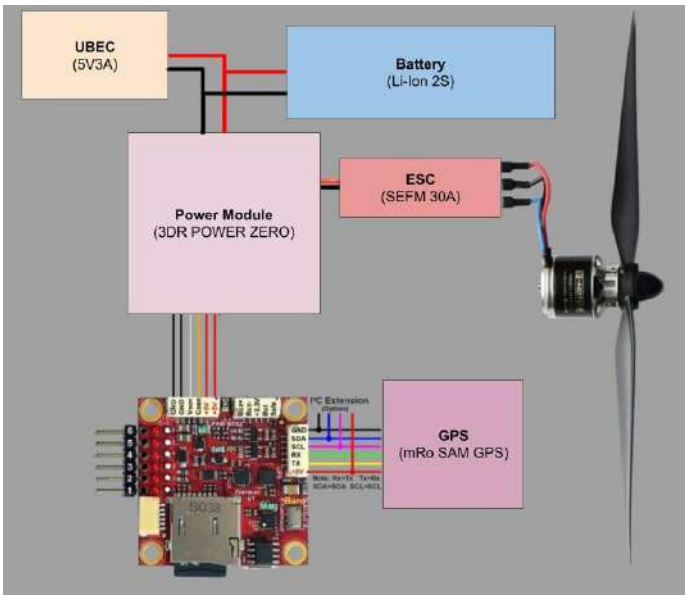

Figure 9.7: Wiring diagram bottom side.

9.2.1 Autopilot Software & Ground Control Station

ArduPilot & QGroundControl

The autopilot system is built upon the ArduPilot open-source firmware, which is loaded directly onto the flight controller. To interact with the flight controller, a ground control station is run on a PC. For this project, QGroundControl serves as the primary ground control station (GCS). QGroundControl provides real-time telemetry including ground speed, altitude, heading, roll, pitch, yaw, battery voltage and current, and GPS status, all displayed on a dashboard and plotted for live monitoring (see Figure 9.8). It is connected to the flight controller on the drone using a 433 mHz USB antenna.

Figure 9.8: QGroundControl - Ground Control Station.

The ArduPilot firmware supports a variety of flight modes to suit different phases of operation. The most commonly used are:

- In **Manual** mode, pilot inputs are passed directly to the control surfaces.
- **Fly-By-Wire A (FBWA)** stabilizes the aircraft by auto-leveling the attitude while still responding to stick commands.
- In **Loiter**, the vehicle circles around a set coordinate, maintaining its position autonomously using GPS and compass feedback.
- The **Return to Launch (RTL)** mode commands the aircraft to fly back to its takeoff point.
- For fine-tuning control parameters, the **Autotune** mode can be engaged; this routine adjusts the PID gains in flight to optimize stability and responsiveness.

Throughout each flight, all sensor data, control inputs, and navigation estimates are continuously recorded to an onboard microSD card in binary log format. After landing, these logs can be downloaded and analyzed.

9.3 Test Flights

9.3.1 Maiden Flight

The maiden flight took place at Trollhättan Airport under light winds, with the tower maintaining radio contact to ensure the airspace remained clear. The ground control setup can be seen in Figure 9.9). After completing all pre-flight calibrations and verifying the CG, the aircraft was switched to FBWA mode. It was then hand-launched into the wind with full throttle. The flight lasted approximately two minutes and the drone flew smoothly and with minimal oscillation, exhibiting good, but perhaps overly robust, control responsiveness, likely a result of the static margin sitting at a relatively high 10%. In FBWA mode, any stick input was effortlessly damped out as the autopilot automatically returned the drone to level flight, making piloting remarkably easy.

This stability, while reassuring, may have masked the subtle handling nuances one would expect with a more neutrally balanced CG. While engaging Manual mode would likely provide a more authentic sense of the aircraft's true control responsiveness, it was deemed too risky given the high chance of failure and the pilot's limited experience.

During the landing attempt on the grass strip, however, the airspeed remained too high and the nose section broke off on impact. While repairing the damage, the battery was inadvertently repositioned forward, shifting the CG. Subsequent launch attempts failed. Because the CG was too far forward, the aircraft could not achieve sufficient angle of attack when thrown.

Figure 9.9: Maiden flight setup.

9.3.2 2nd Test Flight

In preparation for the second test flight, the damaged nose section was repaired and the battery relocated to achieve the correct CG. A new propeller, optimized for cruise efficiency, was installed, and the drone was trimmed with a slight up-elevon "reflex" of a few degrees. This reflex not only improved slow-speed stability but also provided the extra pitch authority needed for a clean hand launch.

Figure 9.10: 2nd test flight - low altitude.

Figure 9.11: 2nd test flight - high altitude.

The aircraft was once again hand-launched into the wind in FBWA mode and remained aloft for thirteen minutes (see Figure 9.10 and 9.11).

The GPS measured an average ground speed of 17 m/s sustained over the 13-minute flight. The drone covered approximately 12.5 km while consuming only 25-30% of its battery capacity. This performance highlights a remarkable level of efficiency and range, comfortably exceeding the mission specifications. Moreover, the measured stall speed of 6.5 m/s lies well below the 8 m/s requirement.

Precise calibration of the power-draw sensor is essential for accurately assessing range and endurance at specific flight speeds. By comparing the battery's true discharge (980 mAh) with the sensor's recorded value (2357 mAh), the onboard voltage/current sensor could be fine-tuned. As a result, all data logged on future flights will reflect true power consumption.

During flight testing, the telemetry link was lost, highlighting the need for a more robust antenna solution. The first prototype used a lightweight flexible antenna to minimize weight, but subsequent prototypes will instead use the standard, more reliable antenna to ensure consistent telemetry performance (see Figure 9.12).

Figure 9.12: Standard antenna (left) and flexible antenna (right).

9.3.3 Estimated Endurance & Range

For the second test flight, the logged mean battery current was 7.07 A (see Figure 9.13) and the mean ground speed 16.93 m/s. Although the absolute current values contain some measurement error, the relative differences at each speed can still be used to predict endurance. Over the 13-minute flight, the battery discharged about 980 mAh of its 3500 mAh capacity, implying a theoretical endurance of:

$$T_0 \;=\; \frac{13\ \text{min}}{980/3500} \;\approx\; 46\ \text{min}$$

Assuming endurance varies inversely (and approximately linearly) with current, we can extend this baseline to estimate the endurance at ground speeds from 8 m/s to 30 m/s (see Figure 9.14). Using these endurance values, a theoretical range can also be calculated (see Figure 9.15):

$$\text{Range (km)} \;=\; \text{Endurance (min)} \;\times\; \frac{60\,\text{s}}{1\,\text{min}} \;\times\; \frac{\text{Speed (m/s)}}{1000}$$

It should be noted, however, that fully depleting the battery pack is not recommended for longevity, so the practical "safe" endurance will be somewhat lower than these theoretical values. Moreover, as the battery discharges, its voltage gradually falls, reducing the available power and further shortening actual flight times compared to the idealized estimates below. Additionally, the speed is measured as ground speed by the GPS, without accounting for wind effects. For a more accurate analysis of range and endurance, an airspeed sensor should be fitted to measure the true airspeed of the aircraft.

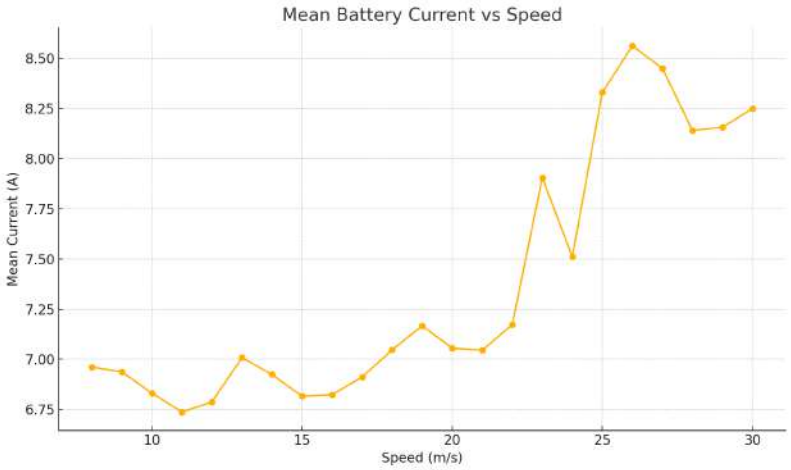

Figure 9.13: Mean battery current vs ground speed.

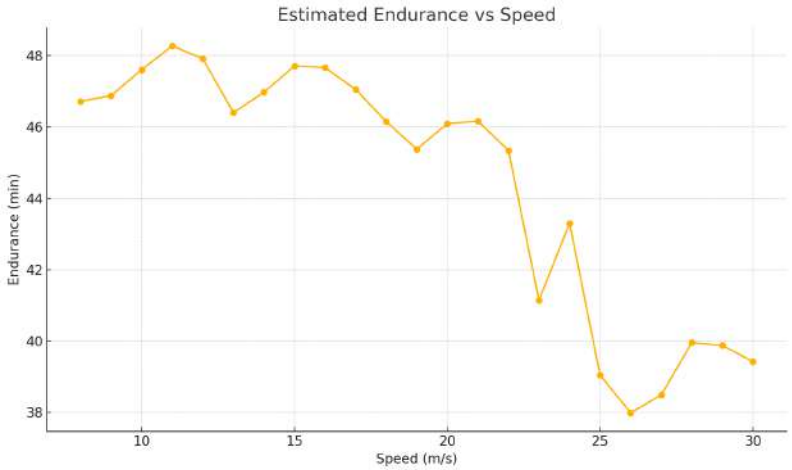

Figure 9.14: Estimated endurance vs ground speed.

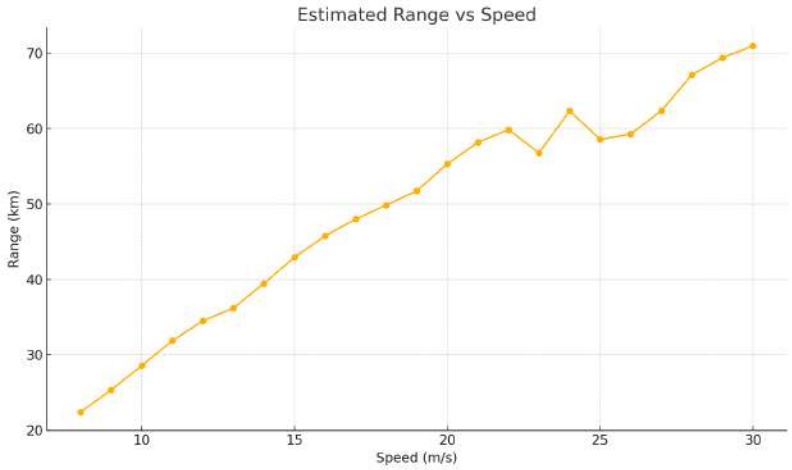

Figure 9.15: Estimated range vs ground speed.

10

Aerodynamic Optimization

10.1 Optimization Problem Definition

Given the tight timeline and broad project scope, the aerodynamic optimization was kept brief. The goal was to maximize the L/D ratio within the 8 to 25 m/s flight envelope. Only AR was varied, since it most strongly affects low-speed performance at low Reynolds numbers. Adjusting AR changes wingspan and wing area, and by extension taper ratio, but these are consequences rather than separate design variables. The mid body shape and airfoil remained unchanged.

10.1.1 Objective

Objective: Maximize L/D ratio within the expected flight envelope of 8-25 m/s.

10.1.2 Design Variables & Constraints

The sole design variable was the AR, defined as:

$$\mathrm{AR} = \frac{\mathrm{Span}^2}{\mathrm{Area}}$$

Both wingspan and wing area therefore impact the AR. In XFLR5, the wing is modeled using six consecutive sections (see Figure 10.1):

1. Wing root
2. Wing body blend 1
3. Wing body blend 2
4. Wing tip
5. Wing tip blend
6. Winglet

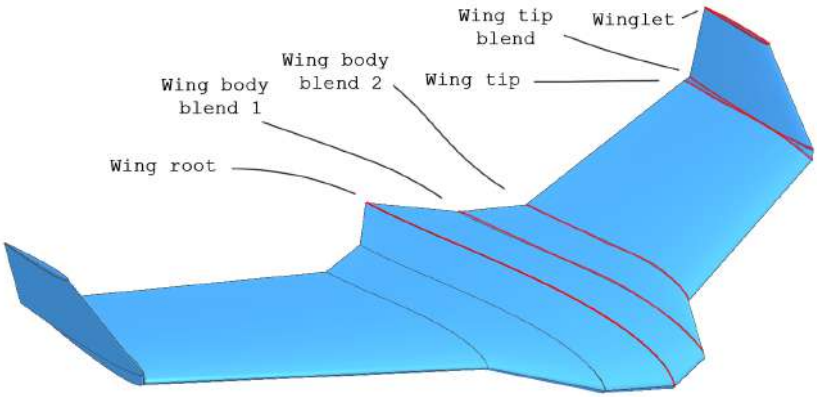

Figure 10.1: Wing sections in XFLR5.

Each of these sections have 6 design variables:

- Y-distance: Spanwise position, measured from the origin along the wing (m).
- Chord: Distance from the leading edge to the trailing edge of the wing cross-section (m).
- Offset: Horizontal (X-axis) displacement from the origin to the wing's leading edge (m).
- Dihedral angle: Angle at which the wing is inclined upward or downward relative to the horizontal plane.
- Twist angle: Variation of wing angle-of-attack along the span, typically to control lift distribution.
- Airfoil: Cross-sectional shape of the wing defining aerodynamic characteristics.

For this optimization, only the Y-position and chord length of section 4 (the wing tip) were treated as free variables. All other geometric parameters were either fixed or directly derived from these two variables (see Figure 10.2).

Free variable
Derived variable
Locked variable

Section	Y (m)	Chord (m)	Offset (m)	Dihedral (deg)	Twist (deg)	Airfoil
1. Wing root	0,000	0,000	0,000	0,0	0,0	PW75
2. Wing blend 1	0,037	0,250	0,020	0,0	0,00	PW75
3. Wing blend 2	0,075	0,165	0,088	0,0	0,00	PW75
4. Wing tip	0,250	0,125	0,200	75,0	-3,00	PW75
5. Wing tip blend	0,255	0,125	0,200	75,0	0,00	NACA 0007 FT
6. Winglet tip	0,300	0,065	0,260	0,0	0,00	NACA 0007 FT

Figure 10.2: Wing sections and their associated variables. The dimensions noted are those of the original concept.

Free Variables

The Y-distance and chord length at the wing tip define both the total wingspan and the overall wing area. Increasing the Y-distance extends the span and wing area, while increasing the chord only enlarges the wing area. These variables are limited to predefined intervals to ensure realistic planform geometries, taking into account both benchmarking results and manufacturing constraints. For instance, a tip chord smaller than 40 mm would result in a structurally fragile wing.

Section 4 Y-distance (m)

- Minimum: 0.200 m → Total span: 0.400 m
- Maximum: 0.350 m → Total span: 0.700 m

Section 4 Chord (m)

- Minimum: 0.040 m
- Maximum: 0.165 m

Derived Variables

To maintain a consistent sweep angle and winglet design regardless of span or area, certain geometric values were derived from the free variables. This ensures alignment with the sweep and winglet guidelines defined in the flight mechanics chapter. The offset for section 4, as well as the Y-position, chord, and offset for sections 5 and 6, were computed as follows:

Section 4

- Offset (m): Sect. 4 Y-distance – 0.050

Section 5
- Y-distance (m): Sect. 4 Y-distance + 0.005
- Chord (m): Equal to Sect. 4 chord
- Offset (m): Equal to Sect. 4 offset

Section 6
- Y-distance (m): Sect. 4 Y-distance + (Sect. 4 Y-distance × 0.2)
- Chord (m): Sect. 4 chord ÷ 2
- Offset (m): Sect. 4 Y-distance × 1.3

Locked Variables
The dimensions of the midsection (sections 1, 2, and 3) were fixed. Additionally, the dihedral angle, twist angle, and airfoil shape remained constant across all sections to reduce complexity and preserve aerodynamic consistency. To compute the AR, the following expressions were used:

$$\mathrm{AR} = \frac{b^2}{A} = \frac{\mathrm{Span}^2}{\mathrm{Midsection, area} + \mathrm{Wing, area}}$$

$$\mathrm{AR} = \frac{(2 \times \text{Sect. 4 Y-distance})^2}{0.037 + \left(\frac{\text{Sect. 3 chord}+\text{Sect. 4 chord}}{2}\right) \times \text{Sect. 4 Y-distance}}$$

10.2 Design Generation - Latin Hypercube Sampling

A Python script was written to generate a set of wing designs by sampling wing tip position and chord length using Latin Hypercube Sampling. For each sample, it calculated derived geometry values and the resulting AR. Valid designs (with AR between 2 and 6) were used to update an XML template describing the aircraft geometry in XFLR5 format. Each design was saved as a separate XML file for further aerodynamic analysis.

Approximately 30 designs were generated, which was deemed a suitable compromise between sufficient coverage of the design space and the time required to perform aerodynamic analysis on all configurations.

10.3 XFLR5 Simulations

10.3.1 CG Calculation

The generated models were imported into XFLR5 for aerodynamic analysis. To ensure consistent and accurate evaluation across all samples, the CG for each aircraft was manually calculated based on its Neutral Point (XNP) and mean aerodynamic chord (MAC) as shown in XFLR5. This adjustment guaranteed a static margin of 10%, promoting stability and enabling fair comparison. Additionally, during the

XFLR5 analysis, any aircraft with a wing area below 7.5 dm^2 or above 10.5 dm^2 was excluded to maintain acceptable weight limits.

10.3.2 Cl/Cd Plot for 8-25 m/s

Each aircraft was analyzed in over a range of angles of attack from $-4°$ to $10°$, at speeds sufficient to generate sustainable lift. For each configuration, aerodynamic performance was evaluated by calculating the L/D ratio. This metric was then plotted as a function of airspeed to allow for direct visual comparison between designs, as can be seen in Figure 10.3:

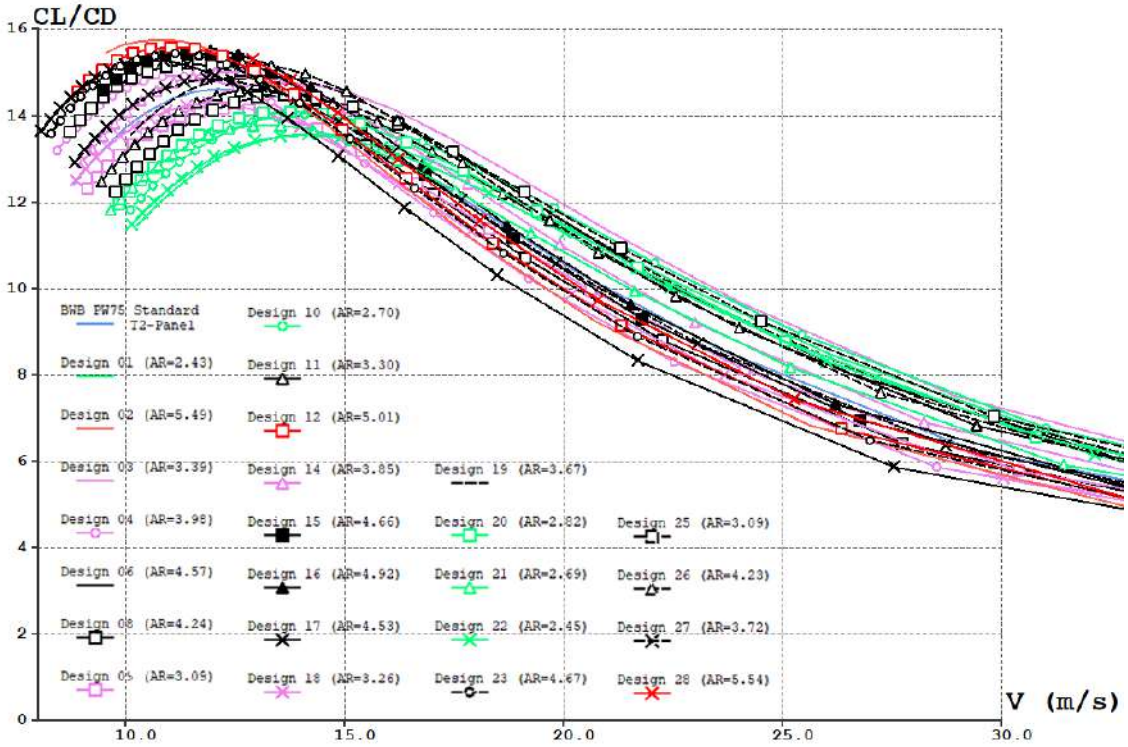

Figure 10.3: Glide polar for all generated designs.

10.3.3 Analysis of Top Performers

As illustrated in the plot above, aircraft with higher ARs demonstrate superior glide performance (higher C_L/C_D values) at lower speeds, as expected. This made them well-suited for slow-speed flight phases such as loitering. Conversely, at higher speeds, designs with lower AR tend to perform better in terms of aerodynamic efficiency. This reveals a fundamental trade-off between slow-speed endurance and high-speed efficiency, requiring a balance depending on the intended mission profile:

Optimized for loitering: The aircraft can be tailored for low-speed operation, maximizing endurance and time on location. However, this comes at the cost of

reduced efficiency during the high-speed transit phase. An example is **Design 02** seen in Figure 10.4, which features an AR of 5.5:

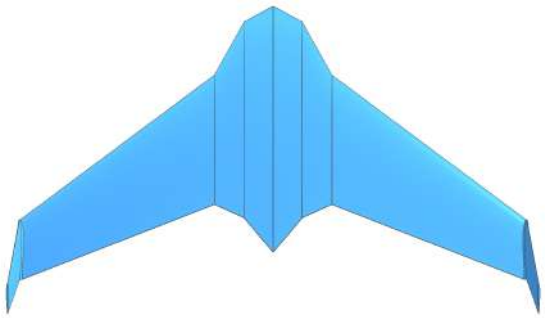

Figure 10.4: Aircraft design 02 optimized for loitering.

Optimized for transit: Alternatively, the aircraft can be optimized for high-speed flight, improving range and efficiency during the initial phase of the mission, but at the expense of loitering performance. This is exemplified by **Design 03** seen in Figure 10.5, with an AR of 3.4:

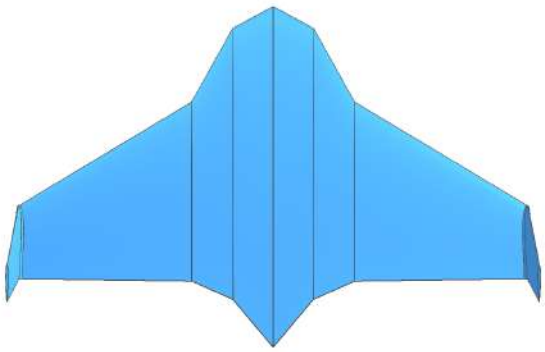

Figure 10.5: Aircraft design 03 optimized for high-speed transit.

Balanced performance: A third approach is to select a moderate AR, achieving a compromise that delivers adequate performance across the entire mission envelope. **Design 14** seen in Figure 10.6, with an AR of 3.9, represents this middle ground:

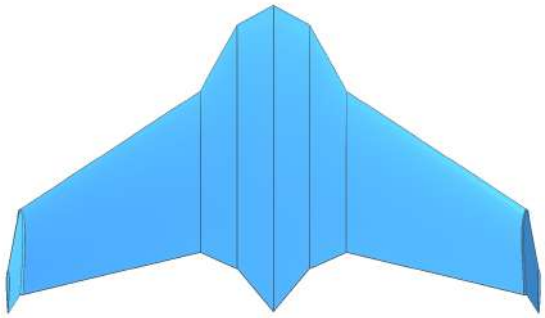

Figure 10.6: Aircraft design 14 with balanced characteristics.

The plot seen in Figure 10.7 below compares the aerodynamic efficiency of the top three performing designs against the standard reference configuration, highlighting their relative strengths across different flight speeds:

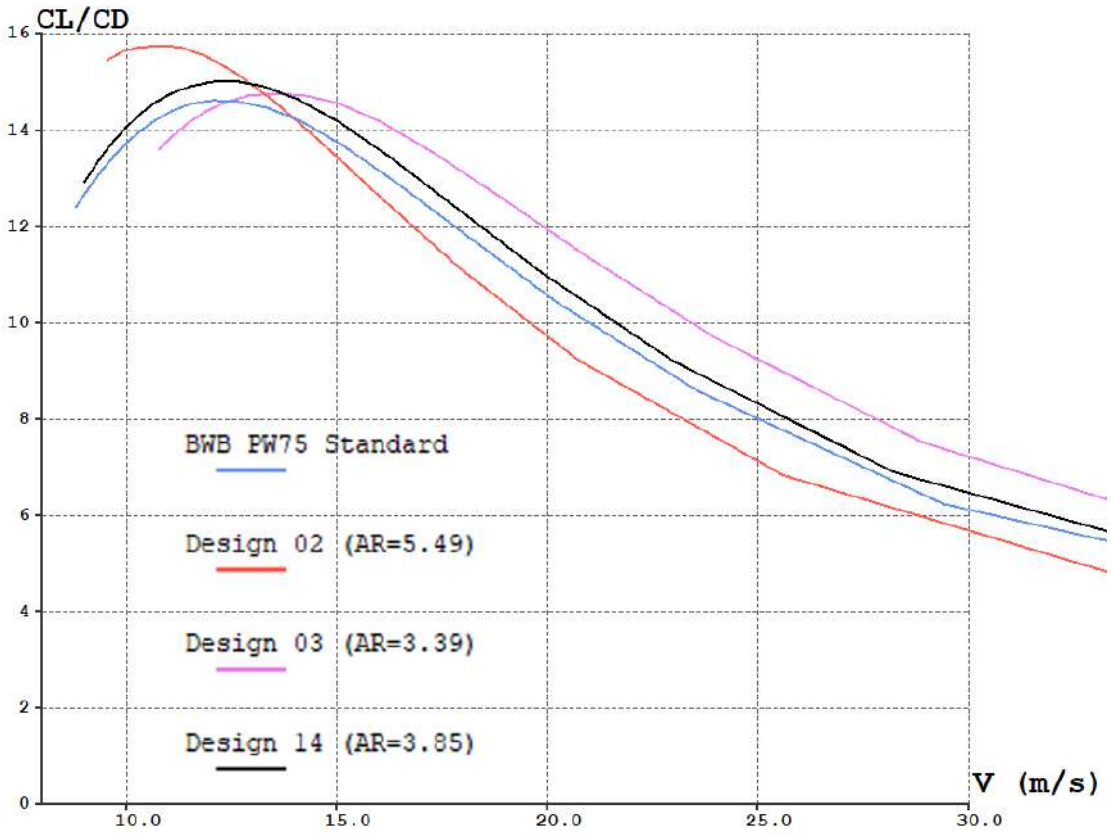

Figure 10.7: Comparison of glide polar across top-performing designs and the reference model.

The detailed dimensions used in the XFLR5 aerodynamic models for the top performers are available in Appendix A.5.7.

10.3.4 Impact of Taper Ratio

Design 14 is very similar to the standard reference design but outperforms it across the entire flight envelope. The primary difference lies in the taper ratio, which is the ratio between the root chord and the wingtip chord. A lower taper ratio means the wingtip is significantly narrower than the root. Among the analyzed configurations, a clear pattern emerges: lower taper ratios tend to yield higher overall aerodynamic efficiency. This is because a lower taper ratio promotes a lift distribution closer to the ideal elliptical shape, reducing induced drag and improving C_L/C_D.

However, this design choice also has drawbacks, as it can cause the wing to stall earlier at the tips, potentially compromising roll control and stability near stall

conditions. Thus, while lower taper ratios improve performance, it must be balanced against handling and stall safety.

10.4 Extended Optimization Analysis

10.4.1 Updated Mid Body & Airfoil

Given the promising results from the test flight in terms of endurance and range, a decision was made to further optimize the aircraft specifically for low-speed flight (loitering). This direction not only aims to enhance endurance but also opens up potential new use-case scenarios, such as forest fire surveillance, where long-duration flight is critical.

In addition to refining the original concept, a secondary design was created featuring a narrower mid-section. This modification allows for an increased overall wingspan while maintaining the same total wing area, effectively raising the AR. To ensure adequate internal space for components, the chord lengths of the central wing sections were kept unchanged.

The same Python script was used for generating wing designs, with updated parameters for sections 1, 2 and 3. The ranges for the free variables were also adjusted to accommodate the new geometry and support a higher AR. Once the designs were generated, they were imported into XFLR5, where the same analysis procedure was followed: filtering by wing area and manually calculating the CG based on the neutral point and mean aerodynamic chord.

The airfoil was also changed to the PW51, which proved to be better suited for high AR configurations. While the PW75 exhibits a slightly higher peak C_L/C_D in 2D analysis, the PW51 consistently performs better in full 3D simulations in XFLR5. This is attributed to its more stable pitching moment which reduce both induced and trim drag. Moreover, PW51 provides more predictable stall behavior and integrates better with the overall wing geometry, resulting in more stable and efficient performance across the entire flight envelope.

10.4.2 XFLR5 Simulations

10.4.3 Cl/Cd Plot for 8-25 m/s

As for the first optimization, the same analysis was done here. A plot of the glide polar as a function of speed for all the generated designs can be seen in Figure 10.8 below.

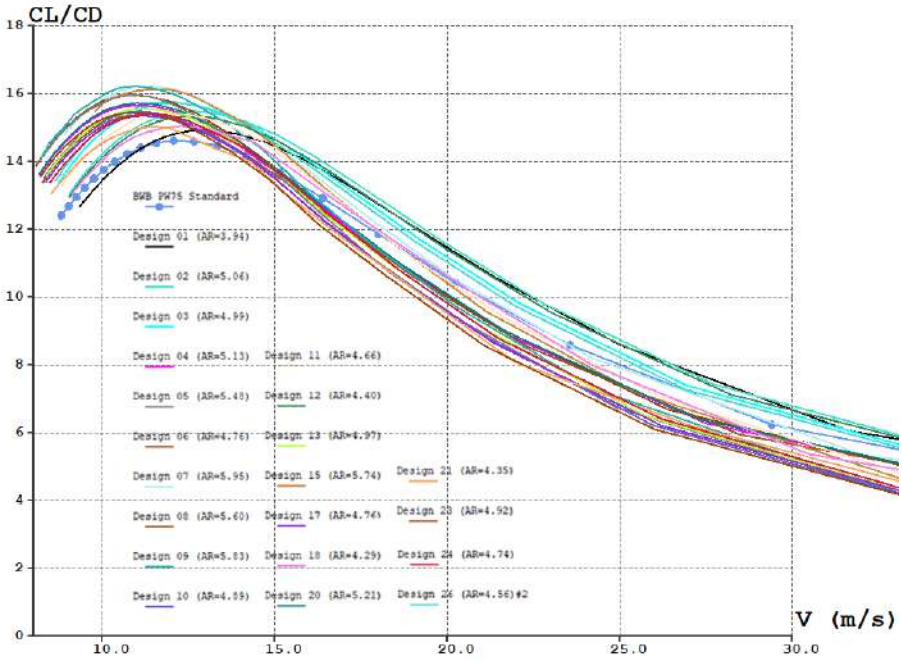

Figure 10.8: Glide polar for all generated designs.

10.4.4 Analysis of Top Performer

For this analysis, two Version 2 (V2) designs stood out as top performers:

Design 26 - Excelling at higher speeds (see Figure 10.9).

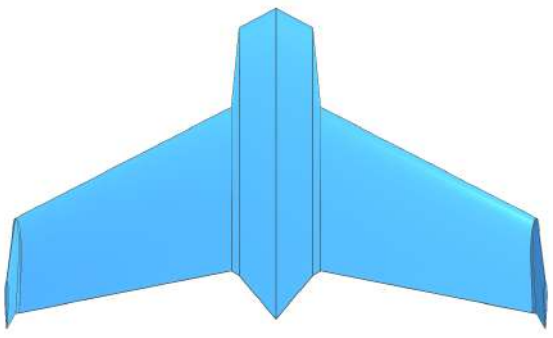

Figure 10.9: 2nd generation optimization - aircraft design 26.

Design 07 - Superior performance during low-speed loitering (see Figure 10.10).

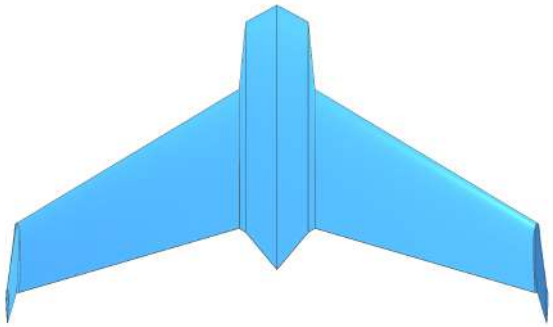

Figure 10.10: 2nd generation optimization - aircraft design 07.

The detailed dimensions used in the XFLR5 aerodynamic models for design 26 and 07 are available in Appendix A.5.7.

The plot in Figure 10.11 below compares these V2 designs with the original concept (BWB PW75 Standard) and the best performers from the previous optimization round (Version 1). Notably, **V1 Design 03** remains the overall top performer, offering the best balance across the entire speed range. However, **V2 Design 26** slightly outperforms it at lower speeds, while still maintaining strong high-speed efficiency.

The standout for loitering missions is clearly **V2 Design 07**, which achieves a C_L/C_D exceeding 16 at around 11 m/s—higher than any other configuration.

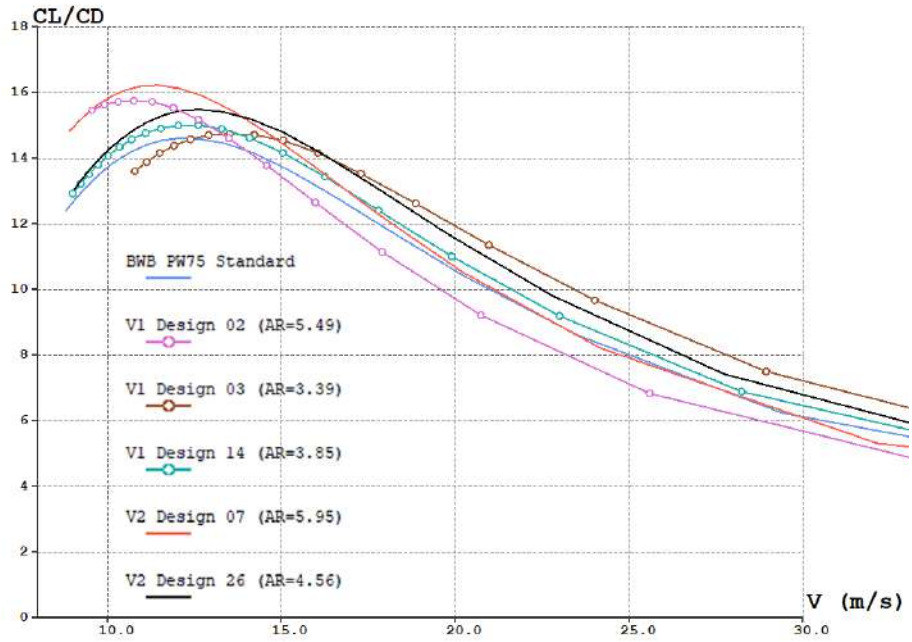

Figure 10.11: Glide polar for top performers of optimization V1 and V2.

11
Final Concept

11.1 Prototype II

11.1.1 Endurance-Focused Redesign

Following the successful test flight of the first prototype, which confirmed that range was not a limiting factor, focus shifted toward maximizing endurance. The goal of the second prototype was therefore to validate the aerodynamic optimization under real-world conditions, with particular emphasis on low-speed performance and extended flight duration. To support this, the design was based on V2 Design 07, which had shown the best loitering capability in simulation while still maintaining strong aerodynamic efficiency across the full flight envelope. With improved endurance, the drone could be adapted for a broader range of missions, such as long-duration surveillance and environmental monitoring.

11.1.2 In-Flight Visualization

The second prototype also featured the integration of an *Insta360 GO3* action camera to provide onboard visual feedback of the drone's flight behavior. This allowed for a deeper understanding of critical flight characteristics such as pitch stability and control surface response, insights that are difficult to fully obtain through ground-based video footage or data logging alone. Although a gimbal-stabilized camera system remains the long-term goal for the drone's operational functionality, it was excluded at this stage due to the added complexity and the need for onboard processing hardware, such as a Raspberry Pi. The Insta360 GO3 offered a lightweight and practical alternative, enabling immersive visual documentation for post-flight analysis.

11.2 Development of Prototype II

11.2.1 Design Changes

Using V2 Design 07 as a base, the root chord was lengthened to 350 mm to make sure the camera would fit in the front. This provided a maximum thickness of 31.15 mm, enough to house the camera with a thickness of about 23 mm. The mid section was also widened a small amount for better aerodynamic blending (see Figure 11.1). To compensate for the 36 g camera mounted near the nose, the wing offset was adjusted

to shift the neutral point forward from 209 mm to 168 mm. This modification made it easier to achieve the desired CG location without adding unnecessary ballast, while maintaining a 10% static margin. The adjustment was crucial for preserving longitudinal stability, especially with the added forward mass.

The winglets were redesigned to improve aerodynamic efficiency. Their span was reduced from 10% to 5% of the wingspan to minimize parasitic drag and structural mass, particularly beneficial at low speeds. The cant angle was increased from 15° to 30°, enhancing yaw stability and deflecting wingtip vortices more effectively.

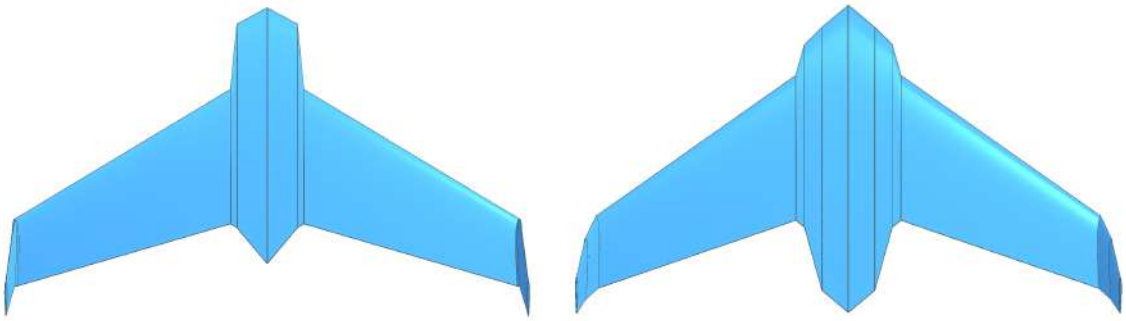

Figure 11.1: Before and after design changes. Detailed dimensions of XFLR5 model for prototype 2 are available in Appendix A.5.7.

11.2.2 CAD File Preparation

As with the first prototype, the model was exported to OpenVSP for blending and weight analysis. Using a foam density of 40 kg/m^3, the airframe model weighed approximately 40,4 grams. The model was then imported into Fusion 360, where it was divided into separate sections and prepared for 3D printing (see Figure 11.2). Components with significant mass were added to the model to determine their optimal placement in order to achieve the correct CG and maintain a 10% static margin.

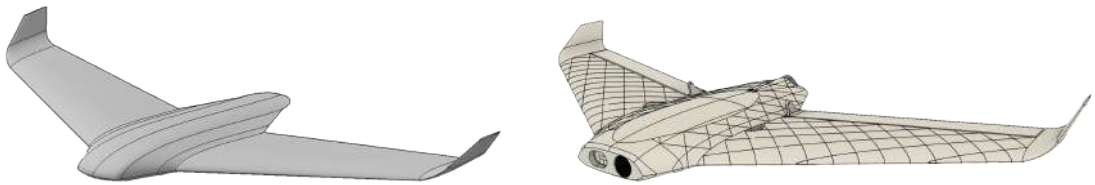

Figure 11.2: OpenVSP and Fusion360 model for 2nd prototype.

11.2.3 3D Printing & Assembly

Each part was then printed and assembled using the same methodology as for the first prototype. Figure 11.3 shows the 3D printed mid section and left wing. However, the nose cone was printed in PETG, a more durable material selected to minimize the need for repairs in the event of a crash. The reinforced nose also served to protect the camera (see Figure 11.4 and 11.5. The wings were covered in red packing tape to reduce drag and enhance the lift coefficient. A smoother surface delays the

transition from laminar to turbulent flow, allowing the wings to generate more lift. In addition to its functional benefits, the red tape significantly improved visibility against the blue sky — a problem encountered with the previous prototype, where the aircraft was difficult to track during flight.

The color choice also supports the project's intended purpose. Red is strongly associated with first responder organizations, giving the drone a safer and more approachable appearance. This visual identity contrasts sharply with the dark grey colors often used for military surveillance drones, which can resemble missiles in both appearance and perception. By adopting a brighter and friendlier color scheme, the drone clearly communicates its peaceful mission and humanitarian focus.

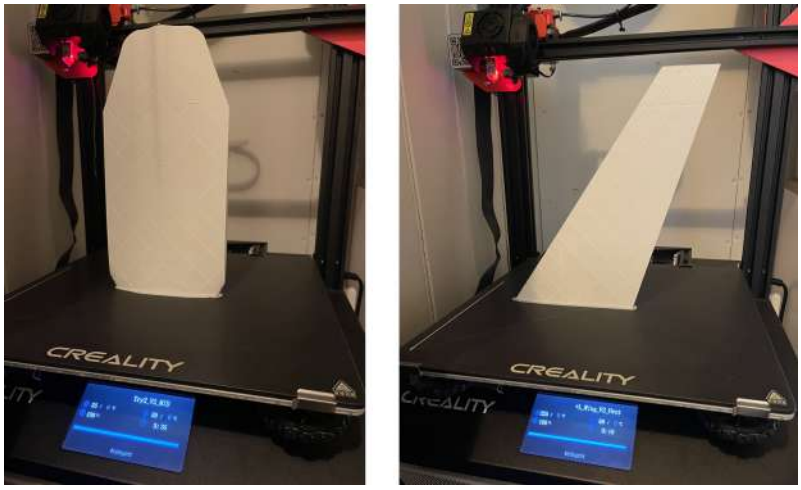

Figure 11.3: 3D printing parts for 2nd prototype.

Figure 11.4: 2nd prototype assembled and flight ready.

Figure 11.5: Close-up of camera installation.

11.3 Flight Testing of Second Prototype

11.3.1 Maiden Flight

The maiden flight of the second prototype was conducted to evaluate stability, control response, and endurance/range performance. The take-off weight was 372 grams, substantially heavier than the first prototype, mainly due to the addition of the camera.

The initial hand-launch method (see Figure 11.6) failed, as the aircraft was unable to pull up quickly enough after being thrown. This was attributed to the higher stall speed and the additional mass. However, a subsequent over-the-head launch method gave the aircraft a higher initial speed and altitude, allowing it to pull up smoothly and achieving stable flight shortly after release.

The larger telemetry antenna fitted on the second prototype performed well, maintaining uninterrupted communication with the ground station (see Figure 11.7) throughout the entire flight. Additionally, the onboard Insta360 camera recorded high-quality video footage (see Figure 11.8), which further confirmed that the flight was stable, with minimal oscillations or disturbances.

Figure 11.6: Hand-launch method.

Figure 11.7: Ground station setup.

Figure 11.8: Aerial view from drone during turn.

During the approach for landing, the aircraft stalled while flying downwind but regained stability just before reaching the ground. This behavior was anticipated, given the significantly increased take-off weight relative to the available wing area. The heavier mass naturally results in a higher stall speed, as shown in the following calculations:

$$V_{\text{stall, 372 g}} = \sqrt{\frac{2 \times 0.372 \times 9.81}{1.225 \times 0.093 \times 1.2}} = \sqrt{53.37} \approx 7.3\,\text{m/s}$$

In comparison, the calculated stall speed for the lighter 250-gram configuration is:

$$V_{\text{stall, 250 g}} = \sqrt{\frac{2 \times 0.250 \times 9.81}{1.225 \times 0.093 \times 1.2}} = \sqrt{35.88} \approx 6.0\,\text{m/s}$$

The results confirm the expected trend: with increased weight, stall speed rises noticeably, requiring careful consideration during landing, especially in windy conditions. Overall, the flight validated the general airframe design, stability, and the plane showed good control authority.

11.3.2 2nd Test Flight

The second test flight took place in stronger winds, estimated at 5–10 m/s, visible by the windsock seen in Figure 11.9. After launch into the wind, the aircraft quickly gained altitude and demonstrated stable flight, with the wings effectively maintaining orientation into the wind. Although the lack of an airspeed sensor limits precise performance assessment, the drone covered 7 km in 7 minutes while using only a small portion of its battery. This suggests it can complete typical missions even under similar wind conditions.

Figure 11.9: 2nd test flight in heavy winds, as indicated by the windsock.

11.3.3 3rd Test Flight & Crash

The third test flight, conducted under similar wind conditions (5–10 m/s), resulted in a stall and subsequent crash. The aftermath of the crash can be seen in Figure 11.10. The failure occurred during a downwind turn, where insufficient throttle input led to a significant reduction in airspeed. The decrease in airspeed caused the aircraft to stall, followed by an unrecoverable spiral descent.

This event underscores a key limitation of the small-scale drone design. While the platform demonstrates acceptable stability and controllability at higher airspeeds, it becomes increasingly vulnerable to aerodynamic disturbances when operating at lower velocities, particularly in turbulent or gusty conditions. In contrast to the more massive 900 g reference drone, the lighter airframe exhibits reduced inertia and greater susceptibility to wind effects. As a result, flight performance cannot be consistently guaranteed in wind speeds exceeding 10 m/s without maintaining adequate airspeed margins.

Figure 11.10: Aftermath of crash during 3rd test flight.

11.3.4 Rebuild & 4th Test Flight

The drone was completely rebuilt following the crash. Fortunately, none of the electrical components were damaged. The rebuild process went swiftly, with the entire airframe being reprinted within 15 hours.

A fourth and final test flight was conducted after the rebuild. This time, the flight was deliberately carried out in calm wind conditions to obtain accurate speed measurements. With minimal wind, the ground speed reported by the onboard GPS closely approximated the true airspeed.

The drone was launched using the over-the-head method and performed as well as in previous flights. During the flight, various throttle settings were tested while circling the airfield to gather data on battery current at different speeds. After

approximately 20 minutes in the air, the drone was no longer able to maintain full throttle, indicating a drop in battery voltage. However, it was still able to cruise steadily at 40–50% throttle. To avoid the risk of losing the drone and the onboard SD card data, the flight was terminated and the drone safely landed.

Data Analysis

The fourth test flight provided valuable performance data for estimating both endurance and range. Over the course of a 21-minute flight, the drone maintained an average ground speed of 20.5 m/s while drawing an average current of 3.20 A. During this period, 1916 mAh of the battery's total 3500 mAh capacity was consumed, giving an estimated endurance of:

$$\text{Endurance} = 21 \text{ min} \times \left(\frac{3500}{1916}\right) \approx 38.7 \text{ min}$$

Throughout the flight, the drone flew with a minimum stable speed of 6.8 m/s, an average speed of 20.5 m/s, and a recorded maximum speed of 33.3 m/s. These values, in combination with the recorded battery current measurements, enable modeling of endurance and range at various cruise speeds (see Table 11.1). The data suggests that the drone achieves its maximum endurance (see Figure 11.11) at a cruising speed of around 10 m/s, where power consumption is minimal. Under these conditions, it can stay airborne for approximately 43 minutes. In contrast, throttle increases caused only a moderate rise in current draw while significantly boosting speed, indicating that maximum range (see Figure 11.12) is theoretically achieved at high velocities. At the recorded top speed of 33.3 m/s, the estimated range exceeds 60 km.

However, the test flight revealed that after about 20 minutes, the battery could no longer supply full throttle, likely due to voltage sag under sustained high current. This suggests that although maximum range occurs near top speed, operating just below full throttle may be more effective in practice, as it reduces the voltage drop.

As a result, the most practical cruising speed is estimated to be the around the specified top speed of 25 m/s, where the drone can maintain steady flight for about 36 minutes and cover an estimated distance of 55 km.

Figure 11.11: Estimated endurance vs ground speed.

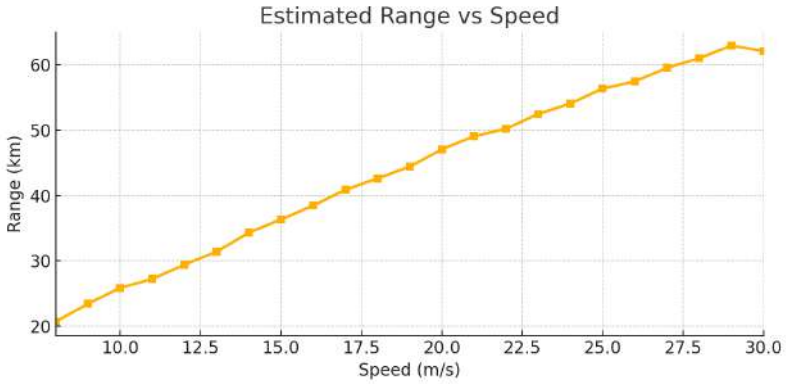

Figure 11.12: Estimated range vs ground speed.

Table 11.1: Average battery current for integer ground speeds and the correlating estimated endurance and range.

Speed (m/s)	Avg. Current (A)	Endurance (min)	Range (km)
8	2.87	43.11	20.69
9	2.85	43.38	23.43
10	2.87	43.12	25.87
11	3.00	41.24	27.22
12	3.03	40.87	29.43
13	3.12	39.62	31.02
14	2.96	41.67	35.00
15	2.95	41.86	37.72
16	2.96	41.71	40.03
17	3.01	41.03	41.96
18	3.13	39.45	42.96
19	3.25	38.00	43.32
20	3.27	37.81	45.37
21	3.19	38.80	49.06
22	3.27	37.79	49.86
23	3.37	36.64	50.67
24	3.17	38.98	56.15
25	3.38	36.63	54.78
26	3.46	35.81	55.91
27	3.52	35.22	57.08
28	3.57	34.73	58.05
29	3.60	34.38	60.05
30	3.64	34.03	61.25

Video analysis

From the ground, the drone appeared to fly with high stability throughout the test. Only minor oscillations were observed in the roll axis, likely caused by occasional

wind gusts. Importantly, the drone consistently corrected these disturbances without intervention.

This visual assessment was confirmed by reviewing the onboard footage (see Figure 11.13), which showed smooth and controlled flight behavior. Both pitch and roll remained highly stable, with only subtle roll oscillations visible during periods of turbulence. The quick self-correction of these deviations suggests that the drone maintains good dynamic stability and damping characteristics.

Figure 11.13: Aerial view from drone during level flight.

11.4 Comparison to First Prototype and the original SSRS Drone

The final prototype was benchmarked (see Table 11.2) against both the original SSRS 900 g fixed-wing drone and the first prototype developed during this thesis. While the SSRS drone remains unmatched in absolute endurance and range due to its larger battery capacity and higher wing surface area (optimal for low-speed loitering), the results show that both prototypes can deliver competitive performance in specific regions of the flight envelope.

Table 11.2: Performance comparison: SSRS vs 250 g prototypes

Metric	SSRS Drone	Prototype I	Prototype II
Max Range (0-25 m/s)	130 km (14 m/s)	62 km (24 m/s)	55 km (25 m/s)
Max Endurance	153 min (14 m/s)	48 min (11 m/s)	43 min (10 m/s)
Takeoff Mass	900 g	302 g	372 g (with camera)

As shown in Figure 11.14, although the SSRS drone has superior range at low cruise speeds (12–16 m/s), this advantage diminishes significantly at higher speeds. At

cruise speeds around 25 m/s, the prototypes demonstrate range values that approach or even match those of the SSRS drone. This is particularly noteworthy considering they operate at roughly one-third of the mass of the SSRS platform. Also, both of the prototypes exceeded the 250 g constraint, which means that performance is expected to further improve when flying with the intended 250 g takeoff weight.

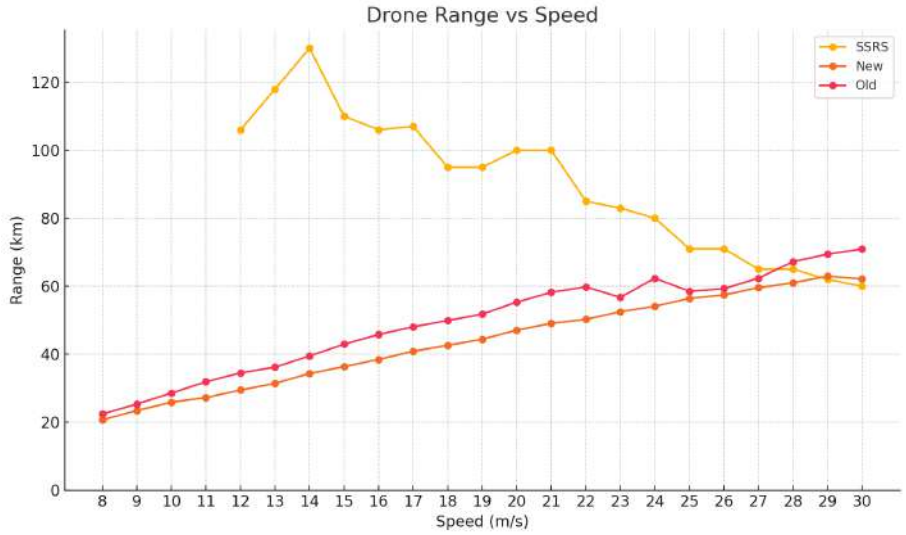

Figure 11.14: Range comparison between SSRS (900 g) and 250 g prototypes (new and old).

Interestingly, both prototypes show a very flat performance curve for both range and endurance (see Figure 11.15), indicating that power consumption scales more linearly with speed than the SSRS drone, implying lower sensitivity to parasitic drag and motor/battery inefficiencies. This suggest a design with greater operational flexibility and speed tolerance, maintaining consistent performance across different flight speeds. This means:

- Less need for precise cruise speed control.
- Better performance under variable conditions (head wind, operator input etc.).
- The designs may be less optimized for a single endurance/range peak, but instead balanced for a broader mission profile.

Comparing the second prototype to the first makes it difficult to isolate the effects of the optimization, primarily because the most influential variable, mass, differed between them. The overall performance of both prototypes appears very similar, with differences likely within the margin of measurement error, despite the second prototype being approximately 20% heavier. This implies that the second prototype must be operating at a higher overall efficiency, as it achieves comparable endurance and range despite carrying more mass. However, any improvements in loitering capability, which was a key objective for the second design, are not clearly evident in the available flight data.

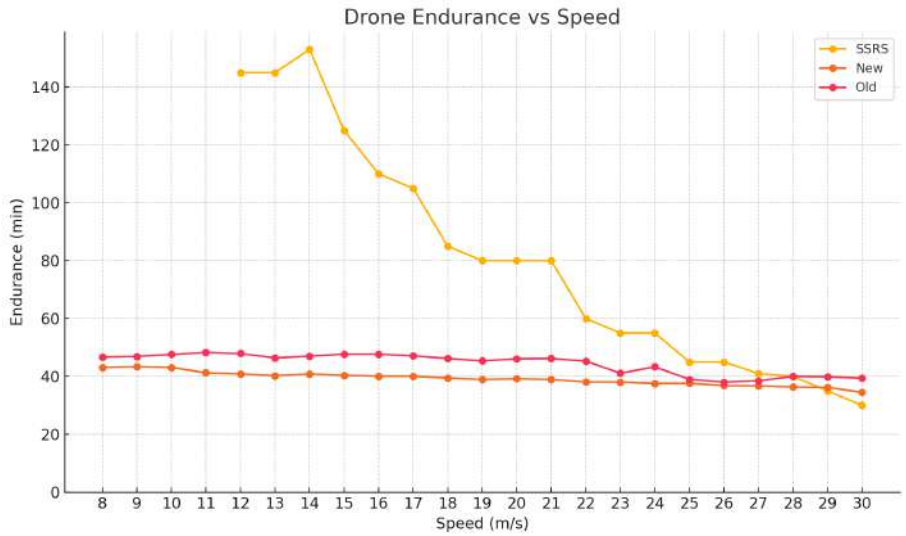

Figure 11.15: Endurance comparison between SSRS (900 g) and 250 g prototypes (new and old).

In summary, while achieving full performance parity with the 900 g SSRS drone is not feasible within the 250 g constraint, both prototypes demonstrate mission-relevant capability, particularly in speed-critical scenarios. Notably, at cruise speeds at around 25 m/s, their range and endurance performance approaches that of the full-size SSRS drone. This makes the prototypes well-suited for rapid-response missions and applications where regulatory advantages of sub-250 g platforms enable low-risk, flexible deployment.

12
Results

The aim of this project was to develop a sub-250 g fixed-wing UAV, suitable for early situational awareness in emergency response scenarios. This chapter presents the results of the thesis.

12.1 Benchmarking

To support the early concept phase, a benchmarking study was conducted on eight tailless fixed-wing UAVs suitable for sub-250 g applications. The analysis focused on aerodynamic layout, stability concepts, and structural configurations. Across the surveyed designs, several consistent trends were identified:

- AR typically ranged from 2.7 to 5.4.
- Sweep angles were moderate (30–35°).
- Pitch stability was achieved using either reflex airfoils or geometric washout.
- Yaw stability was commonly provided by winglets or small vertical fins.
- Most airframes were constructed from lightweight foam and exhibited wing areas between 8 and 9.5 dm^2.

These findings directly influenced the chosen configuration of the final prototype, reinforcing the decision to adopt a blended-wing-body layout.

12.2 Concept development

The development process involved multiple iterations of aerodynamic simulation, design optimization, and physical prototyping.

12.2.1 Prototype I

Testing of the first prototype, conducted with a heavier 302 gram configuration, confirmed the stability and controllability of the airframe. Launch procedures, flight behavior, and telemetry system performance were successfully verified, demonstrating strong preliminary validation of the aerodynamic design.

- Mass: 302 g
- Stall speed: 6.5 m/s
- Max speed: 32 m/s

- Max endurance: 48 minutes (11 m/s)
- Max range (0-25 m/s): 62 km (24 m/s)

12.2.2 Optimization Study

A aerodynamic optimization was performed to maximize Cl/Cd (glide ratio) within the expected flight envelope 8-25 m/s, whilst adhering to the 250 g mass constraint. The design space was limited to a single variable, AR, which in turn impacted wing span and taper ratio. A Python script was written to generate a set of wing designs using Latin Hypercube Sampling. XFLR5 was then used to aerodynamically evaluate each sample, revealing three optimal designs:

- Optimized for loitering: Design 02.
- Optimized for transit: Design 03.
- Balanced performance: Design 14.

An additional optimization study was done, with an updated mid body and airfoil. This resulted in two top performers:

- Optimized for transit: V2 - Design 26.
- Optimized for loitering: V2 - Design 07.

12.2.3 Prototype II

The second prototype was based on the optimized V2 Design 07 layout and included an onboard camera payload.

- Mass: 372 g
- Stall speed: 6.8 m/s
- Max speed: 33.3 m/s
- Max endurance: 43 minutes (11 m/s)
- Max range (0-25 m/s): 55 km (25 m/s)

Despite being approximately 20% heavier than the first prototype, it achieved comparable performance, indicating higher aerodynamic efficiency. However, any improvements in loitering performance, the main optimization goal, were not clearly observed in the flight data.

12.3 Comparison to SSRS Drone

The SSRS 900 g drone served as the benchmark platform. While it remains superior in absolute endurance and range performance, both prototypes demonstrate competitive range performance at higher cruise speeds. Above 25 m/s, both 250 g prototypes achieve range values approaching those of the SSRS drone. This is particularly notable given the large difference in takeoff mass.

These results confirm that the lightweight platform can serve as a fast-deployment alternative when loiter time is less critical than reach and regulatory flexibility.

12.4 Summary of Key Findings

The optimized airframe performs efficiently across a wide speed envelope, maintaining high endurance and range despite testing at weights above the target specification. Power consumption scales nearly linearly with speed, providing operational flexibility for various mission profiles. The second prototype demonstrated comparable performance even at a higher mass, suggesting an increase in overall aerodynamic efficiency. Foam-based construction is expected to reliably achieve sub-250,g compliance, likely maintaining or even improving current performance metrics. Ultimately, all primary design goals, including stall speed, control stability, and endurance, were either met or exceeded during flight testing.

13
Conclusions

13.1 Restatement of Aims

The primary objective of this thesis was to develop a sub-250 g fixed-wing UAV for early situational awareness in critical applications and to conduct an aerodynamic optimization study. Secondarily, the project set out to define key design variables and constraints for that optimization, and to evaluate design trade-offs and regulatory benefits of a lightweight UAV system.

13.2 Summary of Achievements

Feasibility of a sub-250 g UAV
This work has shown that a tailless blended-wing-body airframe, built in low-density EPP foam and sized via an optimized bill of materials, can meet all core performance requirements while remaining under the 250 g mass limit when fully outfitted. Flight tests of two prototypes (one at 302 g and one at 372 g with camera) confirmed that the airframe itself can handle more weight than the 250 g weight target without sacrificing stability or control.

Design Variables & Constraints
A key variable, AR (impacting wing span and taper ratio), and constraints ($\leq$ 250 g maximum take-off mass, stall speed $\leq$ 8 m/s) were formalized in the requirement specification and parameterized for optimization.

Aerodynamic Optimization Study
A systematic Latin-Hypercube sampling of AR (AR 2–6), wing span and root/tip chord in XFLR5 identified two top performers:

- V2–Design 26 optimized for transit
- V2–Design 07 optimized for loitering (L/D = 16 at 11 m/s)

These studies quantified the trade-offs between endurance and range, guiding the selection of the final layout.

Design trade-offs & regulatory advantages
Comparisons against a 900 g SSRS reference drone showed that, around 25 m/s cruise speed, both prototypes achieve similar endurance/range performance while offering simpler regulatory clearance under SORA v2.5 (iGRC 1 regardless of pop-

ulation density). However, the reduced mass also increases the UAV's sensitivity to wind gusts, limiting safe operation in wind speeds exceeding $\approx$ 10 m/s unless additional airspeed margins are maintained.

13.3 Key Quantitative Outcomes

- Prototype II mass: 372 g (airframe ready for 250 g with foam)
- Stall speed: 6.8 m/s (requirement 8 m/s)
- Maximum endurance: 43 min @ 11 m/s
- Maximum range: 55 km @ 25 m/s
- Peak L/D: $\approx$ 16 at 11 m/s

13.4 Operational & Regulatory Impact

By staying under 250 g and capping the top speed at 25 m/s, the drone earns an iGRC 1 rating, removing many flight restrictions and enabling rapid deployment in urban and rural settings. Flight tests confirmed competitive performance, 43 minutes endurance at 10 m/s and a 55 km range at 25 m/s, though winds above 10 m/s exceed its safe envelope. This work proves that a rigorously optimized sub-250 g fixed-wing UAV can rival heavier systems while offering critical regulatory advantages. It establishes a clear blueprint for future lightweight drones in emergency-response roles.

14

Recommendations for Future Work

The prototypes developed during this project successfully fulfilled the parts of the requirement specification that were within the defined project scope. However, to fully meet the complete set of functional and operational requirements, additional work and further development are necessary. Based on the results and insights gained, the following recommendations are proposed. These developments would significantly enhance the drone's robustness, autonomy, and operational readiness, bringing it closer to a fully deployable solution.

14.1 Prototype with Foam Airframe

Construct and flight test a foam-based model incorporating the actual lightweight components defined in the optimized bill of materials (BOM). For both prototypes, using foam with a density of 40 kg/m^3 will reduce the airframe's weight from 80 grams to approximately 40 grams. With this change alone, the total take-off weight is expected to decrease to around 265 grams. For the second prototype, this assumes the onboard Insta360 camera is removed.

Replacing the remaining components with their lightweight counterparts as specified in the BOM is then expected to bring the total weight below the 250 gram target. This setup will enable assessment of the airframe's behavior at a realistic take-off weight, including validation of stall speed, flight stability, and overall performance under operational conditions.

14.2 Onboard Processing & Dedicated PCB

Implement a lightweight onboard computer, such as a Raspberry Pi, similar to the larger SSRS drone platform. This would enable object recognition via the onboard camera and allow for more advanced autonomous flight capabilities. Additionally, a dedicated PCB should be developed to integrate all necessary components into a compact form factor, significantly reducing cabling and improving overall reliability.

14.3 Camera Gimbal

Integrate a camera gimbal improve the usability and quality of aerial footage. A camera gimbal will enhance the drone's effectiveness in situational awareness missions, allowing it to rotate and focus on a point of interest during loiter.

14.4 Weatherproofing

Future iterations should focus on improving the airframe's resistance to weather by implementing waterproofing measures for critical components. This will increase operational reliability in adverse weather environments.

Bibliography

[1] Trafikverket. (2021) *Eyes On Sight - EOS*. Available: https://fudinfo.trafikverket.se/fudinfoexternwebb/pages/PublikationVisa.aspx?PublikationId=7477 [Accessed 05 02 2025]

[2] Kristiansson, M. et al. (2024). *Drones can be used to provide dispatch centres with on-site photos before arrival of EMS in time critical incidents*. *Resuscitation*, 202, 110312. Available: https://www.resuscitationjournal.com/article/S0300-9572(24)00206-5/fulltext [Accessed 05 02 2025]

[3] Transportstyrelsen. (2025). *Drönare – regler och tillstånd*. Available: https://www.transportstyrelsen.se/dronare [Accessed 05 02 2025]

[4] Petterson, E. (2020). *Design of a drone system for maritime search and rescue missions*. Master's thesis, [KTH - Royal Institute of Technology]

[5] Socialstyrelsen. (2023). *Bilaga 10 – Kartläggning av den prehospitala akutsjukvården*. Socialstyrelsen. Available: https://www.socialstyrelsen.se/globalassets/sharepoint-dokument/artikelkatalog/ovrigt/2023-2-8337-bilaga10-enkatsvar.pdf

[6] Socialstyrelsen. (2016). *Hälso- och sjukvårdens förmåga att hantera en allvarlig händelse med många skadade – Erfarenheter och lärdomar av Övning TYKO*. Socialstyrelsen. Available: https://www.socialstyrelsen.se/globalassets/sharepoint-dokument/artikelkatalog/ovrigt/2016-10-7.pdf

[7] Myndigheten för samhällsskydd och beredskap (MSB). (2007). *Automatiska brandlarm – Hur bör räddningstjänsten agera?* Räddningsverket. Available: https://rib.msb.se/filer/pdf/23066.pdf

[8] Tjugofyra7. (2023). *21 min för SOS att larma ut – Stora skillnader i responstid*. Myndigheten för samhällsskydd och beredskap (MSB). Available: https://www.tjugofyra7.se/amnesomraden/raddningstjanst/2023/21-min-for-sos-att-larma-ut---stora-skillnader-i-responstid

[9] Claesson, A. et al. (2016). *Unmanned aerial vehicles (drones) in out-of-hospital cardiac arrest*. Scandinavian Journal of Trauma, Resuscitation and Emergency Medicine, 24, 124. Available: https://doi.org/10.1186/s13049-016-0313-5

[10] JARUS. (2024). *Specific Operations Risk Assessment (SORA) v2.5 – Main Body Release*. Joint Authorities for Rulemaking on Unmanned Systems (JARUS). Available: http://jarus-rpas.org/wp-content/uploads/2024/06/SORA-v2.5-Main-Body-Release-JAR_doc_25.pdf [Accessed 19 02 2025]

[11] ZOHD. (n.d.). *ZOHD Dart 250G*. Available: https://www.zohd.net/zohd-dart-250g [Accessed 19 02 2025]

[12] EMAX. (n.d.). *EMAX Model*. Available: https://emaxmodel.com/ [Accessed 30 04 2025]

[13] 3DR. (n.d.). *Pixracer Pro*. Available: https://store.3dr.com/pixracer-pro/ [Accessed 30 04 2025]

[14] Subash, T., Mayank, M. M., Srikanth, G., Sumantheshwara, G., & Gnanesh, N. D. (2024). *Literature study on tailless UAV*. International Advanced Research Journal in Science, Engineering and Technology, 11(3), 101-109. Available: https://doi.org/10.17148/IARJSET.2024.11316 [Accessed 06 02 2025]

[15] Elijah, T., Jamisola, R. S., Jr., Tjiparuro, Z., & Namoshe, M. (2021). *A review on control and maneuvering of cooperative fixed-wing drones*. International Journal of Dynamics and Control, 9, 1332–1349. Available: https://doi.org/10.1007/s40435-020-00710-2 [Accessed 06 02 2025]

[16] Stewart, M. P., & Martin, S. T. (2020). *Unmanned aerial vehicles: Fundamentals, components, mechanics, and regulations*. Nova Science Publishers. Available: https://www.researchgate.net/publication/351037538 [Accessed 06 02 2025]

[17] Adoni, W. Y. H., Lorenz, S., Fareedh, J. S., Gloaguen, R., & Bussmann, M. (2023). *Investigation of Autonomous Multi-UAV Systems for Target Detection in Distributed Environment: Current Developments and Open Challenges*. Drones, 7(4), 263. Available: https://doi.org/10.3390/drones7040263 [Accessed 06 02 2025]

[18] Baig, A. U. Z., Cheema, T. A., Aslam, Z., Khan, Y. M., Sajid Dar, H., & Khaliq, S. B. (2018). *A new methodology for aerodynamic design and analysis of a small-scale blended wing body*. Journal of Aeronautics & Aerospace Engineering, 7(1), 206. Available: https://doi.org/10.4172/2168-9792.1000206 [Accessed 06 02 2025]

[19] Denieul, Y. (2016). *Preliminary design of control surfaces and laws for unconventional aircraft configurations*. Doctoral dissertation, Institut Supérieur de l'Aéronautique et de l'Espace, Université de Toulouse. Available: https://theses.hal.science/tel-01482103/ [Accessed 07 02 2025]

[20] Kumar, S. H. V., & Shreepal, A. M. (2019). *A study on flight mechanics of tailless aircraft*. Proceedings of the 4th TMAL02 Expert Conference 2019, 43–46.

[21] Cruz, J. R. (2015). *Flight mechanics lecture notes (Version 6)*. NASA Langley Research Center. Available: https://bigidea.nianet.org/wp-content/uploads/2015/10/Flight-Mechanics-Lecture-Notes-V6.pdf [Accessed 06 02 2025]

[22] Hull, D. G. (2007). *Fundamentals of airplane flight mechanics*. Springer-Verlag Berlin Heidelberg. Available: https://aerostarsolutions.wordpress.com/wp-content/uploads/2011/10/fundmentals_of_airplane_flight_mechanics.pdf [Accessed 06 02 2025]

[23] NASA Glenn Research Center. (n.d.). *Forces on an airplane*. NASA. Available: https://www.grc.nasa.gov/www/k-12/VirtualAero/BottleRocket/airplane/forces.html [Accessed 06 02 2025]

[24] NASA Glenn Research Center. (n.d.). *Lift on an airplane*. NASA. Available: https://www.grc.nasa.gov/www/k-12/VirtualAero/BottleRocket/airplane/lift1.html [Accessed 06 02 2025]

[25] NASA Glenn Research Center. (n.d.). *Aircraft motions and the axes of rotation*. NASA. Available: https://www.grc.nasa.gov/www/k-12/VirtualAero/BottleRocket/airplane/rotations.html [Accessed 07 02 2025]

[26] NASA Glenn Research Center. (n.d.). *Aircraft aerodynamics and how airplanes work*. NASA. Available: https://www.grc.nasa.gov/www/k-12/VirtualAero/BottleRocket/airplane/airplane.html [Accessed 07 02 2025]

[27] NASA. (n.d.). *Axes and control surfaces*. NASA. Available: https://www.nasa.gov/wp-content/uploads/2023/06/axes-control-surfaces-k-4.pdf [Accessed 07 02 2025]

[28] NASA Glenn Research Center. (n.d.). *The drag equation*. NASA. Available: https://www.grc.nasa.gov/www/k-12/VirtualAero/BottleRocket/airplane/drageq.html [Accessed 12 02 2025]

[29] NASA Glenn Research Center. (n.d.). *Induced and parasitic drag*. NASA. Available: https://www.grc.nasa.gov/www/k-12/VirtualAero/BottleRocket/airplane/induced.html [Accessed 12 02 2025]

[30] Ur Rahman, N. (2009). *Propulsion and flight controls integration for the blended wing body aircraft (Doctoral dissertation)*. Cranfield University.

[31] Merino Martínez, R. (2014). *Design and analysis of the control and stability of a blended wing body aircraft*. Master's thesis, Royal Institute of Technology). Available: https://www.diva-portal.org/smash/get/diva2:787508/FULLTEXT01.pdf [Accessed 10 02 2025]

[32] Leishman, J. G. (2022). *Introduction to aerospace flight vehicles*. Embry-Riddle Aeronautical University. Available: https://eaglepubs.erau.edu/introductiontoaerospaceflightvehicles/front-matter/4811/ [Accessed 10 02 2025]

[33] Etkin, B., & Reid, L. D. (1996). *Dynamics of flight: Stability and control (3rd ed.)*. Wiley.

[34] Cook, M. V. (2012). *Flight dynamics principles: A linear systems approach to aircraft stability and control* (3rd ed.). Butterworth-Heinemann.

[35] Van Milligan, T. (2000). *Theory and practice of using flying wings*. Apogee Components, Inc. Available: https://www.apogeerockets.com/education/downloads/Newsletter15.pdf [Accessed 10 02 2025]

[36] Boldmethod. (n.d.). *How adverse yaw affects your plane during a roll*. Boldmethod. Available: https://www.boldmethod.com/learn-to-fly/aerodynamics/adverse-yaw-affects-your-plane-during-a-roll-left-and-right/ [Accessed 29 04 2025]

[37] Cornell University. (n.d.). *Dynamic stability*. Available: https://courses.cit.cornell.edu/mae5070/DynamicStability.pdf [Accessed 11 02 2025]

[38] NASA. (n.d.). PRANDTL-D: *A revolutionary approach to aircraft efficiency*. Available: https://ntts-prod.s3.amazonaws.com/t2p/prod/t2media/tops/pdf/DRC-TOPS-36.pdf [Accessed 11 02 2025]

[39] NASA Glenn Research Center. (n.d.). *Lift-to-drag ratio*. Available: https://www.grc.nasa.gov/www/k-12/VirtualAero/BottleRocket/airplane/ldrat.html [Accessed 11 02 2025]

[40] NASA Glenn Research Center. (n.d.). *Range equation*. NASA. Available: https://www.grc.nasa.gov/www/k-12/VirtualAero/BottleRocket/airplane/range.html [Accessed 12 02 2025]

[41] Körpe, D. S., & Kanat, Ö. Ö. (2019). *Aerodynamic optimization of a UAV wing subject to weight, geometric, root bending moment, and performance constraints*. International Journal of Aerospace Engineering, 2019, Article ID 3050824. Available: https://doi.org/10.1155/2019/3050824 [Accessed 12 02 2025]

[42] McCormick, B. W. (1995). *Aerodynamics, aeronautics, and flight mechanics (2nd ed.)*. John Wiley & Sons.

[43] Maughmer, M. D. (2006). *The design of winglets for low-speed aircraft*. Available: https://journals.sfu.ca/ts/index.php/ts/article/view/187 [Accessed 13 02 2025]

[44] Collins, M. (2017, May 1). *What am I: Winglets*. AOPA. Available: https://www.aopa.org/news-and-media/all-news/2017/may/flight-training-magazine/winglets [Accessed 13 02 2025]

[45] Gongzhang, H., & Axtelius, E. (2020). *Aircraft Winglet Design: Increasing the aerodynamic efficiency of a wing*. KTH Royal Institute of Technology, School of Engineering Sciences. Available: https://www.diva-portal.org/smash/get/diva2:1440647/FULLTEXT01.pdf [Accessed 24 04 2025]

[46] Boeing. (n.d.). *737 MAX winglets*. Boeing. Available: https://www.boeing.com/commercial/737max/737-max-winglets [Accessed 24 04 2025]

[47] Dagur, R., Singh, V., Grover, S., Sethi, N., & Arora, B. B. (2018). *Design of flying wing UAV and effect of winglets on its performance*. International Journal of Emerging Technology and Advanced Engineering, 8(3), 414-428. Available: https://www.researchgate.net/publication/325070398 [Accessed 13 02 2025]

[48] Merryisha, S., & Rajendran, P. (2019). *Review of winglets on tip vortex, drag and airfoil geometry*. Journal of Advanced Research in Fluid Mechanics and Thermal Sciences, 63(2), 218–237. Available: https://www.akademiabaru.com/doc/ARFMTSV63_N2_P218_237.pdf [Accessed 13 02 2025]

[49] NASA Glenn Research Center. (n.d.). *Reynolds number*. NASA. Available: https://www.grc.nasa.gov/www/k-12/airplane/reynolds.html [Accessed 13 02 2025]

[50] Drela, M. (2014). *Flight vehicle aerodynamics*. MIT Press.

[51] Department of Defense. (1980, November 5). *MIL-F-8785C: Flying qualities of piloted airplanes*. Available: https://everyspec.com/MIL-SPECS/MIL-SPECS-MIL-F/MIL-F-8785C_5295/ [Accessed 21 04 2025]

[52] Stanton, T. (2022). *Vase mode wing*. Printables. Available: https://www.printables.com/model/261434-vase-mode-wing [Accessed 21 04 2025]

A

Appendix 1

A.1 PERT Diagram

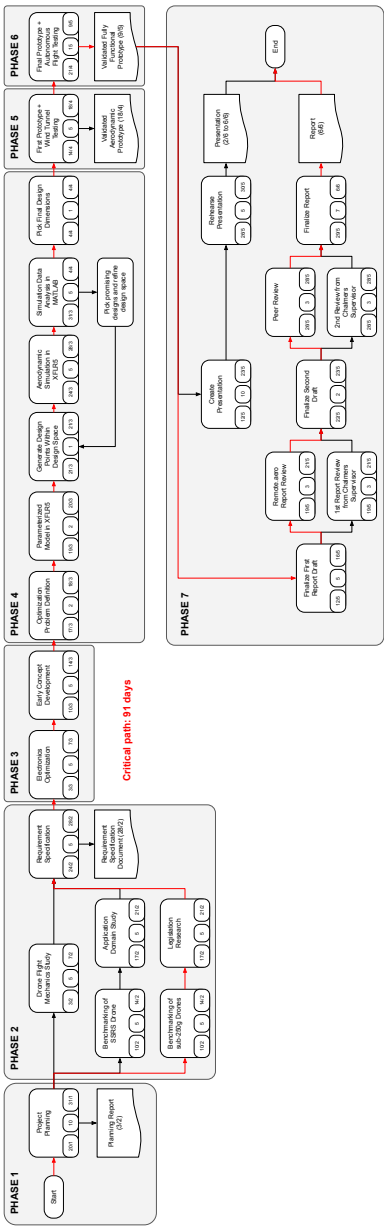

Figure A.1: Project structure and workflow as represented by the PERT diagram. Major milestones and dependencies between tasks are illustrated.

A.2 Gantt Chart

GANTT-CHART

Master Thesis - MPPDE Product Development

Development of a Lightweight Fixed-Wing Drone for Early Situational Awareness in Critical Applications

Alex Andersson 010504-2576

	TASK NAME	START DATE	END DATE	DURATION	% OF TASK COMPLETION
Phase 1	**Project planning**	25-01-20	25-01-31	10	
1.1	*Define project objectives, deliverables and milestones.*	*25-01-20*	*25-01-24*	*5*	5%
1.2	*Set up project time schedule.*	*25-01-20*	*25-01-24*	*5*	0%
1.3	*Secure access to resources, software and facilities.*	*25-01-27*	*25-01-31*	*5*	0%
Gate 1 Deliverables:	☐ Project Planning Report. ☐ GANTT-chart. ☐ PERT-diagram. ☐ List of resources and tools.				0%
Phase 2	**Literature studies and requirement specification**	25-02-03	25-02-28	20	
2.1	*Conduct drone flight mechanics study.*	*25-02-03*	*25-02-07*	*5*	0%
2.2	*Benchmarking of SSRS drone.*	*25-02-10*	*25-02-14*	*5*	0%
2.3	*Benchmarking of sub-250g drones.*	*25-02-10*	*25-02-14*	*5*	0%
2.4	*Conduct application domain research.*	*25-02-17*	*25-02-21*	*5*	0%
2.5	*Conduct legislation research.*	*25-02-17*	*25-02-21*	*5*	0%
2.6	*Create a requirement specification.*	*25-02-24*	*25-02-28*	*5*	0%
Gate 2 Deliverables:	☐ Requirement Specification Document. ☐ "Carry-over" design elements.				0%
Phase 3	**Initial conceptual design**	25-03-03	25-03-14	10	
3.1	*Electronics Optimization*	*25-03-03*	*25-03-07*	*5*	0%
3.2	*Early Concept Development*	*25-03-10*	*25-03-14*	*5*	0%
Gate 3 Deliverables:	☐ Optimized Bill of Materials (BOM). ☐ Early aerodynamic concept. ☐ Aerodynamic analysis of early concept.				0%
Phase 4	**"Proof-of-concept" prototype and flight testing**	25-03-17	25-03-31	11	
4.1	*Create high fidelity CAD model with onboard features/electronics.*	*25-03-17*	*25-03-21*	*5*	0%
4.2	*Build prototype with autonomous flight capability (basically all functionality but no camera - this prototype is for testing the flight characteristics).*	*25-03-24*	*25-03-28*	*5*	0%
4.3	*Conduct manual/autonomous flight test.*	*25-03-29*	*25-03-31*	*3*	0%
4.4	*Troubleshoot and make adjustments based on flight results*	*25-03-29*	*25-03-31*	*3*	0%
Gate 6 Deliverables:	☐ Advanced CAD model. ☐ Fully functional sub-250g UAV prototype. ☐ Flight test results.				0%
Phase 5	**Aerodynamic optimization and detailed design**	25-04-01	25-04-18	15	
5.1	*Evaluate test results from flight testing. FLIGHT LOG ANALYZER in MATLAB.*	*25-04-01*	*25-04-01*	*1*	0%
5.2	*Define the optimization problem.*	*25-04-02*	*25-04-03*	*2*	0%
5.3	*Create a parameterized model in XFLR5.*	*25-04-03*	*25-04-04*	*2*	0%
5.4	*Generate design points within the design space.*	*25-04-07*	*25-04-08*	*2*	0%
5.5	*Conduct aerodynamic simulation.*	*25-04-09*	*25-04-11*	*3*	0%
5.6	*Analyze simulation result data and iterate optimization.*	*25-04-14*	*25-04-16*	*3*	0%
5.7	*Pick final design dimensions.*	*25-04-16*	*25-04-18*	*3*	0%
Gate 4 Deliverables:	☐ Optimized aerodynamic concept. ☐ Results of multi-objective aerodynamic optimization study.				0%
Phase 6	**Final prototype and flight testing**	25-04-21	25-05-04	14	
6.1	*Create high fidelity CAD model with all onboard features/electronics. Based on XFLR5 model with optimal design dimensions - convert to OPENVSP for wing-blending and fusion for 3D print.*	*25-04-21*	*25-04-23*	*3*	0%
6.3	*Build final prototype, aerodynamically optimized and with all functionality (autopilot, gps, camera gimbal etc.)*	*25-04-23*	*25-04-30*	*8*	0%
6.4	*Conduct manual/autonomous flight tests.*	*25-05-01*	*25-05-04*	*4*	0%
6.5	*Condyct wind tunnel test to validate simulated aerodynamic performance.*	*25-05-01*	*25-05-04*	*4*	0%
Phase 7	**Documentation and presentation**	25-05-05	25-06-06	27	
7.1	*Finalize first report draft.*	*25-05-05*	*25-05-16*	*12*	0%
7.2	*Finalize second report draft.*	*25-05-22*	*25-05-23*	*2*	0%
7.3	*Create presentation and prepare for defense.*	*25-05-12*	*25-05-23*	*10*	0%
7.4	*Finalize report.*	*25-05-26*	*25-06-06*	*10*	0%
7.5	*Present the thesis.*	*25-06-02*	*25-06-06*	*5*	0%
7.6	*Conduct opposition on another thesis.*	*25-06-02*	*25-06-06*	*5*	0%
Gate 7 Deliverables	☐ Final report. ☐ Presentation and defense material.				0%

Figure A.2: Gantt chart illustrating the project timeline, major phases, and task scheduling.

A.3 Bill of Materials

Part	Description	Notes	250g Version	Amount	Weight/unit (g)	Weight (g)
Body						57,6
EPP Body	The drone's main structure	TBD	TBD	1	50	50
Main spar	Load-bearing structure within the wing	Same as goblin	3mm CF Rod	400mm	4,2	4,2
Elevon spar	Reinforcing structure within the control surfaces (elevons)	Keep	Kolrek-03-0,4 x 160 mm	2	0,2	0,4
Elevon linkage	Mechanical connections between servos and elevons	Custom	Steel rod + 3d printed tabs	2	1,5	3
Carrier board				1	43,2	43,2
- CM4	Embedded computing unit for onboard processing of video feed, telemetry and flight commands.	Keep for funct.	Raspberry Pi CM4	1	12	
- Modem	Provides LTE connectivity for remote communication and telemetry.	Keep for funct.	Telit LE910C4-EU LTE CAT-4 mPCIe	1	10	
- Flight Controller/Autopilot	Flight stability and control, executing programmed waypoints.	Keep for funct.	3DR CONTROL ZERO H7 OEM	1	3,5	
- BMS	Regulates and protects the battery cells during charging	Remove				
- Airspeed Sensor	Measures dynamic pressure to estimate airspeed	Keep for funct.	mRo Next-Gen MS5525	1	1,7	
- Power Module	Distributes and regulates power to electronics	Keep for funct.	AUAV Power Module (ACSP5)	1	2	
- PCB + connectors	Central hub for electrical connections	Shred weight	Est. weight (no bms connector etc)	1	14	
Electronics						115,6
Elevon servos	Actuators that move the elevons	Same as Goblin	EMax ES9051	2	4,1	8,2
Batteries	Power source for propulsion and avionics	Fredrik rec.	Ampirus SA10 2S Li-Ion 4000mAh	2	48	96
GPS	Positioning data	Keep for funct.	Keep	1	9	9
LTE Antenna	Long-range data transmission and remote monitoring	Keep for funct.	Keep	1	2,4	2,4
Propulsion						24,35
Motor	Converts electrical energy into thrust	Same as FLIK	Emax RS1108 5200kv	1	8,2	8,2
ESC	Regulates motor speed based on flight controller inputs	Fredrik rec.	Chaos BLHeli_S Dshot ESC 20A 2-6S	1	4,9	4,9
Propeller	Converts motor torque into thrust	Same as FLIK	Avan Mini 3"	1	1,25	1,25
Misc. cables	Connects propulsion components to power and control systems	Same estimate.	Not spec. Weight est.	1	10	10
Payload						9,9
RGB Camera	Regular camera	TBD		1	1,7	1,7
FLIR Camera	Thermal imaging	Remove				
Camera Gimbal Servo	Adjusts camera orientation for stable imaging	Only 2 axis. Investigate.	EMax ES9051	2	4,1	8,2

Figure A.3: Bill of Materials (BOM) summarizing the components selected for the final prototype configuration.

A.4 Benchmarking Table

Figure A.4: Full benchmarking table including airframe parameters and material choices.

A.5 XFLR5 Model Dimensions

A.5.1 1st Prototype

	y ()	chord ()	offset ()	dihedral(°)	twist(°)	foil	X-panels	X-dist	Y-panels	Y-dist
1	0,000	0,314	0,000	0,0	0,00	FW75	13	Cosine	5	-Sine
2	0,037	0,250	0,020	0,0	0,00	FW75	13	Cosine	5	-Sine
3	0,075	0,165	0,088	0,0	0,00	FW75	13	Cosine	9	-Sine
4	0,250	0,125	0,200	75,0	-3,00	FW75	13	Cosine	4	Uniform
5	0,255	0,125	0,200	75,0	0,00	NACA 0007 Free Transitions	13	Cosine	2	Uniform
6	0,300	0,065	0,260		0,00	NACA 0007 Free Transitions				

Figure A.5: XFLR5 dimensions of 1st prototype.

A.5.2 V1 - Design 02

	y ()	chord ()	offset ()	dihedral(°)	twist(°)	foil	X-panels	X-dist	Y-panels	Y-dist
1	0,000	0,314	0,000	0,0	0,00	FW75	13	Cosine	5	Uniform
2	0,037	0,250	0,020	0,0	0,00	FW75	13	Cosine	5	Uniform
3	0,075	0,165	0,088	0,0	0,00	FW75	13	Cosine	9	Uniform
4	0,323	0,076	0,273	75,0	-3,00	FW75	13	Cosine	4	Uniform
5	0,328	0,076	0,273	75,0	0,00	NACA 0007 Free Transitions	13	Cosine	2	Uniform
6	0,387	0,038	0,354		0,00	NACA 0007 Free Transitions				

Figure A.6: XFLR5 dimensions of V1 optimization, design 02.

A.5.3 V1 - Design 03

	y ()	chord ()	offset ()	dihedral(°)	twist(°)	foil	X-panels	X-dist	Y-panels	Y-dist
1	0,000	0,314	0,000	0,0	0,00	FW75	13	Cosine	5	Uniform
2	0,037	0,250	0,020	0,0	0,00	FW75	13	Cosine	5	Uniform
3	0,075	0,165	0,088	0,0	0,00	FW75	13	Cosine	9	Uniform
4	0,233	0,068	0,183	75,0	-3,00	FW75	13	Cosine	4	Uniform
5	0,238	0,068	0,183	75,0	0,00	NACA 0007 Free Transitions	13	Cosine	2	Uniform
6	0,280	0,034	0,238		0,00	NACA 0007 Free Transitions				

Figure A.7: XFLR5 dimensions of V1 optimization, design 03.

A.5.4 V1 - Design 14

	y ()	chord ()	offset ()	dihedral(°)	twist(°)	foil	X-panels	X-dist	Y-panels	Y-dist
1	0,000	0,314	0,000	0,0	0,00	FW75	13	Cosine	5	Uniform
2	0,037	0,250	0,020	0,0	0,00	FW75	13	Cosine	5	Uniform
3	0,075	0,165	0,088	0,0	0,00	FW75	13	Cosine	9	Uniform
4	0,259	0,088	0,209	75,0	-3,00	FW75	13	Cosine	4	Uniform
5	0,264	0,088	0,209	75,0	0,00	NACA 0007 Free Transitions	13	Cosine	2	Uniform
6	0,311	0,044	0,272		0,00	NACA 0007 Free Transitions				

Figure A.8: XFLR5 dimensions of V1 optimization, design 14.

A.5.5 V2 - Design 07

	y ()	chord ()	offset ()	dihedral(°)	twist(°)	foil	X-panels	X-dist	Y-panels	Y-dist
1	0,000	0,314	0,000	0,0	0,00	PW51	13	Cosine	5	Uniform
2	0,037	0,250	0,020	0,0	0,00	PW51	13	Cosine	5	Uniform
3	0,045	0,165	0,100	0,0	0,00	PW51	13	Cosine	9	Uniform
4	0,309	0,082	0,259	75,0	-3,00	PW51	13	Cosine	4	Uniform
5	0,314	0,082	0,259	75,0	0,00	NACA 0007 Free Transitions	13	Cosine	2	Uniform
6	0,355	0,041	0,337		0,00	NACA 0007 Free Transitions				

Figure A.9: XFLR5 dimensions of V2 optimization, design 07.

A.5.6 V2 - Design 26

	y ()	chord ()	offset ()	dihedral(°)	twist(°)	foil	X-panels	X-dist	Y-panels	Y-dist
1	0,000	0,314	0,000	0,0	0,00	PW51	13	Cosine	5	Uniform
2	0,037	0,250	0,020	0,0	0,00	PW51	13	Cosine	5	Uniform
3	0,045	0,165	0,100	0,0	0,00	PW51	13	Cosine	9	Uniform
4	0,262	0,096	0,212	75,0	-3,50	PW51	13	Cosine	4	Uniform
5	0,267	0,096	0,212	75,0	0,00	NACA 0007 Free Transitions	13	Cosine	2	Uniform
6	0,301	0,048	0,276		0,00	NACA 0007 Free Transitions				

Figure A.10: XFLR5 dimensions of V2 optimization, design 26.

A.5.7 2nd Prototype

	y ()	chord ()	offset ()	dihedral(°)	twist(°)	foil	X-panels	X-dist	Y-panels	Y-dist
1	0,000	0,350	0,000	0,0	0,00	PW51	13	Cosine	5	Uniform
2	0,030	0,300	0,025	0,0	0,00	PW51	13	Cosine	3	Uniform
3	0,050	0,208	0,045	0,0	0,00	PW51	13	Cosine	2	Uniform
4	0,060	0,165	0,080	0,0	0,00	PW51	13	Cosine	9	Uniform
5	0,287	0,082	0,240	60,0	-3,00	PW51	13	Cosine	4	Uniform
6	0,312	0,070	0,265	65,0	0,00	NACA 0007 Free Transitions	13	Cosine	2	Uniform
7	0,337	0,041	0,310		0,00	NACA 0007 Free Transitions				

Figure A.11: XFLR5 dimensions of 2nd prototype.

DEPARTMENT OF INDUSTRIAL AND MATERIALS SCIENCE
CHALMERS UNIVERSITY OF TECHNOLOGY
Gothenburg, Sweden
www.chalmers.se

CHALMERS
UNIVERSITY OF TECHNOLOGY